1-1-2010

Compaction density variation in powder metallurgy components

Elham Jafar-Salehi
Ryerson University

COMPACTION DENSITY VARIATION IN POWDER METALLURGY COMPONENTS

By

Elham Jafar-Salehi

B.Eng, University of Tehran, Iran, 1999

A thesis

Presented to Ryerson University

In partial fulfillment of the

Requirements for the degree of

Master of Applied Science

In the Program of

Mechanical Engineering

Toronto, Ontario, Canada, 2010

© Elham Jafar-Salehi, 2010

Author's Declaration

I hereby declare that I am the sole author of this thesis or dissertation.

I authorize Ryerson University to lend this thesis or dissertation to other institutions or individuals for the purpose scholarly research.

Signatures

I further authorize Ryerson University to reproduce this thesis by photocopying or by other means, in total or in part, at the request of other institutions or individuals for the purpose of scholarly research.

Signature

Abstract

COMPACTION DENSITY VARIATION IN POWDER METALLURGY COMPACTION
Master of Applied Science 2010
Elham Jafar-Salehi
Mechanical Engineering
School of Graduate Studies, Ryerson University

The main objective of this research was to study the relationship between green density and compaction pressure in powdered metallurgy. Powder metallurgy has gained popularity and importance because of its near net shape, cost effectiveness and its ability to reduce the complexity of multileveled engineering components. However, powder metallurgy poses challenges that are yet to be fully understood. There are many works performed to address challenges such as the effect of friction, the tool kinematics, handling component prior to sintering and fracture under compaction.

This work concentrates on the relationship between green density distribution and compaction pressure. In order to measure the relative density of compacted components, Electron Scanning Microscope was utilized. One can intuitively conceive that the relative density increases as the compaction pressure increases, but the distribution of relative density requires more than intuition. It was determined that highest relative density occurs at the center of the specimen and reduces toward the die-powder or punch-powder boundary. For completeness, the application of artificial neural network (ANN) and finite element (FE) model in estimation of green relative density was studied. The results of this research signify that ANN is an excellent technique to determine the relative density distribution of un-sintered compacted specimen. Moreover, finite element method can accurately estimate the average relative density of compacted specimen.

Acknowledgement

I would like to give a special thank to Dr. Ghasempoor for his support and guidance. I am greatly indebted to Dr. Ghasempoor for allowing me to work on such wonderful, interesting and at time challenging project

Additionally, I would like to extend my gratitude to Dr. Lanny Pease (Powder-Tech Associated INC.), for his wisdom, knowledge and providing me with experimental sample and manufacturing information. Moreover, I like to thank Mr. Alan Machin and Mr. Qiang Li for their support, help and insight. Without their support, this study wouldn't have come to fruition.

Last but not least, I would like to thank my husband Mr. Hamed Tabatabaei for his moral support and patience. Finally, I like to dedicate my work to my beloved son, Kiarash who means the world to me.

Table of Content

List of Figure

List of Table

Chapter 1

Introduction

1.1 Motivation

Powder metallurgy (PM) is a popular processing technique to fabricate ceramic, metallic or composite components, typically of small size and of complex shape. In effect, PM is a near net shape process, which can produce components with high precision at low cost with little waste. There has been a significant expansion in the PM industry over the past decade [1]. PM components are replacing a wide range of casting, forging and machined components. Also, more and more complex multileveled engineering components are being manufactured using PM technology. This increasing complexity challenges quality control of the finished parts. Consequently, proper handling techniques throughout the entire PM process are required to manufacture consistent, uniform products. This must be based on a full understanding of each stage of the entire PM process.

Powder metallurgy has a unique set of benefits, most importantly being quite economical. Therefore, this method is very suitable for batch production of parts with complex shapes. Nowadays, powder metallurgy is considered a conventional manufacturing method even in high stress application [2]. Using powder metallurgy, it is possible to fabricate components, which otherwise would decompose or disintegrate. This is because powder processes are more flexible than casting, extrusion forming, or forging techniques. PM products are used in a variety of applications, such as automotive, aerospace and household appliances [3]. It is well known that

part manufacture using PM technology can lead to significant material and energy savings in some cases. Appreciation of the potential of PM technology for a given application often takes place after a part has been designed for manufacture by an alternative technology. In fact consideration of PM often does not occur until the part has been in conventional production for a considerable period of time [4]. Even in cases where a part is identified for manufacture using PM process, selection of material and process parameters require inputs from a number of experts in the field. Unlike wrought parts, design specifications determine the process parameters and type of powder material to be used in producing a PM part.

In powder metallurgy (PM), first the primary bulk material is physically turned to powder form and cleaned of oxides or other contaminants. Then the powder is injected into a mould or passed through a die to produce a weakly cohesive structure near the dimensions of the final object. This process is known as compaction and the product at this stage is referred to as green compact. Finally, the end part is formed by applying pressure, high temperature and long setting times, this process is known as sintering. The compaction process itself can be divided into five identifiable stages: filling, transfer (when required), compaction, unloading, and ejection. Modelling of powder compaction process has received considerable research attention particularly in compaction, unloading and ejection stages of the process [4]. With some justification, the powder metallurgy industry is constantly striving towards producing green parts with ever increasing densities. Higher density compacts, for the most parts, lead to improved post sinter properties in machining, dimensional tolerance and mechanical strength. Higher green densities are also traditionally associated with higher green strengths, a prerequisite to machining parts in the green state, since during this operation, parts are subjected to both clamping forces and the stresses associated with material removal. Except for the simplest part geometries,

determining an appropriate tool design and pressing schedule for the production of 'good' parts with an acceptable density distribution and without cracks is a costly and time consuming trial and error process. Inhomogeneities in the density of the final part can arise from many factors, particularly variations in the packing density of the powder particles after die filling. As mentioned previously, the green compaction process is one of the most important stages in PM, which is directly affected by the density and other properties of the green compact stage. Although, there has been many studies on density variation in compaction stage, most of these studies only considers average density distribution [3, 4].

1.2 Research Objective

The first objective of this research was to perform an experimental study of the density and void distribution in green compact powder metallurgy parts made of stainless steel 316L powder. To achieve this goal, no heat treatment and sintering and post-processing was performed on the as-compacted samples. The second objective was to study the application and predictive capability of Artificial Neural Network (ANN) techniques in determination of the green density. In recent years, ANN has been applied in many fields including function approximation and modelling. Artificial neural network is a kind of information processing technology, which is good for handling problems in which complex nonlinear relations exist among the input and output variables. The third objective in this work was to evaluate the results of finite element (FE) analysis in determination of green density. A comprehensive FE simulation was carried out to study the validity of FE results in green density determination. Finally, neural network and finite element results have been compared with the experimental results.

1.3 Organization by Chapter

The rest of this thesis is organized in the following manner: Chapter 2 presents a brief overview of powder metallurgy and application of artificial neural networks and finite element method in powder metallurgy and presents a literature survey of relevant research in this area. Chapter 3 explains the manufacturing setup and sample preparation steps. Chapter 4 presents the experimental results. Chapter 5 briefly explains the neural network modeling process and its application to the present work. The green density results predicted by neural network are then presented. Chapter 6 presents the FE model development and a brief overview of finite element method. The FE results and conclusions on the FE application and the validity of the FE results are also presented. Chapter 7 finally provides concluding remarks based on the current work.

Chapter 2

Literature Review

2.1 Introduction

Powder metallurgy has been used for manufacturing of a variety of products from brake pads to artificial joints. In the past few years, many experimental research works have been conducted to study the mechanical properties of PM components and the effect of processing steps in the final outcome. Moreover, analytical and numerical modeling have found growing popularity in analysis of green and sintered density of powdered metallurgy. This chapter presents an overview of the most relevant works in this area.

2.2 Experimental measurement of density distribution

Mamedov and Mamedov [5] presented a new fabrication method for the manufacturing of high density powder metallurgy parts using single pressing cold sintering technique. Using SEM images they estimated the compact green density of samples and explored the influence of the processing conditions on the density. They found that in order to reduce the negative influence of gases trapped in the pores, it is necessary to ensure effective air venting from the compaction zone. They introduced small holes on the die body to provide a proper vent for trapped air. In this case, they avoided sintering and achieved cold sintering under high compaction pressure.

In another study, Korachkin *et al.* [6] measured young's modulus and tensile strength properties of green compact alumina, Zirconia and Distaloy AE powders. They conducted a

series of experiments, using an instrumented die, unconfined compression cylinder, three-point bending and Brazilian disc test to explore the elastic modulus and tensile strength in powder compacts. They found that the measured modulus data does not depend on data reduction method. It was speculated that the die dilation at high pressures has an effect, since the Young's modulus slightly decreases at higher density levels. Modulus data from the unconfined compression of a cylindrical compact lead to a lower value of modulus in comparison with the instrumented die test. They attributed this to the removal of confining and frictional effects at the die wall. Modulus data obtained from three point bending were again lower than that obtained from the unconfined compression test. They also found that, lubricant for Distaloy AE has a small effect on Young's modulus. The modulus of the Distaloy AE powder increases as the density increases and it was attributed to the bonding between particles under this condition

Briscoe and Rough [7] explored some of the effects of the alumina powder-die-wall friction, the compact aspect ratio and the ultimate applied compaction stress on the relative density of samples. The resulting density distributions within the samples were measured using powders with various colors. They generated contours of constant density at various heights of the samples. Their results show that wall lubrication has an effect on density distribution. They found that the local density varies across the sample. The average density of wall-lubricated samples was found to be higher than that of the non-lubricated-wall samples. The density distribution and wall stresses were also determined analytically using the Janssen-Walker method [8].

Khorsand *et al*. [9] experimentally studied the effect of heat treatment duration and temperature on the mechanical properties of the compacted steel powders with various densities. Subsequently, the results of their experimental investigation were used for neural network

simulation. Sudhakar and Haque [10] performed an experimental study and obtained the mechanical properties of powder metallurgy high density steel samples. They found that the tensile properties of samples were sensitive to heat treatment. They identified a composition (0.47% C and quenched at 503 K) for which the produced samples exhibited the best fatigue and tensile properties. For each samples, they experimentally determined the mechanical properties such as, the endurance limit, yield strength, and hardness of the samples. They also incorporated their results into neural network simulation.

Korachkin *et al* [11] developed a floating die shear plate apparatus and used it to explore lubrication mechanisms and to assess the effectiveness of lubrication under a wide range of both compaction and normal loading conditions. The equipment was used for exploration of the effect of density and normal stress on the friction between compact and tool set surface. Tests were carried out using Distaloy AE, a Zirconia target surface and Kenolube as lubricant. They found a friction correlation that includes both density and normal stress effects. Their results suggested that the coefficient of friction during ejection was lower than that during compaction. They speculated that the lubrication regime may break down leading to galling at very high contact stresses. Taking into account the friction mechanism, surface analysis using EDX (Energy Dispersive X-ray) did not detect the presence of lubricant on the compacted surface. However, it did reveal two distinct pore types, a 'dark' one having a higher than average level of carbon and a 'light' one having a higher than average level of nickel. Both analyses suggested significant closure of open pores due to sliding with topographical analysis revealing trace of pores under the deformed particles that make up the exterior of the compact surface. Their results confirmed that there was no noticeable benefit in increasing admixed lubricant content above 0.5%. Die wall lubricant was also found to be effective, achieving a reduction in friction of up to 58% for

un-lubricated powder and up to 27% for powder containing 0.5% admixed lubricant. This was achieved for a lubricant film with typical thickness of 5–20 μm.

Modnet [12], Sinka *et al.* [13] and Michrafy *et al.* [14] showed that there was a great need for both accurate friction data for specific powders and a better overall understanding of the friction mechanisms that are present during the powder pressing cycle. Studies of friction comprise development of measurement techniques, exploring the effect of different powder types and the presence of lubricant. They concluded that the friction is the key to the density homogeneity of the compressed part.

Doremus *et al.* [15] used a shear plate apparatus to investigate the friction between iron powder and a tungsten carbide target surface. Density, normal stress, sliding velocity, temperature and displacement were considered as parameters in the friction process and their effects were evaluated. The authors concluded that density and normal stress reduced the friction, sliding velocity increased the friction, and temperature had no significant effect on it. The amplitude of the displacement was also found to have a significant impact on friction, leading to damage of green parts.

Sanchez *et al* [16] studied the hot isostatic pressing as a manufacturing process capable of producing mechanical parts in one step by the hot forming of metal powders. A trial and error method was used for this manufacturing technique; several prototypes were therefore manufactured before a successful conclusion was reached. They found that the pressure was partially transmitted to the powder because of the container rigidity. In their work, new rheological functions were determined with the stress values obtained by numerical simulation. Their new numerical simulations resulted in better agreement with the experimental findings.

Degnan *et al.* [17] investigated the machinability and mechanical strength of green compacts containing two lubricants. They considered drilling operation and Brazilian compression test for their study. They found that machinability does not improve significantly at high compaction pressure. It is well understood that presence of lubricant of the system affects the green strength for a given density. Studies have been carried out to compare the green strength and type of lubricant used in compaction process. These studies are appropriate for characterization of machining of green compacts using various lubricants [18].

To this day, obtaining high density part using cold compaction remains a challenging task. It certainly presents an economically viable option in comparison to warm compaction [19]. Friction between die and powder is the main limiting factor for this process. Many studies have focused on friction phenomenon to increase the density. It has been demonstrated that increasing the internal powder lubricant decreases the density. In some applications, decreasing the density during sintering may have a harmful effect on the porosity of the part [20]. Bonnefor *et al*. [21] suggested a new coating on the compaction tooling system to overcome the effect of internal powder lubrication phenomenon.

Every researcher in the field of powder metallurgy faces the same issue, the inhomogeneous density distribution. There are other issues such as tool wear, loss of press power, etc. but the density distribution is the most important challenges [22]. Solimanjad [23] used a new device to measure the radial pressure on die body and strain gauge to measure pressure of punch bodies. The new device offers the possibility of investigating the pressure on powder particles and keeping the green density constant. The investigation showed that coefficient of friction can be reduced by using proper lubricant and particle characteristics.

2.3 Artificial neural network and density distribution

There has been a great amount of experimental research data collected on powder metallurgy in past few years, but they have not been matched by computer modeling [24]. There have been some attempts to develop a comprehensive data base for manufacturing, tooling and powder selection. However, this information is limited and more research is required for a meaningful model useful to manufacturers [25- 27].

Ozan *et al*. [28] studied the application of ANN in prediction of pore concentration of aluminum powder metallurgy component. They used key parameters such as mean particle size, pressure and alloying element concentration to train neural network for predicting pore concentration of sintered parts. It was reported that the parameters used were effective on pore concentration profile but had little effect on pore diameter. According to authors, ANN was successful in predicting the pore concentration as function of key parameters. Altinkok and koker [29] studied the application of ANN in predicting mechanical and density properties of particle reinforced composite at room temperature. They experimentally determined the effect of various SiC size particles on mechanical response and used this information in ANN training phase of their study. They found the neural network extremely successful in determining experimental results

Wikman *et al.* [30] developed an efficient way to determine the necessary constitutive model parameters of the numerical models by means of inverse modelling. The objective function was formed and optimized based on the force–displacement experimental data and the numerical model prediction. Minimization of the objective function with respect to the material parameters was performed using in-house optimization software. They concluded that their

proposed approach could readily be used to determine material parameters and estimate the density distribution accurately given fabrication parameters.

In another study, Cherian, Smith and Midha [31] used the neural network approach to model powder compaction. In this statistical method, which is similar to non-linear regression analysis, experimental data are used to train a network to be used for design purposes later. In their study, input data to the network were parameters, such as compact pressure, particle size, etc. A neural network was obtained in order to recommend suitable metal powder compositions and process settings. Their results confirmed the capability of neural network for design purposes. In particular, they trained the network such that it can predict the sintered density of manufactured parts when processing data were given to the network.

In another neural network study by Khorsand et al. [9], the effect of heat treatment duration and temperature on the mechanical properties of the compacted steel powders with various densities was studied. Experimental data were used to train a neural network for predictions of hardness when the heat treatment conditions were presented to the model. The predictions obtained from the neural network model in their work showed a good agreement with the experimental results.

Sudhakar and Haque [10] performed an experimental study on heat treatment sensitivity of compacted components. They experimentally identified the composition that produced the best fatigue and tensile properties. The experimental measurements were used to train a neural network to predict the mechanical properties such as, the endurance limit, yield strength, and hardness of the samples. Their ANN simulation showed a very good agreement with experimental data.

Kafkas *et al.* [32] studied the application of ANN in determining the effect of heat and residual stress. They studied the residual stresses in powder metallurgy steel samples using the electrochemical technique. The values and distributions of residual stresses occurring in the samples were determined under various densities and heat treatment conditions. The heat treatment and the residual stress data were used to train a neural network, where the residual stresses was considered as the output. Their study revealed that neural network, when trained based on the appropriate input parameters, can accurately predict the residual stress in compacted materials.

Smitha, *et al*. [33] utilized neural networks for solving the 'inverse problem', for assisting with materials selection. The term inverse problem refers to the task of employing process output information (i.e. the required mechanical or physical properties of the final material), in order to recommend suitable input settings for the process concerned. For example, for the powder metallurgy (PM) process, where parts are manufactured from powdered metals, powder composition, compaction pressure, and sintering conditions are important input parameters that have to be controlled.

Previous attempts at solution of the inverse problem have involved the use of statistical methods for fitting curves to the available experimental data. While such techniques are useful for identifying general trends in process inputs and outputs, they are subject to a number of disadvantages. PM manufacture involves multiple process inputs that are non-linear and the experimental data exhibits considerable noise. When fitting curves to non-linear data, the selection of transform is inevitably subjective and becomes very difficult when multiple inputs are involved.

Additionally, regression analysis is not well suited to modelling noisy data. These considerations have lead to the identification of the neural network approach as being suitable for PM modelling for materials selection purposes. In such cases, multiple inputs, modelling of highly non-linear responses and the avoidance of detrimental noise effects have been provided by training a back-propagation neural network with experimental data for ferrous PM data. The neural network results for process inputs were compared to those generated by regression analysis. The neural network reduced the standard deviation of the errors associated with the inverse solutions by 36% [33].

2.4 Application of finite element method in powder metallurgy

The main merit of powder metallurgy is its near net shape forming of mechanical parts. Finite element has been used to predict the density distribution of sintered and un-sintered powder components with relatively good accuracy. Generally, the accuracy of FE results lies in accurate modeling of part geometry, powder nonlinear mechanical properties and die-powder frictional properties. Furthermore, finite element simulation can be used to perform realistic computer experiments minimizing costs, time and resources needed for process and equipment optimization.

Han *et al*. [34] and Cunningham *et al* [35] used FE method to simulate the compaction of pharmaceutical products. In both studies, a modified Drucker-Prager model was used and a nonlinear elasticity constitutive law was proposed to capture the nonlinear unloading behaviour. They implemented their model using ABAQUS software utilizing a user subroutine and managed to accurately reproduce the experimental observations. They used the FE and their

proposed nonlinear model to predict the stress and density distribution during compaction, depression and rejection period.

Prealloyed powders undergo significant dimensional change during sintering and springback process. This characteristic of PM poses a challenge to the wide use of powder metallurgy. Finite element analysis has been employed to address this issue and to help manufacturer in design and selection of tooling. Ma *et al.* [36] used finite element method to predict the relative density and stress distribution in both compacted materials and tooling. Forming multi-level components in die generally result in an inhomogeneous density distribution. The density distribution has been the subject of research and simulations for design and manufacturing purposes [37, 38, 39]. Huang et al. [40] used stress flow model in finite element to simulate the compaction process of cylindrical component. They used three dimensional models to simulate the compaction of gear-hub assembly with various initial densities. They compared their results with experimental data and concluded that flow model predicts the density distribution accurately. Their results also suggested that the simulated density distribution was homogeneous after optimization.

Several yielding criteria have been proposed and implemented using finite element method. Most of these yielding functions were developed for materials with relatively high starting relative density. Recently, Fleck et al. [41] proposed a yielding function for material with very low starting relative density. Kwon et al. [42] used finite element method to simulate densification of cold compaction of stainless steel powder using Fleck yielding criterion. In their study, they considered friction and various compaction pressures using an elastoplastic material model (Fleck) [41] and (Shima and Oyane) [43] yielding function criterion. In their study, they

considered both single and double action compaction process. Their simulation produced accurate results of densification for low tapped density materials.

Briscoe and Rough [7] studied wall friction model to develop a more accurate FE model. In their FE simulation, they adopted state parameters for a numerical finite element model of powder compaction that incorporated a non-linear elastic constitutive material model. The numerical results showed agreement with the experimentally determined distributions and those obtained from the application of the Janssen-Walker model [8].

Coube and Riedel [44] numerically studied the powder die compaction with emphasis on cracking of samples and green density distribution. The reasoning behind modeling and testing non-sintered parts was to optimize the tools and the press kinematics using computers models. They concluded that computer modeling prior to the manufacturing improves the success rate of designing the tools and manufacturing processes. Using a finite-element approach, they modified the Drucker–Prager cap model [45, 46]. The model was used to describe the formation of cracks during various stages of sample and part production and handling. Their model needed several parameters, which were determined from the measured green strength values of iron powders. They found a good match between the results and the measured density distribution. They also explored the risk of cracking in various conditions.

Park *et al* [47] simulated three types of duplex compaction, employing finite element method using a backward Euler method and a yield criterion, which can describe the densification behaviour of ceramic powder. They examined the effects of two parameters in the yield criterion on the uniaxial compaction curve. The calculated shape of duplex compacts and density distribution showed good agreement with experimental results using Zirconia powder. It

was found that a height difference between inner and outer compacts after combination disappears by friction force reduction.

Zhang *et al.* [48] simulated the densification and creep behaviour of stainless steel powders. The appropriate material model was implemented in ABAQUS through a user subroutine code. Their approach was based upon the continuum theories of elastic and nonlinear-viscous deformation of porous bodies. The nonuniform density distribution of the green compact was considered as an initial condition for the FE model. Grain growth, gravity, thermal expansion, thermal conductivity, and other factors were also considered in the simulation. Several experiments were performed and the simulation results of axial shrinkage and density distribution changes were compared before and after sintering. Their FE results showed good agreement with experimental findings.

2.5 Summary

Many experimental works have been published that address the relationship between compaction pressure, types and amount of lubrication, mechanical properties and the density distribution. However, most experimental works have been conducted on either cold or hot sintered components. From this survey, it can be determined that there is a need for experimental evaluation of green density distribution as the function of compaction pressure prior to sintering.

Therefore based on the above mentioned literature review, the aim of the present work was to conduct a series of experiments and compare the predictive capability of two models in determining the green density variation in PM of stainless steel, namely neural network and finite element. This study consists of three parts: First, the measurements of green density variation on sample surfaces utilizing Scanning Electron Microscopy (SEM) images were made.

Next the neural network model was constructed and the predictive capability of it was examined. Finally, finite element method was used to simulate the fabrication and its results were compared to experimental to examine its applicability.

Chapter 3

Experimental Procedures

3.1 Introduction

This chapter introduces the procedures for fabrication of specimens and other experimental setups. The experimental method of measuring green relative density using Scanning Electron Microscopy is detailed and the experimental data are presented.

3. 2 Specimen Size and specification

For the purpose of this study, three sample sizes were considered; 1) 31.75 mm by 12.275 mm by 10mm, 2) 31.75 mm by 12.275 by 15 mm and 3) 31.75 mm by 12.275 by 20 mm. For each size, five specimens were fabricated at different compaction pressures. Therefore, all together, fifteen samples were fabricated. The samples were prepared by Powder-Tech Associated INC., US.

Since the determination of green relative density in all samples was the primary objective, the surface and through thickness measurement were taken for accurate quantification of average density. To do this, after surface density measurements, the surface was ground to a specific thickness and measurements were taken. The grinding process was continued and overall four surface measurements for each sample were taken, see Figure 3-1. Table3-1 shows the sample size and the amount of material ground for each subsequent measurement. Throughout this work, the layer designation outlined in table 3-1 is used.
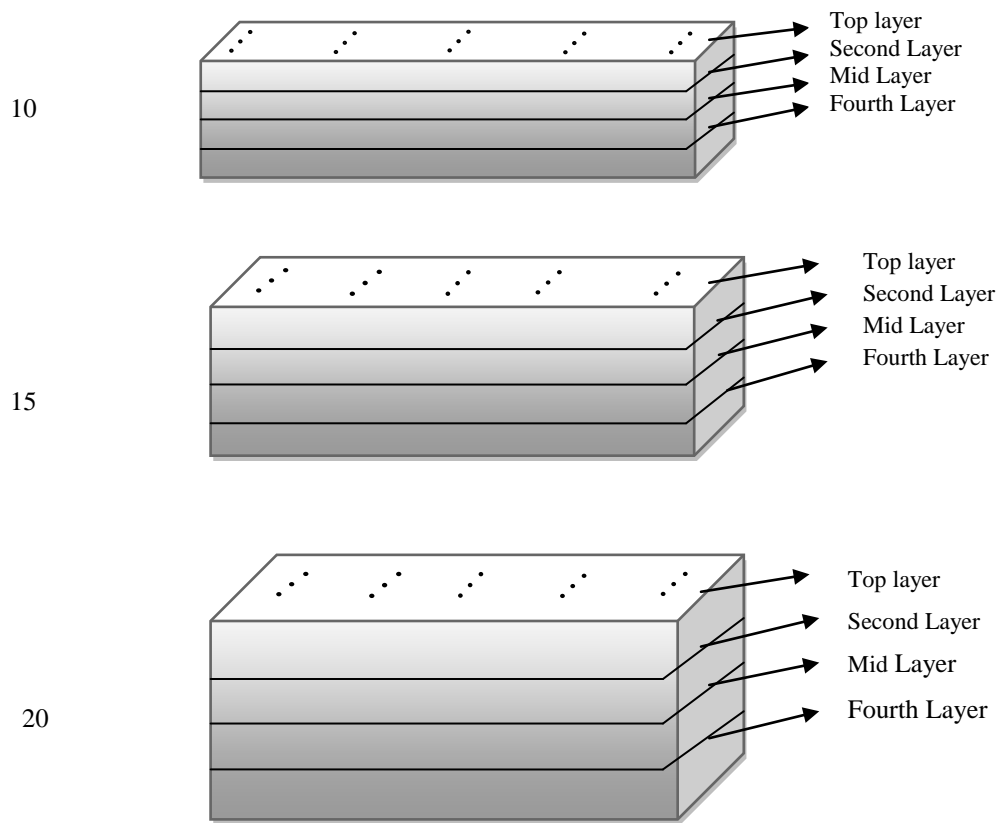
Figure 3 - 1: Pictorial representation of the location of relative density measurement. Average of three measurements on the lateral axis of specimen was taken. Five readings were taken along the longitudinal axis of each specimen

Table 3 - 1: Surface measurement specification

Sample thickness	10 mm	15 mm	20 mm
Top layer	0 mm removal	0 mm removal	0 mm removal
Second layer	2.5 mm removal	5 mm removal	5 mm removal
Mid-sample	5 mm removal	7.5 mm removal	10 mm removal
Fourth layer	7.5 mm removal	10 mm removal	15 mm removal

3.3 Powder Materials

The powder selected for this study was water atomised stainless steel ($316L$) with a tap density of 3.48 g/cm^3. This powder is a fully alloyed mesh size of 100 (or less than 150 micrometer grain size) austenitic steel powder, generally conforming to the chemistry of AISI

316L (low carbon). The powder is produced by water atomization and has an irregular particle shape ideally suited for compacting. The median particle size of the powder is about 25 µm. This grade of stainless steel offers a good combination of corrosion resistance, machinability and mechanical properties. It also offers superior strength at elevated temperatures and is non-magnetic. Table 3-2 shows the composition of the powder. Table 3-3 summarizes the physical characteristics of the powder.

Table 3 - 2: Composition of the powder: SS 316L

CHEMISTRY,	Wt% (Typical)
Chromium	17
Nickel	13.5
Molybdenum	2.2
Silicon	0.75
Manganese	0.12
Carbon	0.02
Phosphorus	0.02
Sulfur	0.01
Iron	Balance

Table 3 - 3: Physical Specification of the powder

SCREEN ANALYSIS	(Typical)
+100 mesh (>149µm)	1%
-100 +500 mesh (105 to 149µm)	10%
-150 +200 mesh (74 to 105 µm)	18%
-200 +325 mesh (44 to 74 µm)	29%
-325 mesh (<44 µm)	42%
Apparent Density g/Cm^3	2.80
Flow Rate sec/50gr	26.6

3.4 Sample preparation

Tinius Olsen testing equipment was used to fabricate the specimens. This machine is a standard tensile testing machine that has been retrofitted to be used as a metal powder compaction apparatus. It consists of four columns with dual hydraulic pressure loading. Each pair of columns are connected to the cross head of the machine giving it capability to move the top and bottom cross heads simultaneously or independently. The die is mounted in a small spring loaded holder. Using the swabbed die, the powder is poured into the die and levelled. During compaction, the die floats down on the springs. This results in equal compaction on both ends of the part. The top punch is then removed by hand, and the die is pushed down onto the lower punch, forcing the rectangular test bar up and out of the die [49].

3.5 Specimen Specifications and Fabrication

The compressibility data shown in Table 3-4 were used to estimate the green density for each selected pressure. Five compaction pressures were selected to represent the range of pressures available on the compaction press which had a maximum compression force of 60,000 lb. The lowest density was selected such that the resulting sample would hold together after pressing. The die had a cross section of 1.250" x .500" and is the standard used for a transverse rupture bar as outlined in ASTM B 925. There is no admixed lubricant in the powder; therefore, DuPont Vydax AR, a fluorotelemer, diluted 10 to 1 in DuPont Vertrel FX was used as a die wall lubricant. The die was swabbed between each compaction. Five pressures were used in compacting of the samples. These were: 276, 372, 469, 565 and 662 MPa. Knowing the sample volumes, the mass required for each part was calculated (see Table 3-4).

Table 3 - 4: Sample specifications and identification

Pressure MPa	Sample #	Mass (g)	Length (mm)	Width (mm)	Thickness (mm)	Density (g/cm^3)
276	1-1	23.49	31.75	12.725	10.0	5.58
	1-2	35.49	31.75	12.725	15.0	5.57
	1-3	47.33	31.75	12.725	20.0	5.56
372	2-1	25.09	31.75	12.725	10.0	5.93
	2-2	37.22	31.75	12.725	15.0	5.90
	2-3	50.00	31.75	12.725	20.0	5.90
469	3-1	26.24	31.75	12.725	10.0	6.12
	3-2	38.19	31.75	12.725	15.0	6.09
	3-3	51.39	31.75	12.725	20.0	6.1
565	4-1	26.32	31.75	12.725	10.0	6.35
	4-2	40.19	31.75	12.725	15.0	6.35
	4-3	53.16	31.75	12.725	20.0	6.36
662	5-1	27.35	31.75	12.725	10.0	6.54
	5-2	40.64	31.75	12.725	15.0	6.55
	5-3	54.07	31.75	12.725	20.0	6.57

3.6 Sample Post-Processing and Preparation for SEM

The die lubricants tend to contaminate the specimen surfaces. This was observed in all samples fabricated for this work. Thus, for achieving a clean surface, all samples were cleaned by acetone, in order to remove the punch surface lubricant that was applied on the punch surfaces to facilitate the easy ejection of samples.

In order to avoid erroneous results due to surface lubricant, all samples were polished using abrasive paper No.4. The polishing was performed using a belt sander adjusted to a low speed. In addition to the sample's original surface, surface morphologies and densities were also examined in three additional sub-layers. In order to remove the desired amount of material, each sample was polished using the same belt sander.

While polishing the samples, it was observed that large chunks of the material were being removed. As a result, it was difficult to obtain a smooth surfaces needed for density analysis. This was due to the inadequate strength of the specimen as the samples were not sintered.

Figure 3 - 2: A photograph of the JSM-6380LV SEM machine used in this study [50]

The surfaces of polished samples, obtained after compression, were examined using a JSM-6380LV SEM shown in Figure 3-2 [50]. The SEM micrograph of the top layer of 10 mm thick specimen compacted at 276 MPa is shown in Fig.3-3. The Figure shows widespread deformation of the powder particles together with evidence of extensive powder particle interlocking and void areas. The sample surface morphology and microstructure was evaluated by image analysis of individual SEM images. For each layer of sample, fifteen SEM images were digitized and processed to identify void and filled parts of the surface. The density at a specific layer (the density on specific layer at specific pressure) of the sample was calculated by averaging over the 15 readings on that specific layer. For the calculation of local density, the

density of bulk stainless steel 316 L, which is 7.99g /cm^3, was multiplied by the fraction of area.

Also, for some cases, energy dispersive spectroscopy (EDS) tests were performed on the samples

to identify the composition of dark and bright spots. EDS results showed that the dark areas are

mainly void, whereas the bright areas are compacted particles. Figure 3-3 shows a typical EDS

analysis.

(a)

(b)

(C)
The white spots are almost 100% composed of the
S.S. ingredients

(d)
No ingredient of S.S. was found in dark areas
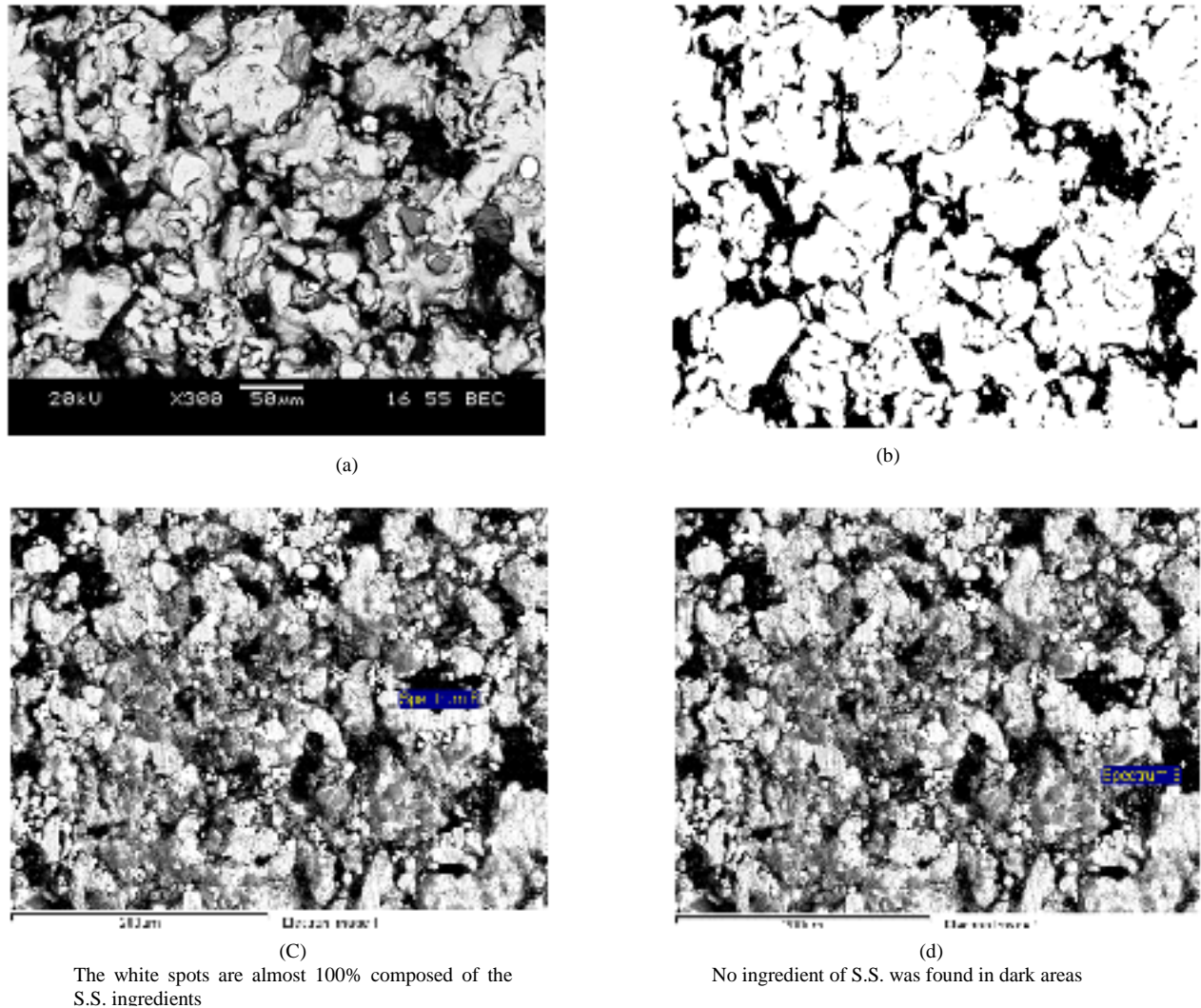
Figure 3 - 3: Scanning electron microscope (SEM) images of stainless steel powder-compacted samples. (a) a typical
SEM image; (b) post-processed image of part; (c) and (d) Energy Dispersive X-Ray Spectroscopy (EDS) analysis
and the SEM of two representative white and dark points, respectively.

Looking at Figure 3-3, one can see the distinction between dark and white areas. The dark areas are dense areas and pale while areas are the void areas. The post processing of SEM was performed by Open access image analyzer, ImageJ software. The imageJ software work based on assigning a number from 0 to 255 pixels from white to black. However, the contrast in colour in every image is relative, meaning a 0 may not necessarily be applied to white or 255 to a black area. Thus, a threshold was defined to identify the boundary of void and compacted area. In this work, numbers from 0 to 55 were assumed void areas and the remaining were considered dense and compacted areas. To check the validity of this assumption, we compared the overall density with the estimated density of the sample. Finally, using this threshold, the void and compacted areas were determined and used to obtain the local green density.
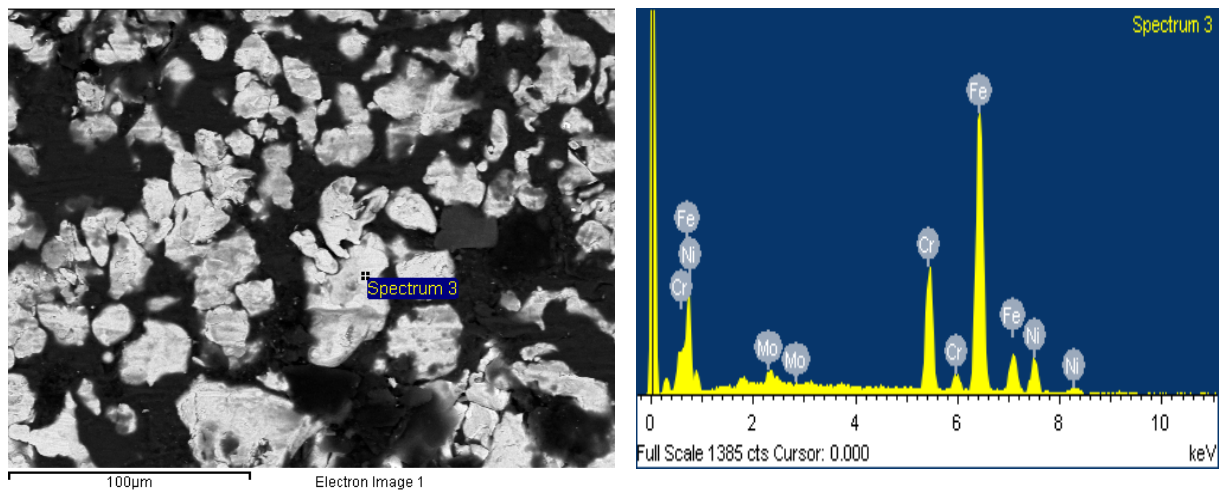
Figure 3 - 4: typical EDS white area element analysis.
(Cr: 18.35 Wt%, Fe: 66.41 Wt%, Ni: 12.6Wt%, Mo: 2.64Wt %)

25

Chapter 4

Experimental Results

4.1 Introduction

This chapter presents the experimental measurements and explores the results. First, the relative green density measurements are presented. Next the effect of the sample height increase on relative green density at constant pressure is studied. Furthermore, the effect of an increase in compaction pressure on relative green density is examined and the results are presented. Finally, an overall summary of the experimental data is given.

4.2 Distribution of Relative Green Density at Constant Pressure

In order to estimate the local relative green density, Scanning Electron Microscopy (SEM) was utilized. Three SEM images were taken close to the die wall (on the sample edges) on both sides of the sample; three images at the samples centers, and three images between the two above mentioned spots, i.e. at equal distances away from the die wall and the sample center, at both sides of the center. These measurements were taken in four layers: the top surface (surface that is in contact with the punch), equal distance from either side of both top and bottom surfaces, and the mid-sample surface. Using the method outlined above, the local green densities at selected points of each sample were measured and reprehensive plots were produced. Figures 4-1 to 4-4

display the variation of the local green density of the sample with 20 mm thickness made at die pressure of 469 MPa.

These images show the relative green density (correlated with the void density) at various locations and depths on the 20 mm sample. As mentioned previously, these samples were made using double surface compacting technique. Therefore, friction between punch and powder exists on both sides of the sample during the compaction process. Because of this, it was expected that the density at the mid-surface of the sample would be the highest and it would decreases toward either side of the mid-surface. Additionally, there is friction between die and powder, which would make the relative green density higher at the center location of any given surface than the location close to the die body.
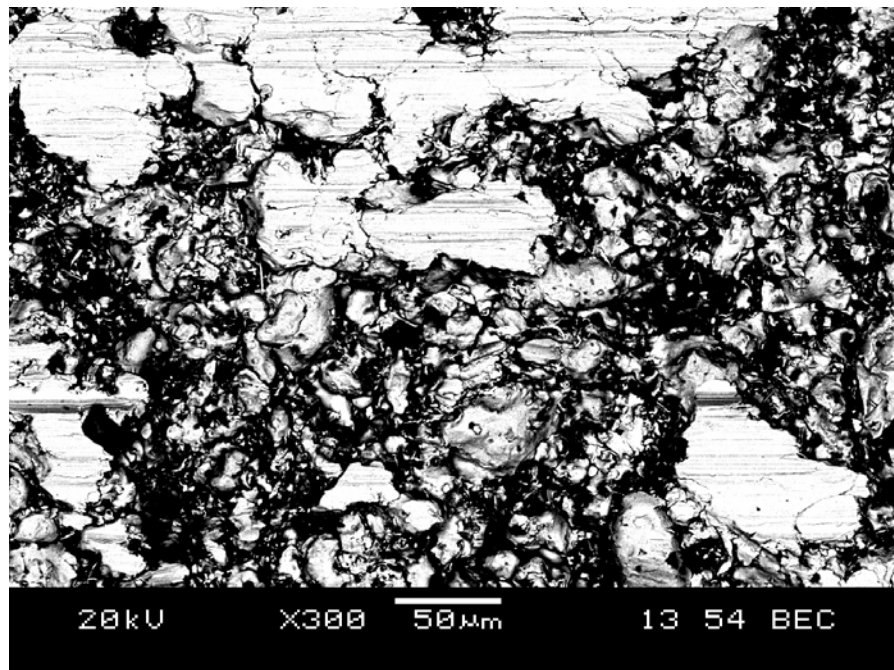
Figure 4 - 1: Scanning electron microscope (SEM) images of stainless steel powder-compacted samples No. 3-3 (center) for top surface
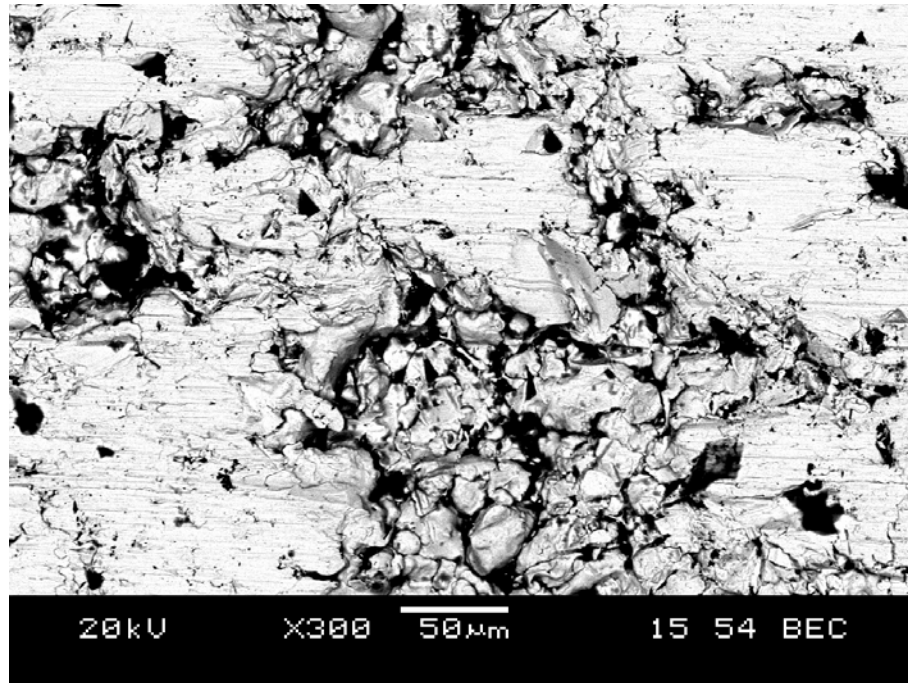
Figure 4 - 2: Scanning electron microscope (SEM) images of stainless steel powder-compacted samples No. 3-3 (center) for second sub-layer surface.
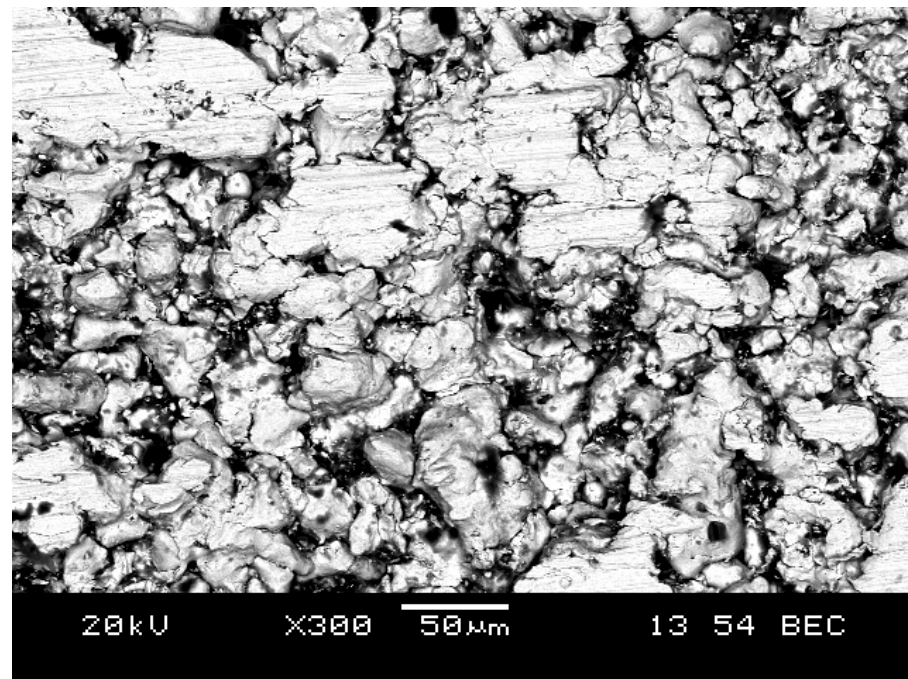
Figure 4 - 3: Scanning electron microscope (SEM) images of stainless steel powder-compacted samples No. 3-3 (center) for third sub-layer surface
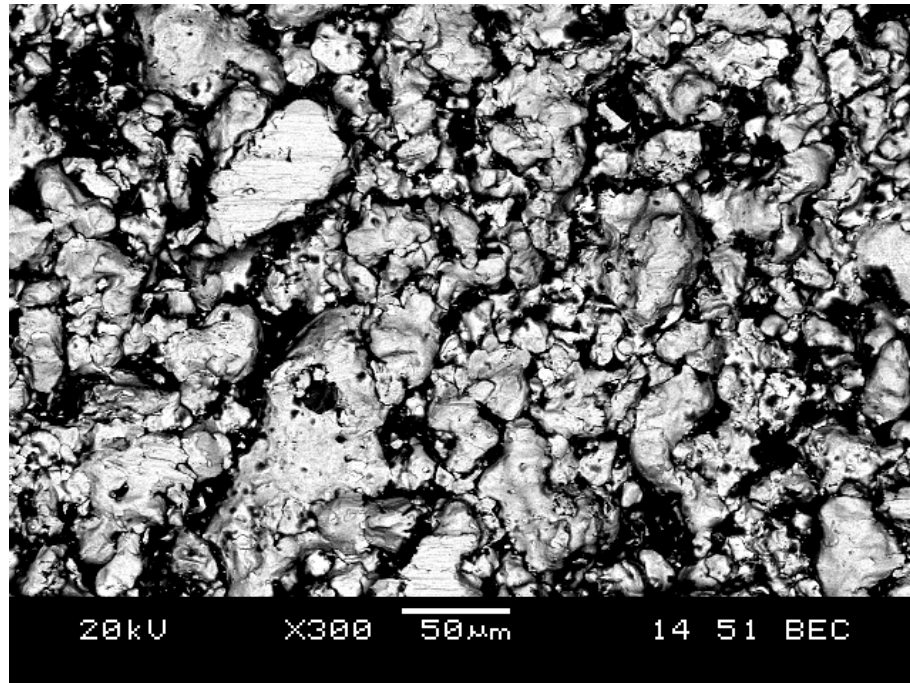
Figure 4 - 4: Scanning electron microscope (SEM) images of stainless steel powder-compacted samples No. 3-3 (center) for forth sub-layer surface

To verify this expectation, the densities of the specimen were measured at mid-surface, two equal distances from mid-surface and top surface. The experimental measurement were determined to be 5.8 g/cm^3 on the top, 5.91 g/cm^3 on the layer above mid-surface, 6.2 g/cm^3 on mid surface and 5.87 g/cm^3 on layer below the mid-surface. This was the trend in all samples fabricated at various pressures. Another important observation was that the images taken closer to the die body showed less relative density than the center point of the specimen.

Figures 4-5 to 4-10 display the variation of the local green density along sample's longitudinal axis for compaction pressure of 372 and 565 MPa for 10, 15 and 20 mm sample sizes. Figures 4-5 to 4-7 show the variation in local green density along the sample longitudinal axis at second layer, mid-sample and fourth layer, respectively, for the specimen fabricated at compaction pressure of 372 MPa. Also, Figures 4-8 to 4-10 shows the similar layer results for

the specimen fabricated at 565 MPa compaction pressure. These Figures show the distribution of the relative green density throughout a sample at given compaction pressure. 0 (x axis origin) denotes center of the samples. Average of densities of three data points selected on the sample longitudinal axis (two points on the top and bottom and one on the center) along the line perpendicular to the sample longitudinal axis.

Overall it is observed that the local relative green densities are symmetrical about the sample center. In general, one may expect that the density should be higher in the center as compared to the edges. This is in fact observed in all Figures. Particles adjacent to the sample edges have frictional interaction among themselves as well as those with the walls, whereas far from the edges and particularly in the center, the wall friction is absent and particle interlocking may readily occur. These results in higher local densities in the sample center compared to the edges.
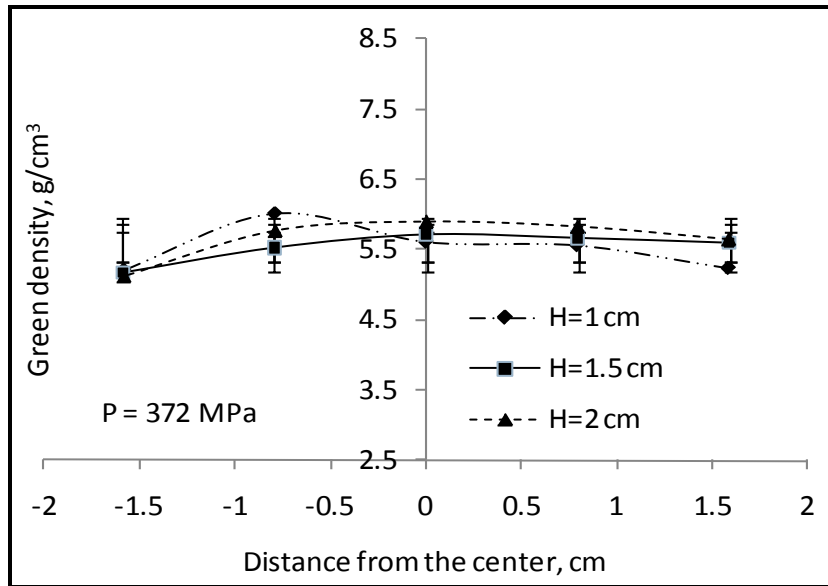
Figure 4 - 5: Variation of local green density along sample's longitudinal axis at given pressure (372 MPa) for three sample heights (second surface).
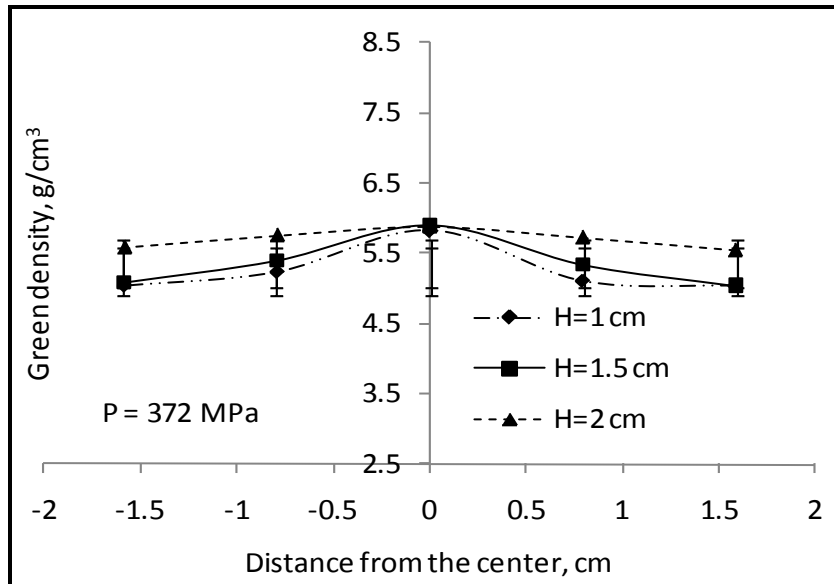
Figure 4 - 6: Variation of local green density along sample's longitudinal axis at given pressure (372 MPa) for three sample heights (middle surface).
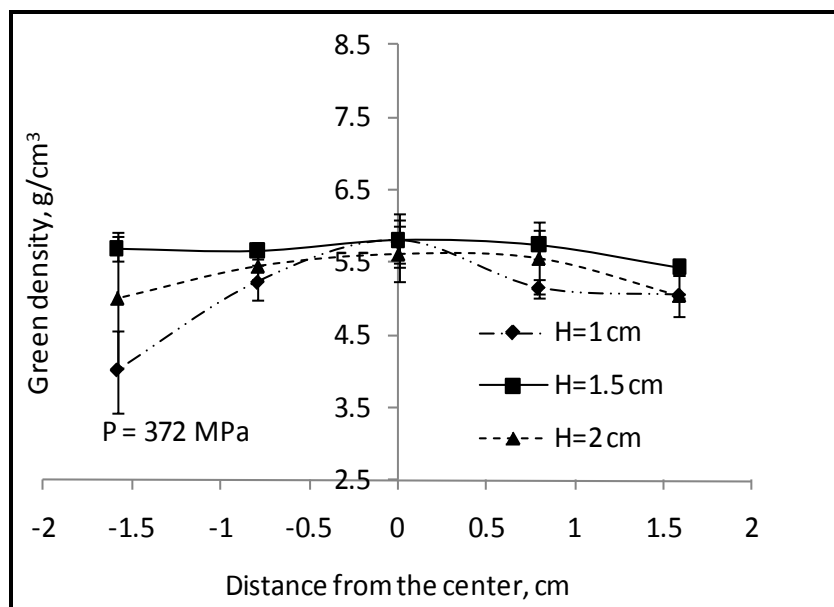
Figure 4 - 7: Variation of local green density along sample's longitudinal axis at given pressure (372 MPa) for three sample heights (forth surface).
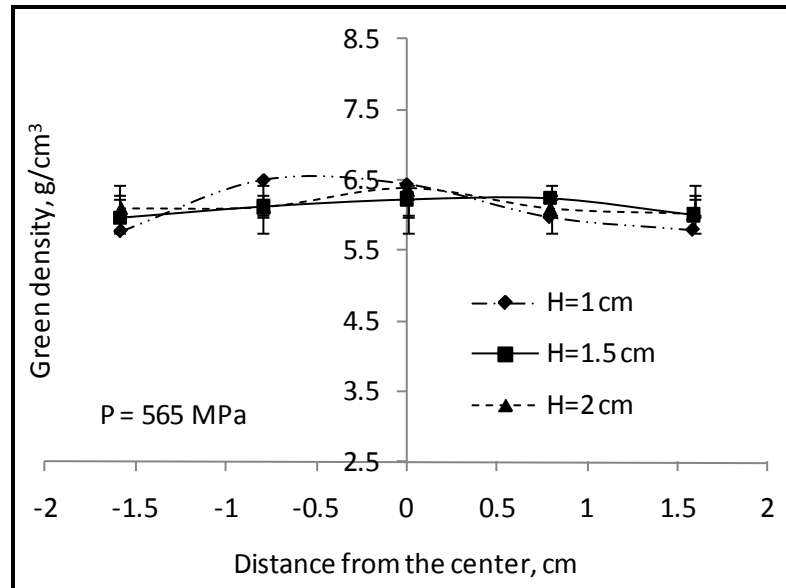
Figure 4 - 8: Variation of local green density along sample's longitudinal axis at given pressure (565 MPa) for three sample heights (second surface).
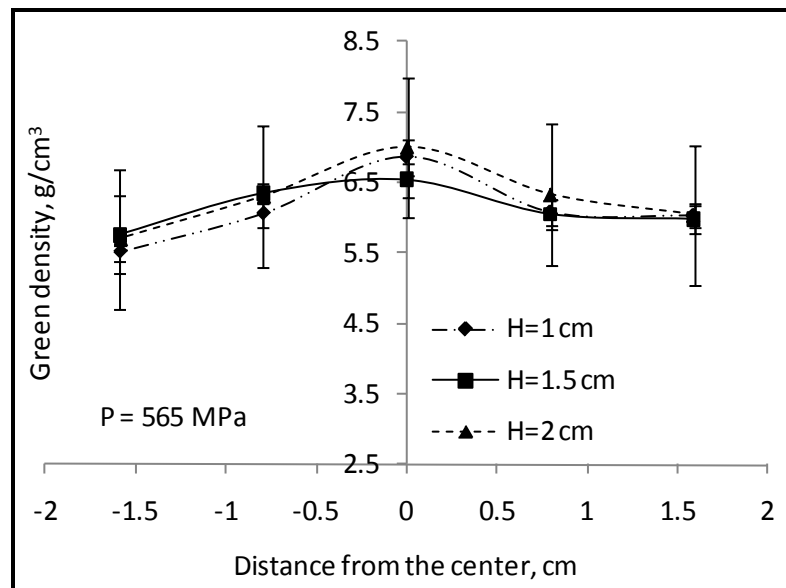
Figure 4 - 9: Variation of local green density along sample's longitudinal axis at given pressure (565 MPa) for three sample heights (middle surface).
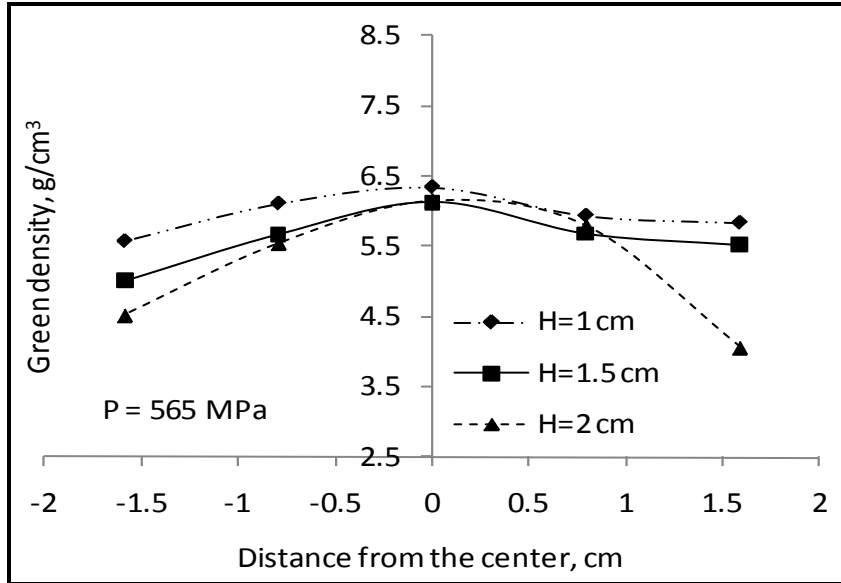
Figure 4 - 10: Variation of local green density along sample's longitudinal axis at given pressure (565 MPa) for three sample heights (forth surface).

4.3 Effect of Sample Size Change on Relative Green Density under Constant Pressure

In this work, specimens with three specific thicknesses were fabricated. From the earlier results, it was determined that the friction between the die body and the punch has significant effect on the relative green density distribution. In this work, samples with 10, 15 and 20 mm thicknesses were fabricated under five specified pressures. The important question was whether the 10 mm sample would have different relative density distribution than the 15 or 20 mm thick samples fabricated under the same compaction pressure, for instance 372 MPa. Therefore, the relationships between pressure, sample thickness and density were examined. The SEM results showed that the green density is dependent on compaction pressure but independent of original thickness of the samples. For instance, at compaction pressure of 565 MPa, the measured green density on the top surface of 10, 15 and 20 mm thick samples did not demonstrate conclusive evidence of thickness dependency. This observation was consistent at various layers and various

33

compaction pressures. Figures 4-11 to 4-13 depict the top surface density distribution of 10, 15 and 20 mm thick sample fabricated at 662 MPa.
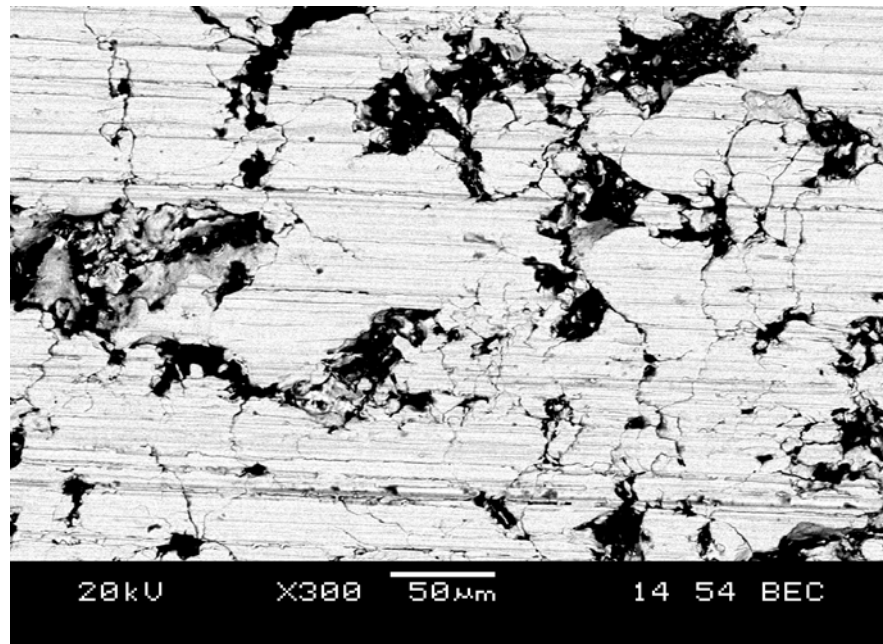
Figure 4 - 11: Scanning electron microscope (SEM) images of stainless steel powder-compacted samples No. 5-1 (center) for first layer (top surface).
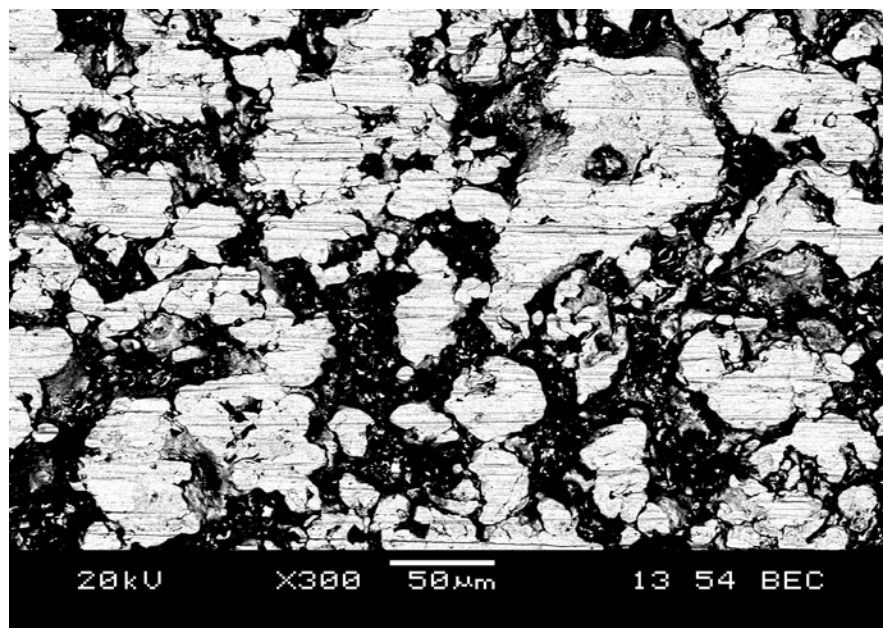
Figure 4 - 12: Scanning electron microscope (SEM) images of stainless steel powder-compacted samples No. 5-2 (center) for first layer (top surface).
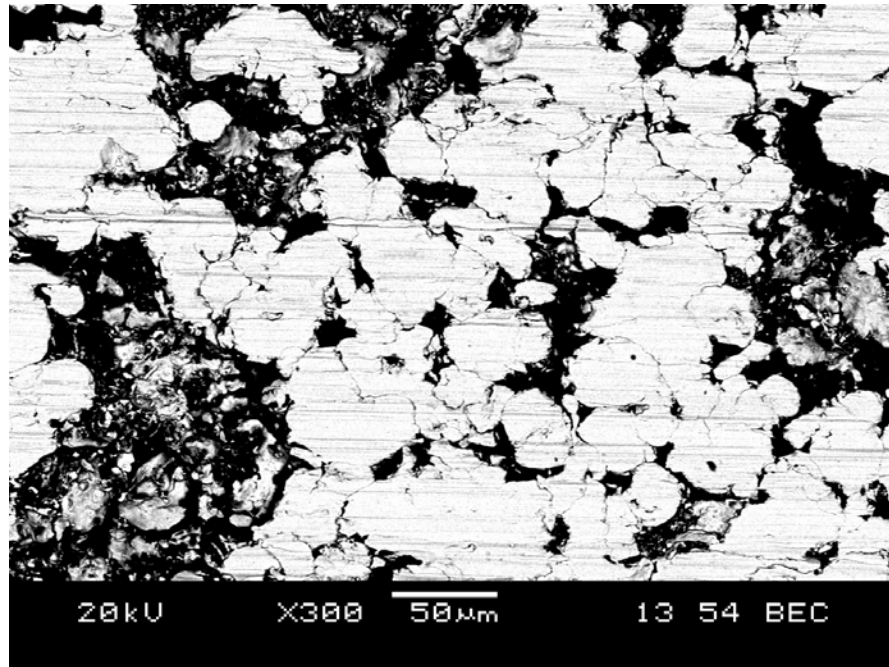
Figure 4 - 13: Scanning electron microscope (SEM) images of stainless steel powder-compacted samples No. 5-3 (center) for first layer (top surface).

Similarly, Figures 4-14 and 4-15 display the variation of local green density along sample's longitudinal axis for two compaction pressures of 372 and 565 MPa for sample thickness of 10, 15 and 20 mm, respectively. These heights are the final fabricated sample thickness not the thickness after grinding. As the graph shows, the green density is independent of the material thickness. Looking at Figure 4-14, one can see that relative density of sample size of 20 mm and 15 mm thick fabricated at 372 MPa compaction pressure does not show any increasing or decreasing density pattern. The same conclusion can be drawn from Figure 4-15 where the samples were fabricated at 565 MPa compaction pressure.
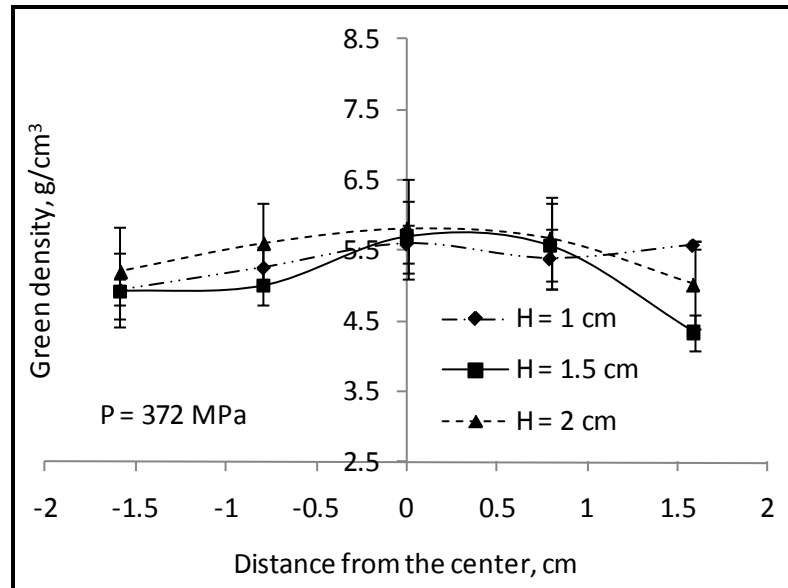
Figure 4 - 14: Variation of local green density along sample's longitudinal axis at given pressure (372 MPa) for three sample heights (top surface).
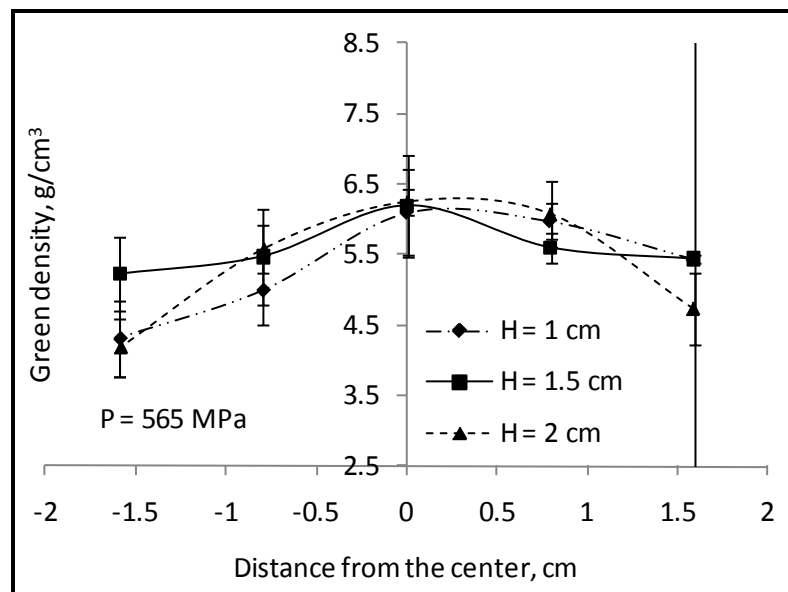

Figure 4 - 15: Variation of local green density along sample's longitudinal axis at given pressure (565 MPa) for three sample heights (top surface).

4.4 Effect of Pressure on the Relative Green Density

It is logical to expect that an increase in pressure results is an increase in density. However, it is important to study the degree of influence pressure has on relative green density. Figures 4-16 to 4-20 show the effect of pressure on the relative density for 10 mm thick sample. It can be deduced from the SEM images that the increase in pressure causes an increase in the relative density until the compaction pressure of 469 MPa at which point the density increases at slower rate that at lower pressures. This can be attributed to the fact that as the compaction pressure increases, the friction between metal powder and interlocking increases.
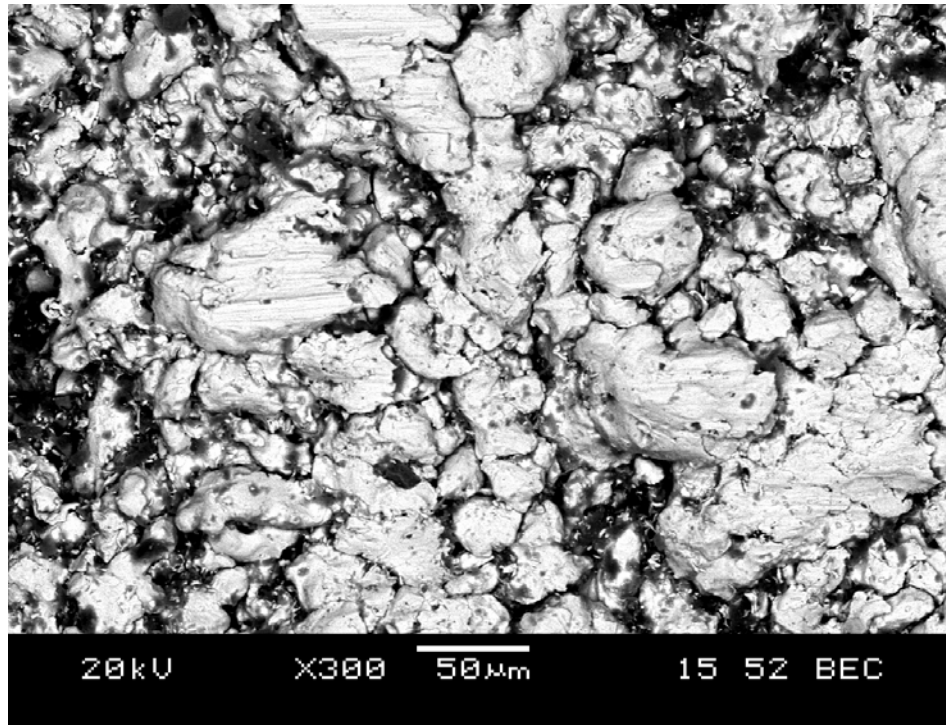
Figure 4 - 16: Scanning electron microscope (SEM) images of stainless steel powder-compacted samples No. 1-1 (center) for the second layer surface.
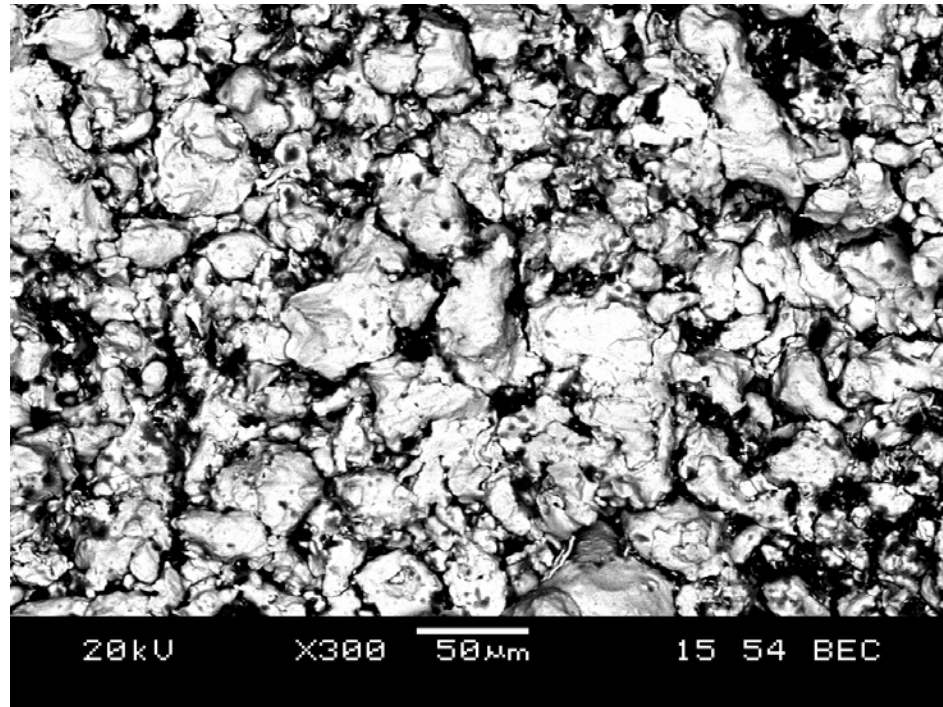
Figure 4 - 17: Scanning electron microscope (SEM) images of stainless steel powder-compacted samples No. 2-1 (center) for the second layer surface.
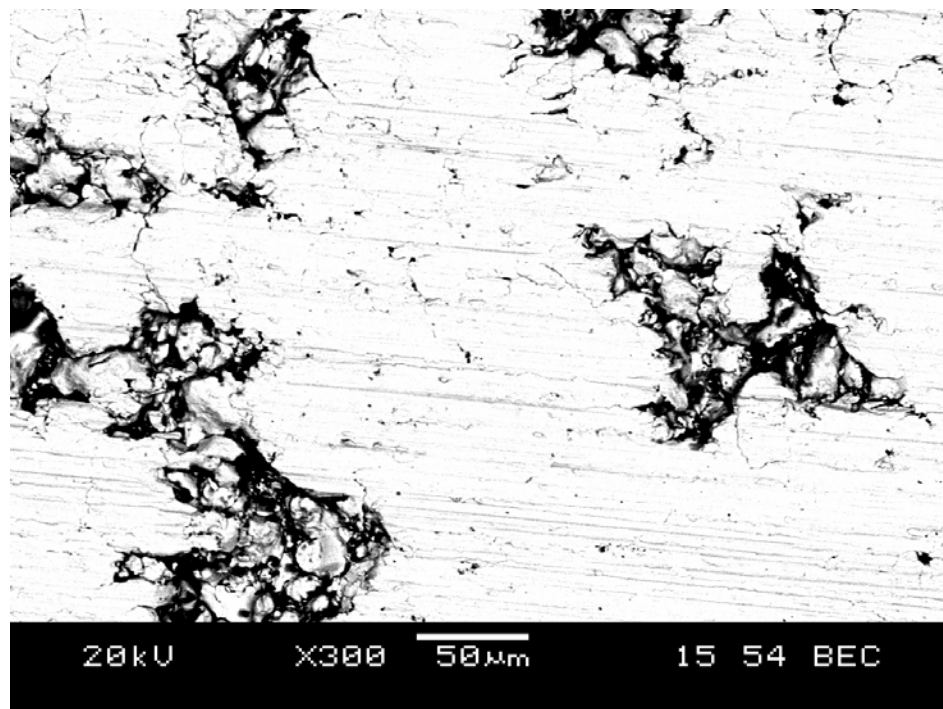
Figure 4 - 18: Scanning electron microscope (SEM) images of stainless steel powder-compacted samples No. 3-1 (center) for the second layer surface.
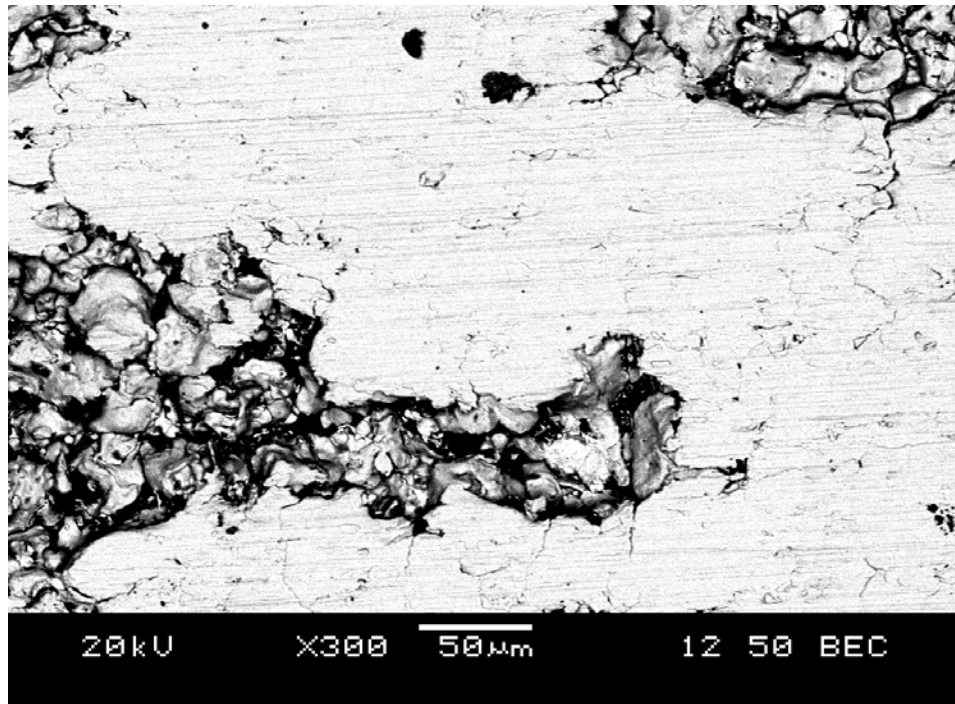
Figure 4 - 19: Scanning electron microscope (SEM) images of stainless steel powder-compacted samples No. 4-1 (center) for the second layer surface.
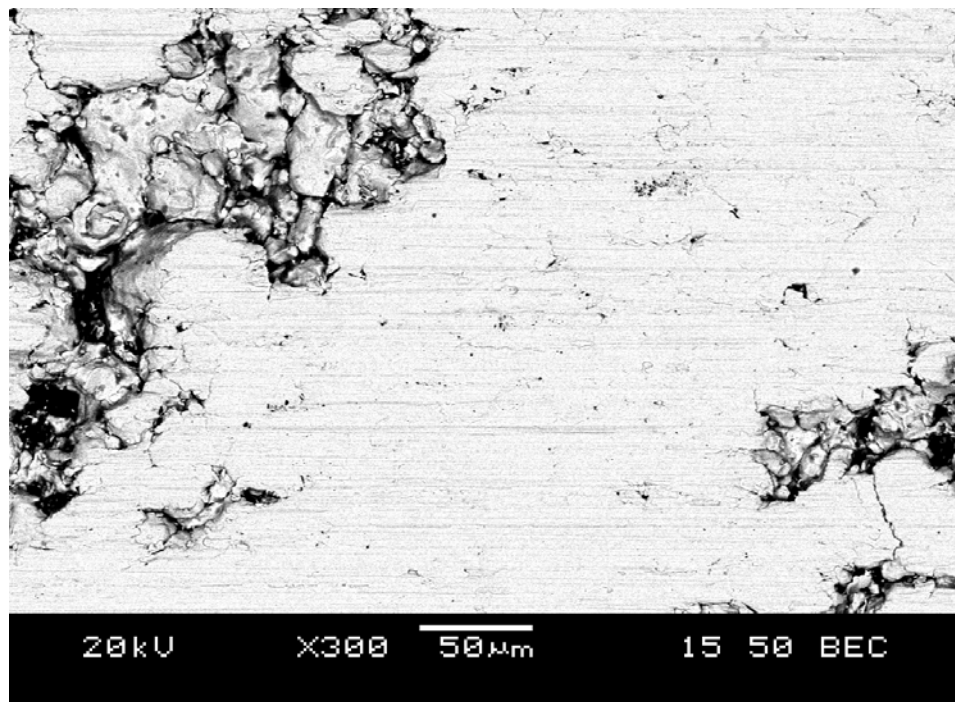

Figure 4 - 20: Scanning electron microscope (SEM) images of stainless steel powder-compacted samples No. 5-1 (center) for the second layer surface

At low compaction pressures, porosity will be present in the samples, but powder interlocking will be negligible. The occurrence of high density and/or strength in the un-sintered state does not necessarily equate with good machining characteristics. At higher values of green density, particle rearrangement is considerably less and the particles in contact are already plastically deformed. For the range of the parameters considered in this project, inhomogeneities in the density distribution obtained during filling and transfer only have a small effect on the final density distribution in the compacted component. Also, it is evident from Figures 4.15 to 4-20 that the density in the vicinity of the corner and edge is much lower than in the rest of the compact. This zone could be potentially detrimental, since cracking is more likely to be initiated in this region.

Figures 4-21 to 4-24, layer by layer, depict the density distribution and the influence of pressure. For instance, Figure 4-21 shows the relative green density distribution of the top layer of the 20 mm thick sample fabricated at all five aforementioned pressures. It can be observed that the relative density increases by increasing the compaction pressure. Additionally, the relative density appears to be higher at the center of the specimen than the edge of the specimen. This is caused by die body friction. Moreover, Figure 4-22 depicts the relative density at second layer of the 20 mm specimen. Figure 4-22 indicates an increase in relative density from top layer to the middle layer. This could be attributed to the fact that at sub-surface layers and middle of the sample, only friction between powders is present. Moving away from the center point to corner edges and to or bottom surface, additional friction between die and punch body with powder plays a role in the local relative density.
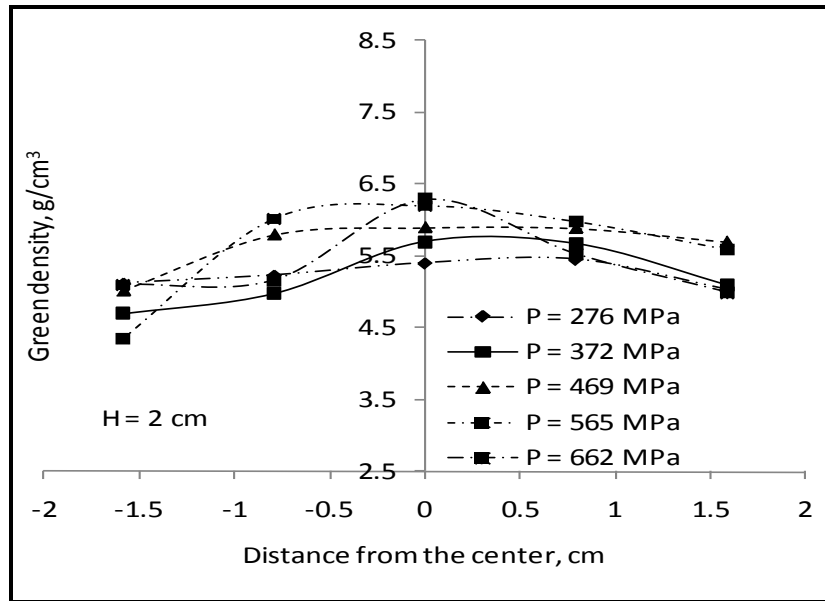
Figure 4 - 21: Variation of local green density along sample's longitudinal axis at given sample height for five compaction pressures (top surface).
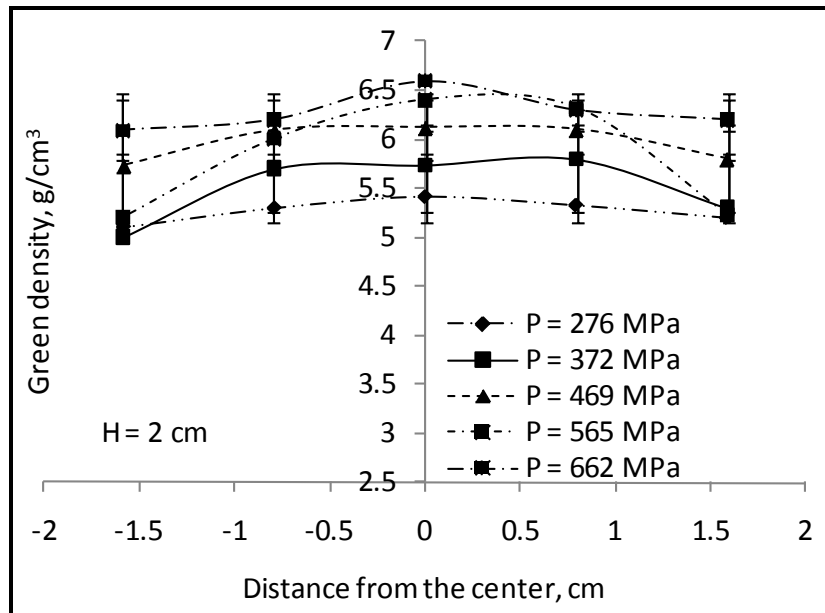
Figure 4 - 22: Variation of local green density along sample's longitudinal axis at given sample height for five compaction pressures (second surface).

41
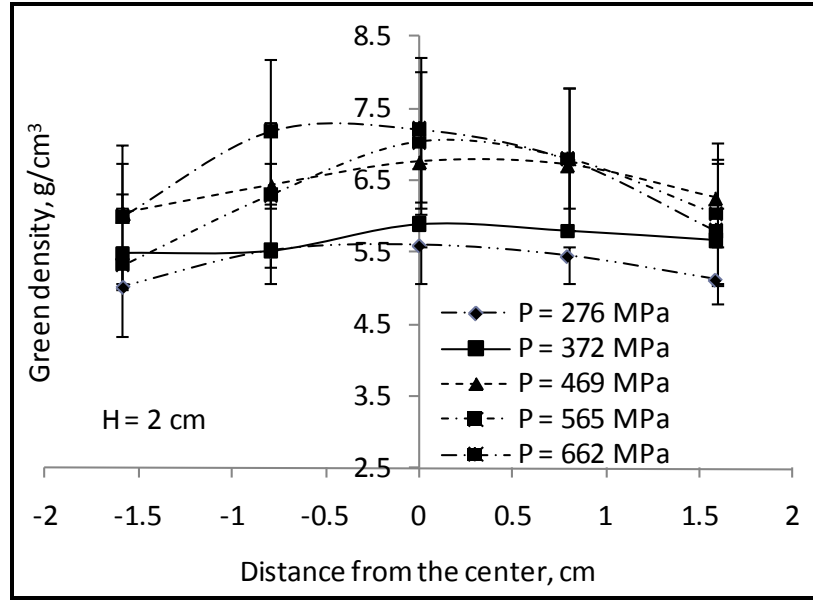
Figure 4 - 23: Variation of local green density along sample's longitudinal axis at given sample height for five compaction pressures (middle surface).
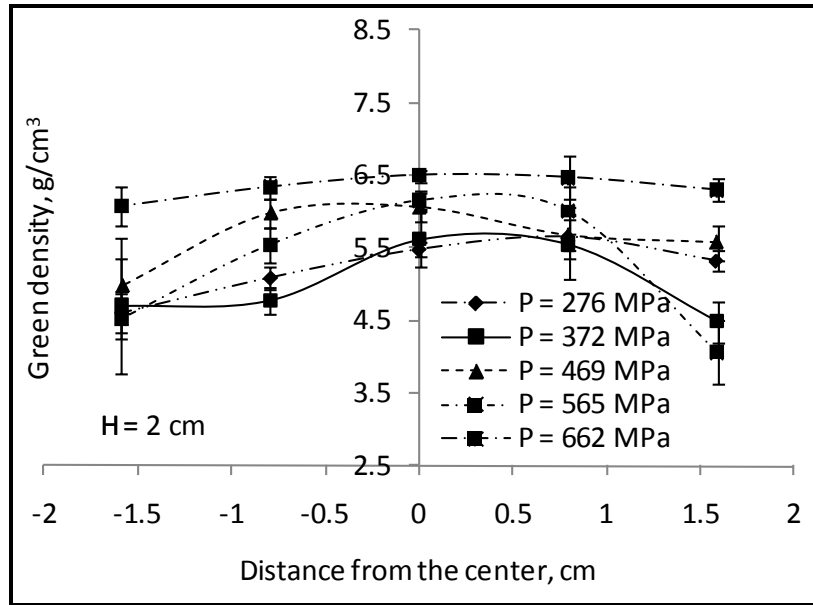
Figure 4 - 24: Variation of local green density along sample's longitudinal axis at given sample height for five compaction pressures (forth surface).

42

4.6 Local Variations of Porosity

One measure of the sample quality is the distribution of voids. This is particularly important since it shows the effect of friction between the particles and how the particles flow under compaction pressure. To study the distribution of the voids in the specimens, the SEM images were exported to MATLAB. A MATLAB program was developed to subdivide the images in both directions (x and y direction). The images were divided into 10 sections in each X and Y direction. Using MATLAB program, the void ration of each sub-image were determined. These information were collected as void ration versus location in X and Y-directions. Figures 4-25 and 4-26 depict the void distribution of 10 mm thick sample fabricated at 372 MPa compaction pressure.
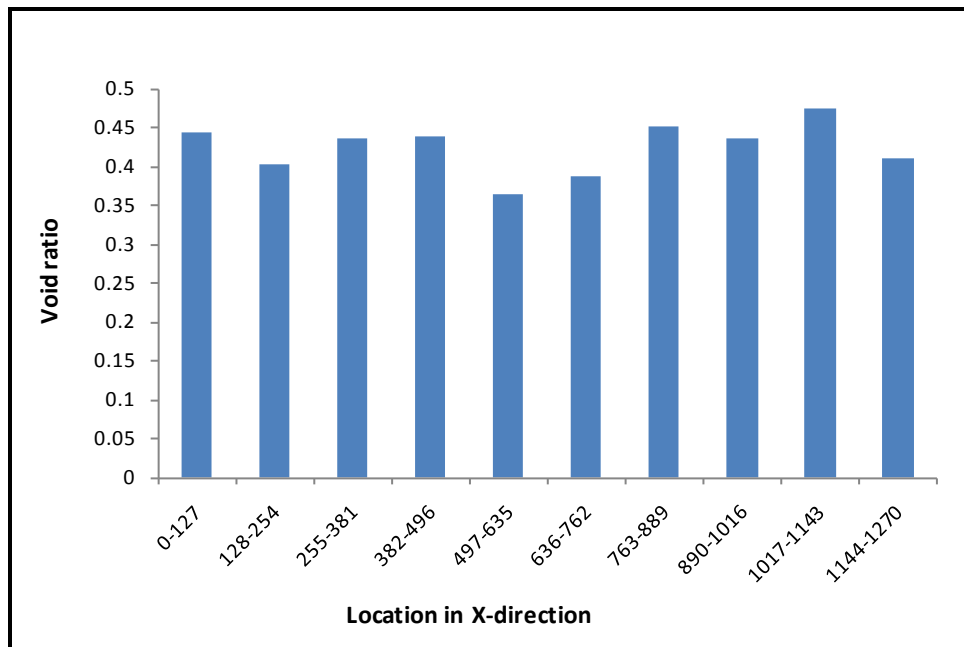
Figure 4 - 25: Variation of local Void ratio along sample's longitudinal X axis at mid-surface for specimen fabricated at 372 MPa compaction pressure
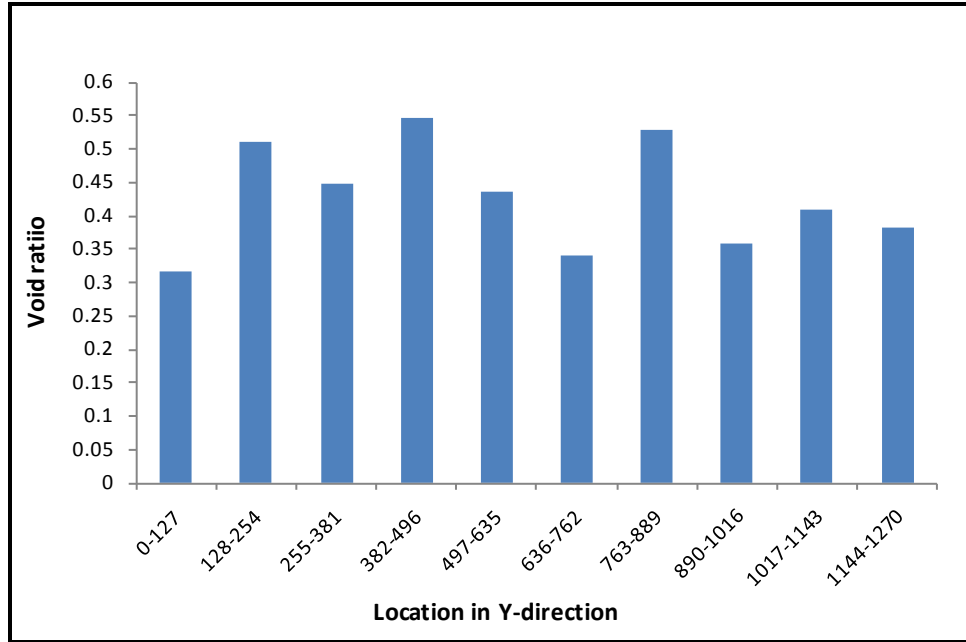
Figure 4 - 26: Variation of local void ratio along sample's longitudinal Y axis at mid-surface for specimen fabricated at 372 MPa compaction pressure

In addition to void ratio distribution, the standard deviations of the void distribution in x and y directions were computed. Moreover, the void standard deviation versus compaction pressure was studied. Figures 4-27 and 4-28 show the standard deviation of void ratio as a function of compaction pressure on top layer of 15 mm specimen. Figures 4-29 to 4-34 depict the void standard deviation as a function of compaction pressure for second layer, mid-surface layer and the fourth layer, respectively. It is intuitive to assume that higher pressure results in lower void ratio, or higher relative green density. In fact, the increase in pressure for the specimens tested here clearly shows this behaviour. However, upon close inspection of the graph of standard deviation of void ratio, one can deduce that the void distribution is random and does not follow a specific pattern. The void distribution could be attributed to the bridging of powder particle during the filling, a phenomenon that is reduced by vibratory technique but never eliminated because of various powder sizes.

44
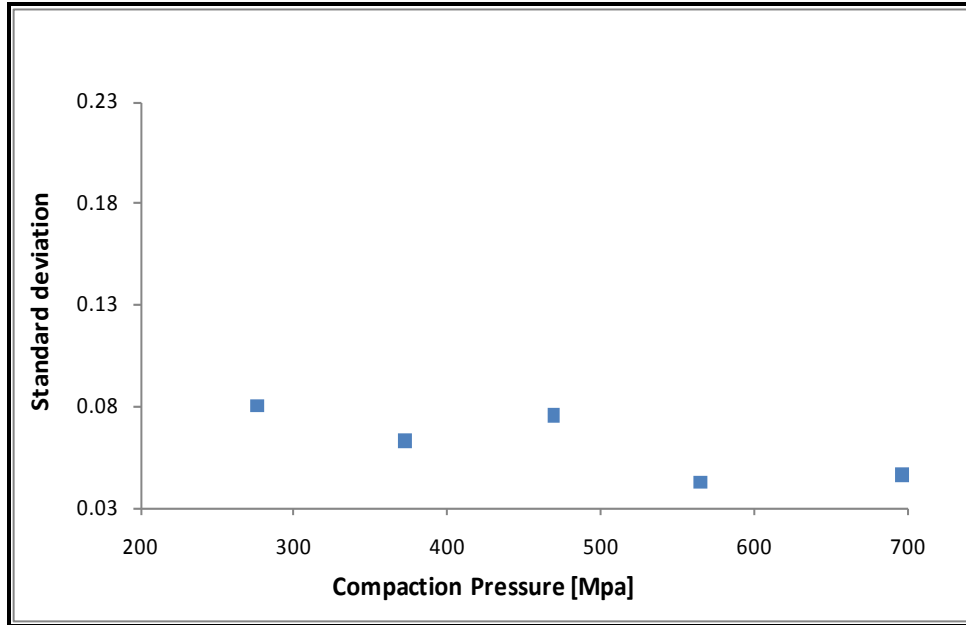
Figure 4 - 27: Standard deviation of local Void ratio along sample's longitudinal X axis at top layer for 15 mm specimen under various compaction pressures
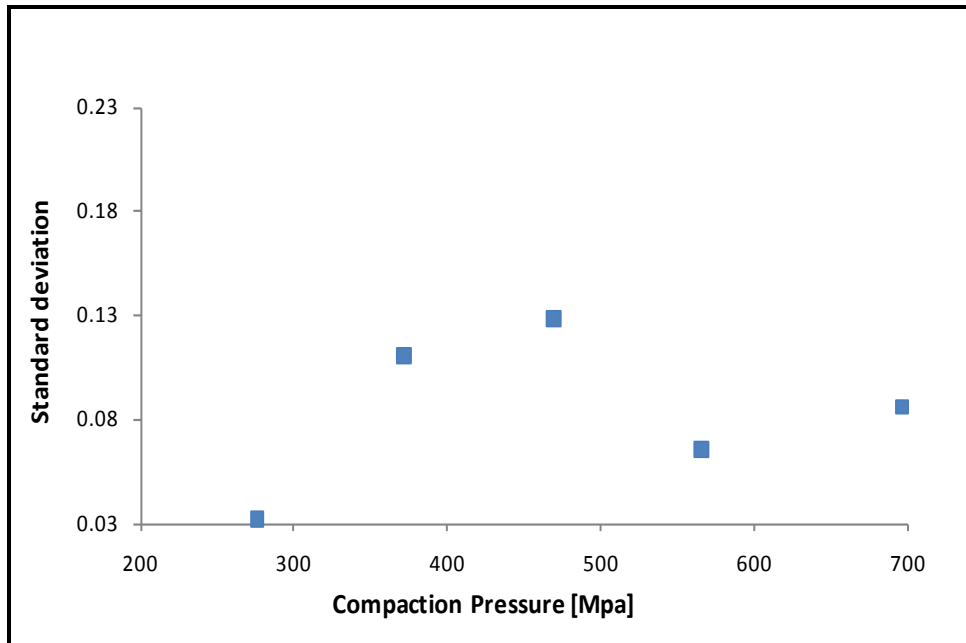
Figure 4 - 28: Standard deviation of local Void ratio along sample's longitudinal Y axis at top layer for 15 mm specimen under various compaction pressures
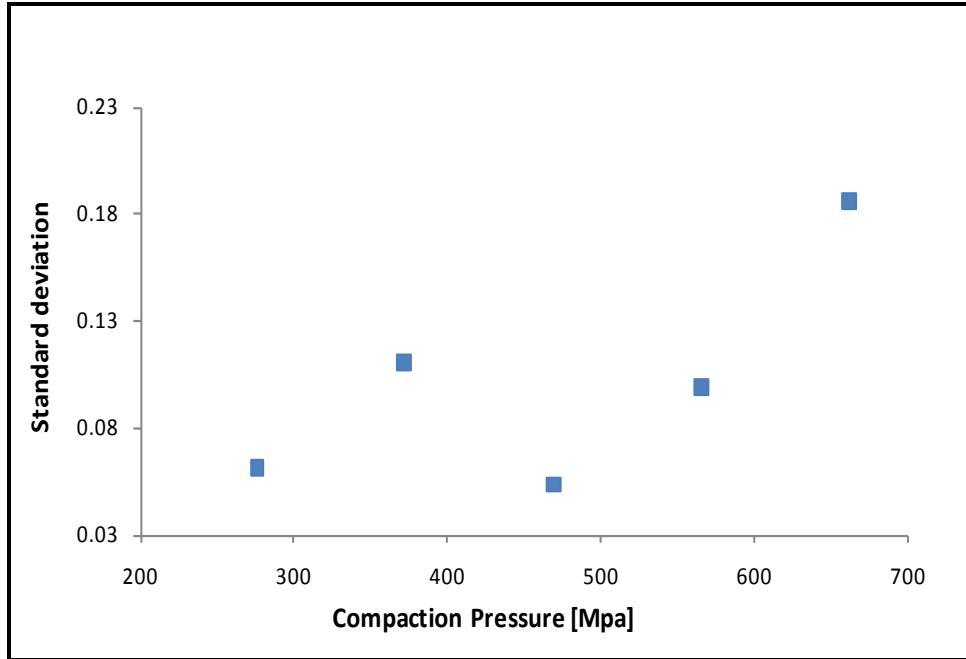
Figure 4 - 29: Standard deviation of local Void ratio along sample's longitudinal X axis at second layer for 15 mm specimen under various compaction pressures
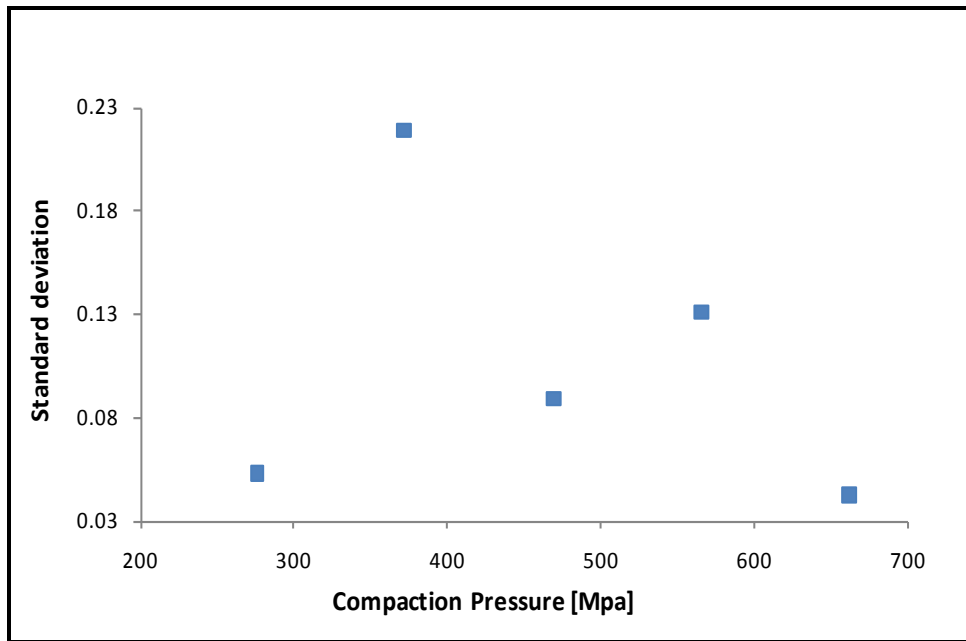
Figure 4 - 30: Standard deviation of local Void ratio along sample's longitudinal Y axis at second layer for 15mm specimen under various compaction pressures
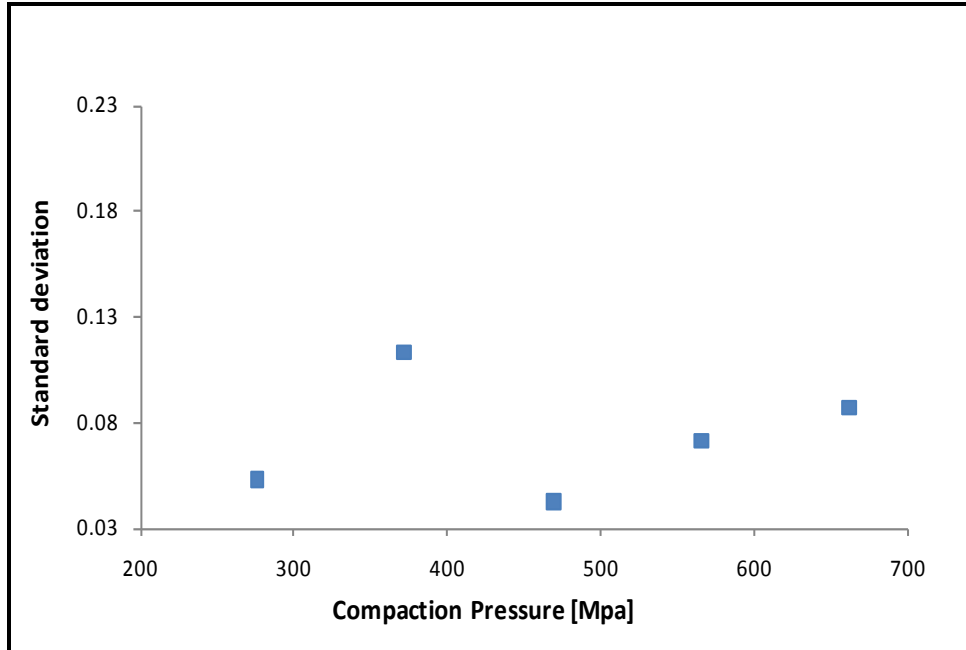
Figure 4 - 31: Standard deviation of local Void ratio along sample's longitudinal X axis at middle surface layer for 15 mm specimen under various compaction pressures
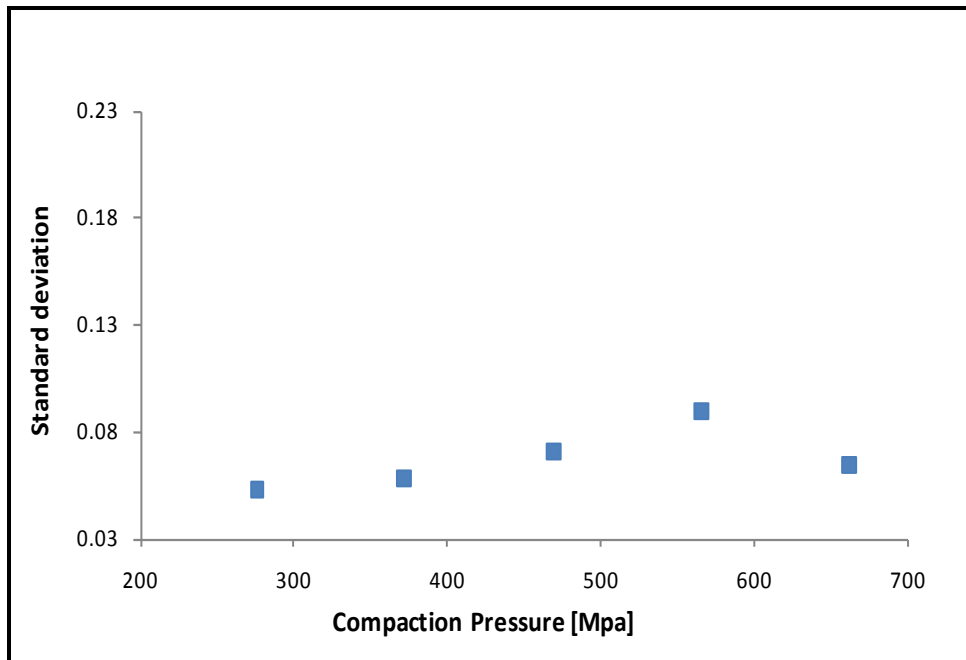
Figure 4 - 32: Standard deviation of local Void ratio along sample's longitudinal Y axis at mid surface layer for 15mm specimen under various compaction pressures
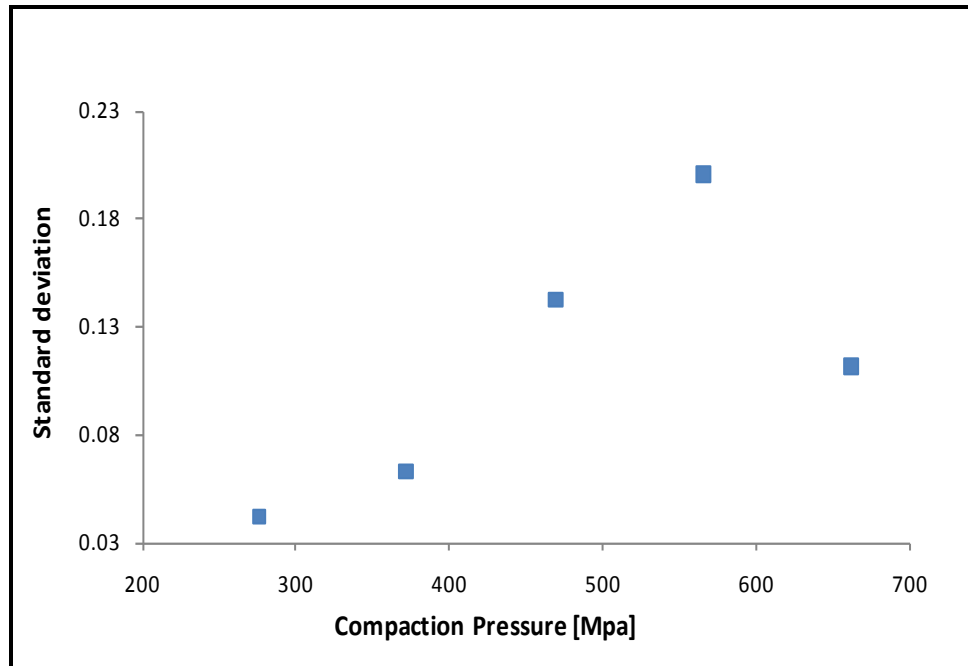
Figure 4 - 33: Standard deviation of local Void ratio along sample's longitudinal X axis at fourth layer for 15mm specimen under various compaction pressures
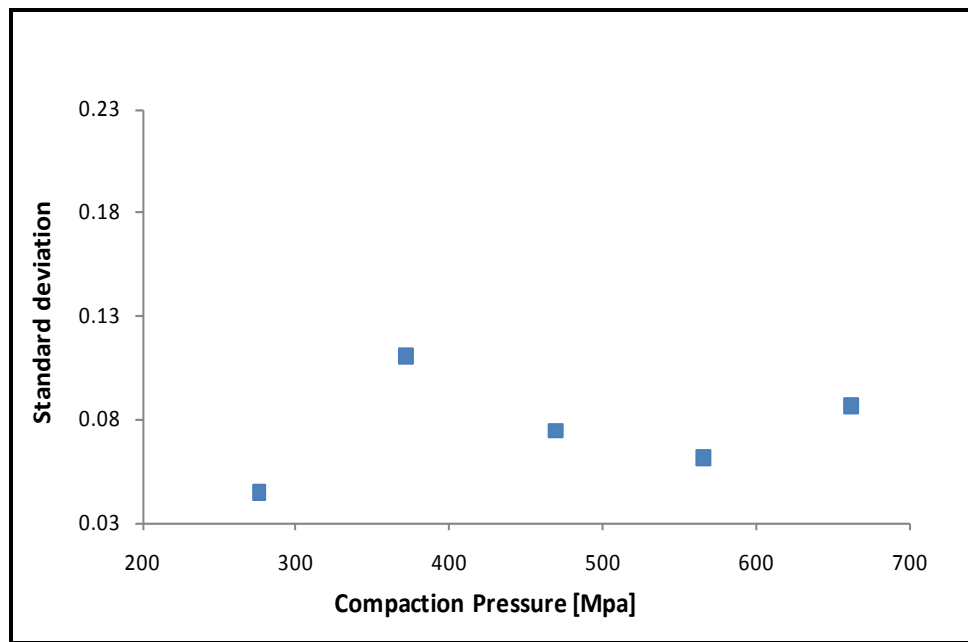
Figure 4 - 34: Standard deviation of local Void ratio along sample's longitudinal Y axis at fourth layer for 15mmspecimen under various compaction pressures

Furthermore, as discussed in previous sections, the relative green density at the center of the mid layer of the specimen was measured to be the highest in all compaction pressures. This was due to the fact that the effect of the die wall and punch frictions vanish and only inter-particle frictions exist. To further study this effect, the standard deviation of the void ratio vs. the layer was graphed. Figure 4-35 depict a typical standard deviation distribution as a function of layer location for 15 mm thick specimen fabricated at 469 MPa. As the graph indicates the deviation of void distribution decreases from the top layer to the mid surface layer.
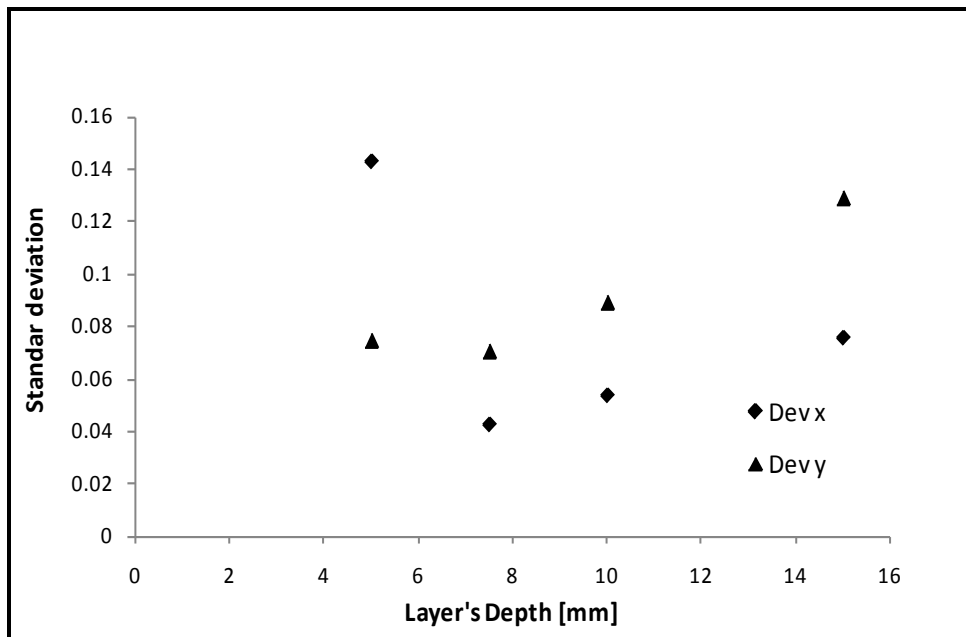
Figure 4 - 35: Standard deviation of average Void ratio at four layers of 15 mm thick sample fabricated at 469 MPa.

4.4 Cold Welding and Density Distribution

The behaviour of the cold compaction process of iron powders is dependent on factors such as tool kinematics, material properties of the powder and frictional sliding at the tool–powder interface. During compaction the particles experience frictional forces between each other in the specimen. On the other hand, at the die-powder or punch-powder boundary, they experience frictional forces due to punch and die body as well as powder themselves. Another

phenomenon observed during the fabrication was that the powder seems denser at the center as compared to the top surface. In other words, the tap density appeared to be higher at the center layer of specimen than anywhere else. This is primarily due to the fact that smaller powder particles tends to migrate to lower layers during tapping phase, therefore causing higher tapped density at the center layer compared to other regions. Naturally, under compaction, the higher tapped density and lack of frictional forces due to die and punch body combined has the net effect of higher density at the center layers. This was observed in all samples tested regardless of compaction pressure.

At high compaction pressures powder particles are bonded together by mechanical interlocking of powders or by cold welding. The mechanical interlocking generally happens at lower compaction pressures while cold welding occurs at high compaction pressures. At a high pressure, the particles contact area increases due to particle deformation at contact interface. Continuous deformation of contacting particles and continuous increase of interface contact area takes place and eventually the cold welding of the contacting particle occurs. This is shown in Figure 4-36 and 4-37. Figure 4-36 shows the center point of the mid surface layer of 20 mm thick sample fabricated at 276 MPa compact pressure and Figure 4-37 shows the same location on sample fabricated at 662 MPa.

As Figure 4-36 indicates, the specimen fabricated at 276 MPa pressure does not show cold welding at the boundary of the grains and the grain interlocking is visible. On the other hand, the grain boundaries in Figure 4-37 are less visible indicating the occurrence of the cold welding phenomenon. The powder interlocking is prominent in lower pressures and gradually is replaced with cold welding as the compaction pressure increases.
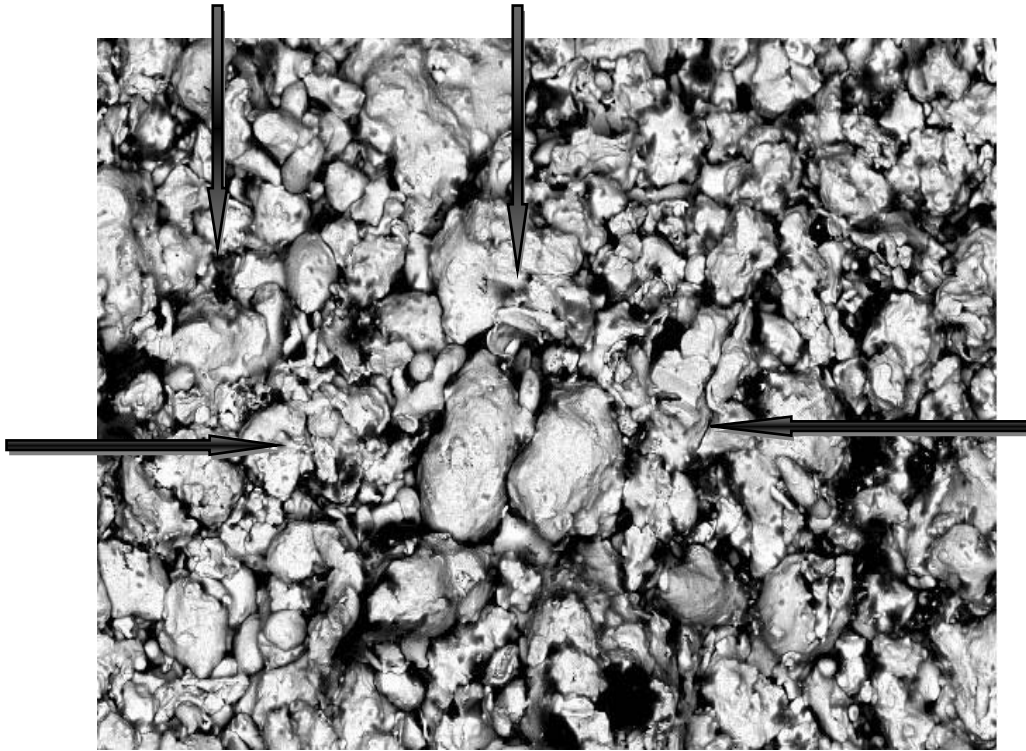
Figure 4 - 36: Grain boundary of sample size 20 mm thick on mid surface layer fabricated at 276 MPa. The arrows show the boundary and interlocking of grains
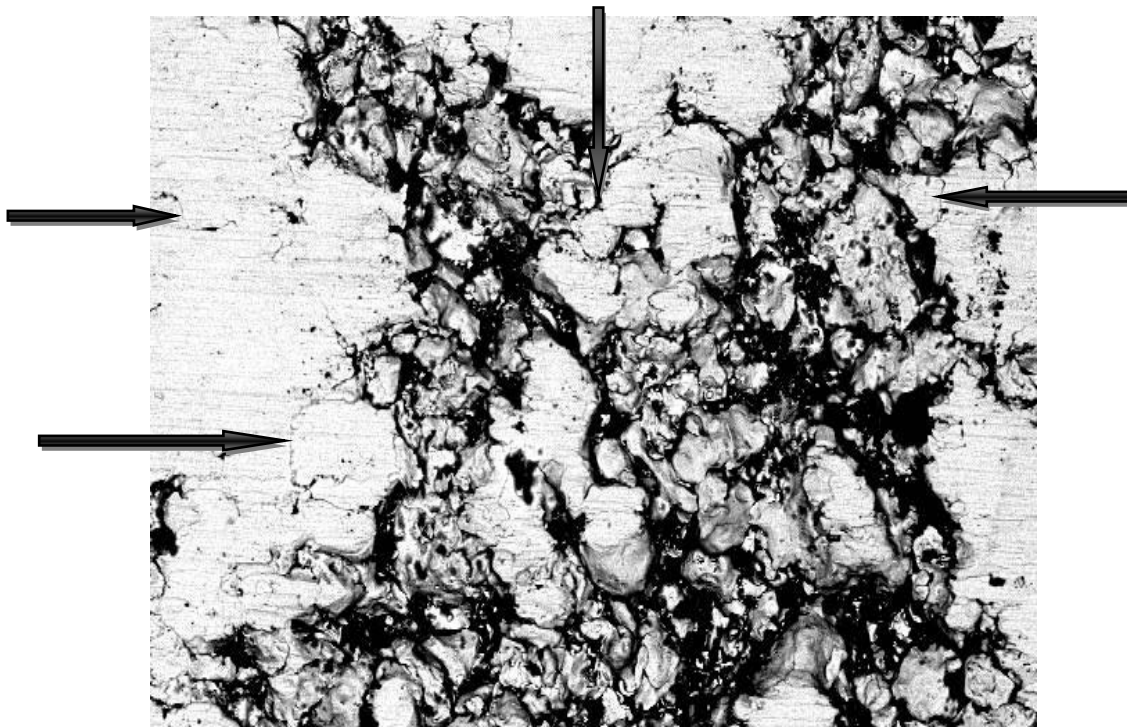
Figure 4 - 37: Grain boundary of sample size 20 mm thick on mid surface layer fabricated at 662 MPa. The arrows show the boundary and cold welding of grains

Chapter 5

Neural Network Analysis

5.1 Introduction

In this chapter artificial neural network (ANN) modelling of green compact density variations is discussed. The neural network architecture and comparison between experimental results and ANN's results is also presented.

5.2 Neural Networks

Neural networks are computational models based on the human brain. They consist of a number of interconnected neurons. ANNs operate by simulating the ability of biological neural systems to perform complex decision making tasks, without any prior programming. In recent years, a considerable research effort has gone into the development of ANN data analysis, function approximation, sensor processing, and control [51, 52].

Significantly, their ability to perform complex non-linear mappings can be used for approximating multiple input, multiple output relationships. Generally there are two schemes of neural network, supervised and unsupervised network. Supervised network are used when a desired output is of interest in respond to input. Unsupervised network are networks that are continuously adjusted the output to new input parameters. In this study, supervised network was utilized.

ANNs are used in a number of applications where the observed phenomenon is either too complicated to model using conventional tools or is not clearly understood. Such applications involve classification and function-mapping or approximation problems, which exhibit a degree of imprecision. However, an ANN can be trained iteratively from examples to learn and represent the complex relationships represented within the data. In fact the general applicability of the technique has been demonstrated by the proof that feed-forward networks with a single hidden layer, having sufficient number of neurones, using threshold or sigmoid activation function, are universal approximations [53]. The number of connections, how these connections are arranged, and the nature of the connections determine the architecture of the network. Figure 5-1 shows the schematic representation ANN programming.
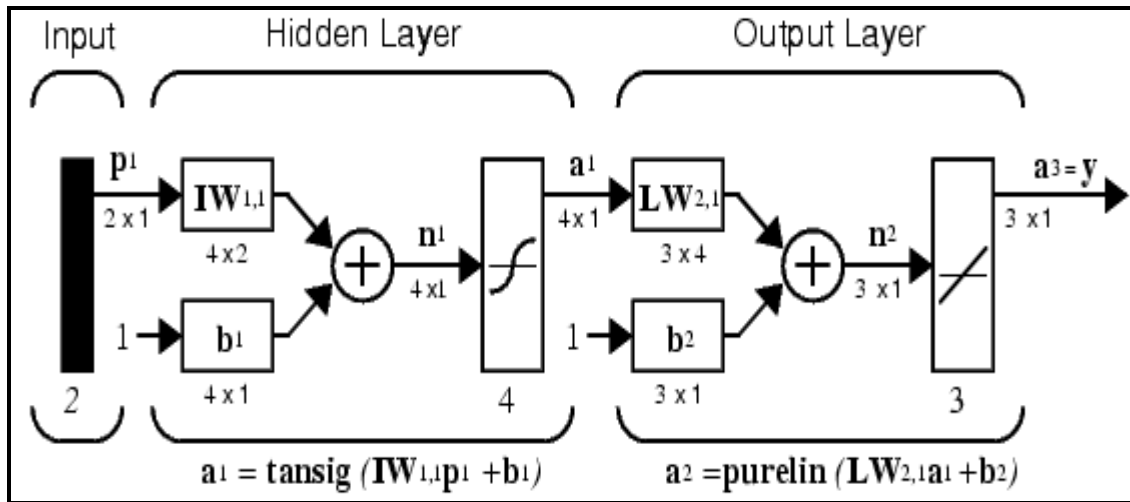
Figure 5 - 1: Schematic of the structure of a multilayer feedforward neural network. [54]

The feed-forward, back-propagation (or multilayer perceptron, MLP) neural network is the most commonly used for input-output modelling [55], and is used as the architecture of the networks for this study. Artificial neural networks have the ability to 'learn' complex, non-linear interactions through the training and updating of the synapse weights connecting each neuron.

The training algorithm governs the strengths of the connections and how they are adjusted or trained to achieve a desired overall behaviour of the network [56].

5.2 Neural Modeling of compaction

The modelling problem in powder compaction can be thought of as a continuous non-linear mapping from '*n*-dimensional property space' to '*m*-dimensional process parameter space'. In this study, a multilayer neural network model consisting of three input layer, one hidden layer, and one single-variable output layer was used to create a neural model of the compaction process. The ANN was trained and implemented using neural network toolbox in the MATLAB R2009a using back-propagation learning rule with Levenberg-Marquart algorithm [56].

The experimental data of local green densities on sample surfaces were employed to train the neural network. The input variables of the ANN consisted of compaction pressure, height of the samples and the distance from the edge of samples. The output was the local density in different distances. The neural model was then used to predict the green density. Once these input and output parameters are set, the ANN training can start.

Of the total number of training data, 70% were allocated for training the neural network while the 15% of the remaining 30% were used for evaluation of generalization abilities of the trained network and to stop training before over fitting and finally the last 15% were used as a completely independent test of network generalization. The number of hidden nodes was chosen by optimizing this generalization capability of the network. This is a critical step, since if too many hidden nodes are chosen; the generalization will suffer while if too few nodes are chosen the ability of the network to learn the patterns of data will be affected. It was determined that 150 nodes resulted in output with least amount of error and best generalization.

In the early stopping method, the available data were divided into two subsets. The first subset was the training set, which was used for computing the gradient and updating the network weights and biases. The second subset was the validation set. The error on the validation set was monitored during the training process. The validation error normally decreased during the initial phase of training, as did the training set error.

However, when the network begins to over fit the data, the error on the validation set will typically begin to rise (see Figure 5-2 , which is an example drawn by using MATLAB). When the validation error increases for a specified number of iterations, the training is stopped, and the weights and biases at the minimum of the validation error are returned. The test set error is not used during the training, but it is used to compare different models. It is also useful to plot the test set error during the training process. If the error in the test set reaches a minimum at a significantly different iteration number than the validation set error, this may indicate a poor division of the data set [54]. Figure 5-2 depicts the convergence of least square error optimization as the function of training data iteration. As shown, the error is relatively high at the beginning of the training phase. As the number of iteration increase, the least square error decreases. However, the error starts diverging after (increases) as the data iteration increases. At the point that error is a minimum, MATLAB software automatically stops the training.
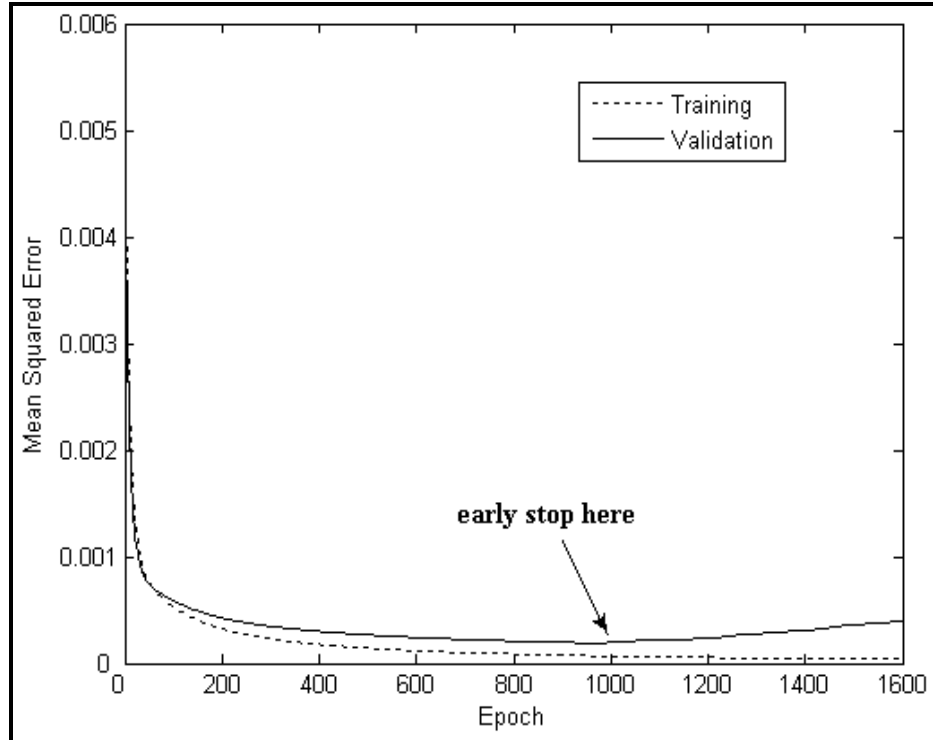
Figure 5 - 2: Early stopping method [54]

5.3 Neural network results

To determine the predictive capability of the trained neural network, the relative densities were obtained by the neural network at various locations and at various pressures. Table 5-1 shows the ANN's results of a 20 mm thick specimen fabricated at 469 MPa pressure at top surface. The measurements were taken from the top surface (first layer), along the longitudinal axis of a 20 mm thick specimen. In this work, all specimens have the same cross sectional dimension of 31.75 mm (longitudinal) and 12.275 mm (transverse), but varying thickness. Three measurements were taken in transverse direction and the results were averaged. This measurement process was followed along the longitudinal direction at five locations presented in Table 5-1. Note that 0 refers to the center location and ± 15.875 mm refers to the location near

the die body (see Figure3-1). As it can be seen, the neural network resulted in overall average error of 2.2% for sample data presented in Table 5-1.

Table 5 - 1: Comparison of experimental and neural network result at pressure 469 MPa and 20 mm thickness on top surface

Distance from the center of the sample's surface (mm)	Measured experimental density	Neural network (NN) predicted density
15.875	5.09	5.4460
7.9375	5.59	5.5902
0	5.68	5.6802
-7.9375	5.6	5.5999
-15.875	5.11	5.3147
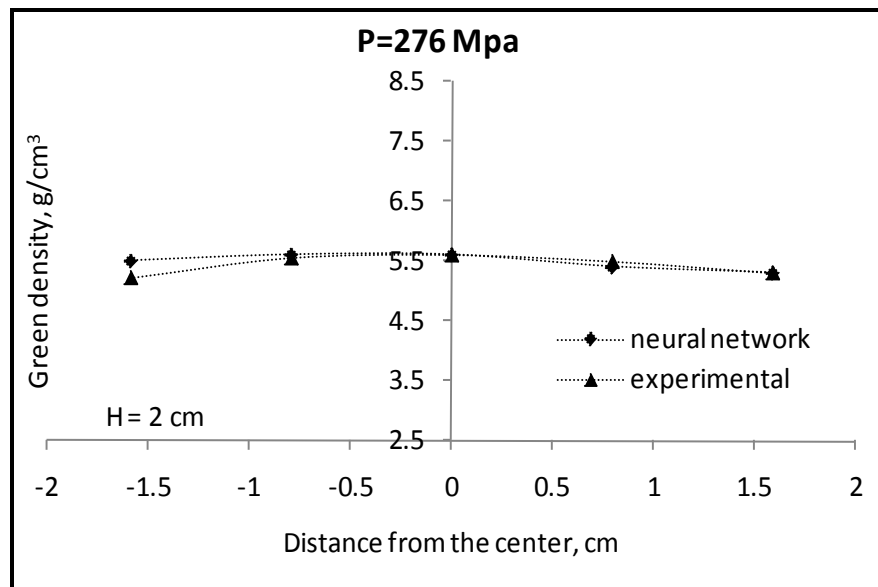
Figure 5 - 3: Comparison between neural network predicted local green density and experimental results along sample's longitudinal axis at middle surface of samples height (H = 2 cm, P = 276 MPa)
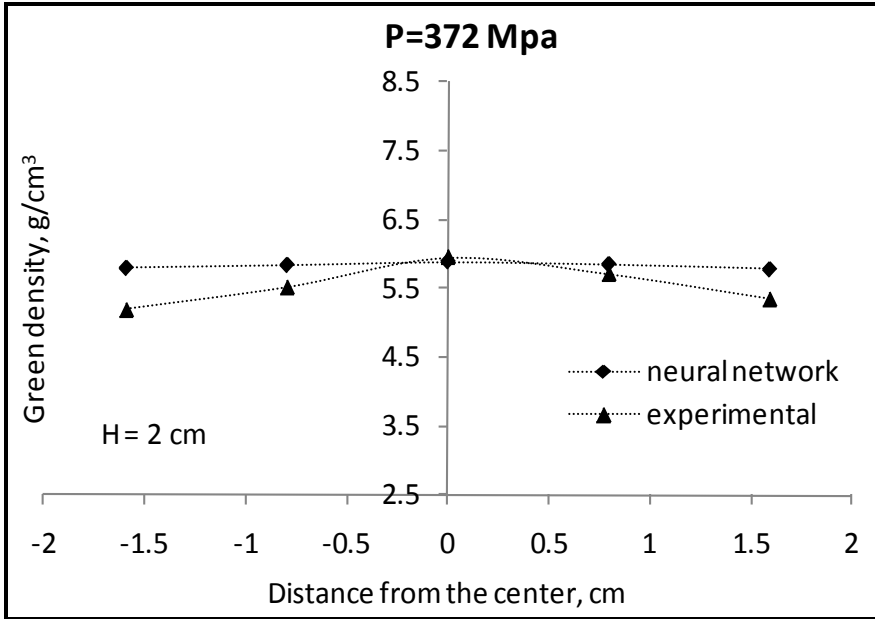
Figure 5 - 4: Comparison between neural network predicted local green density and experimental results along sample's longitudinal axis at middle surface of samples height (H = 2 cm, P = 372 MPa)
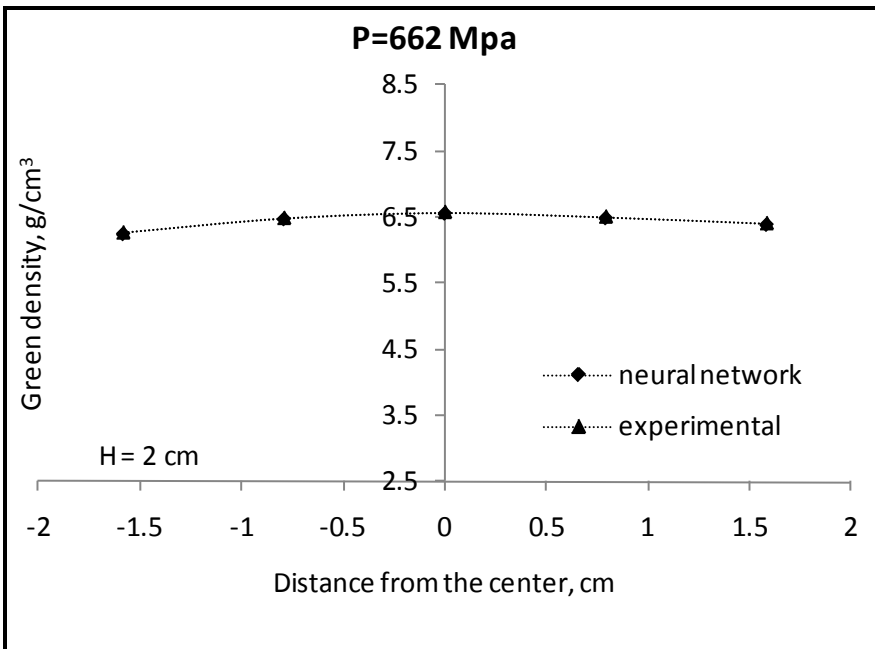
Figure 5 - 5: Comparison between neural network predicted local green density and experimental results along sample's longitudinal axis at middle surface of samples height (H = 2 cm, P = 662 MPa)

Figures 5-3 to 5-5 depict green densities on sample's middle surfaces obtained from neural model. Figure 5-3 shows the variation of green density distribution (five points on longitudinal

58

axis) on the mid surface layer of specimen fabricated at 276 MPa. Likewise, Figures 5-4 and 5-5 show the density distribution on the mid surface layer of specimen fabricated at 372 MPa and 662 MPa, respectively. In general, an increase in the overall green density of the sample can be observed as a result of an increase in the compaction pressure. The predicted results by ANN show an excellent agreement with the experimental results at high pressure. On the other hand, there is more discrepancy between the ANN's predicted and the experimental results at sub-layers below the mid surface. However, the ANN's predicted results are well within acceptable range with 1.1% deviation from experimental results for compaction pressure of 662 MPa and 2.3% deviation from experimental results for 276 MPa.

Additionally, it was imperative to study the predictive capability of the ANN's results for all four layers for a given pressure. Figures 5-6 (a), (b) and (c) show the neural network and experimental results of compaction pressure of 662 MPa in mid-surface layer for three sample thicknesses. Moreover, Figures 5-7 (a) and (b) show the neural network and experimental results of compaction pressure of 469 MPa at various surface layers in the 20 mm thick sample. Table 5-2 lists the results of neural network and experimental data for compaction pressure of 662 for various sample thicknesses. While Table 5-3 shows the results of the ANN for various layers for the 20 mm thick specimen.

H=1 cm

Green density, g/cm³

P = 662 MPa

Distance from the center, cm

neural network

experimental

(a)

H=1.5 cm

Green density, g/cm³

P = 662 MPa

Distance from the center, cm

neural network
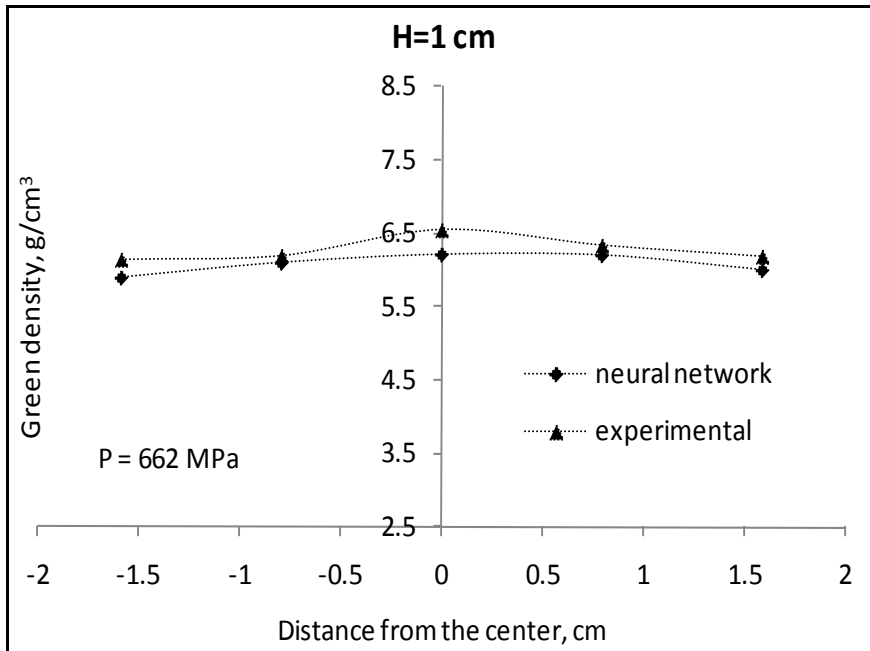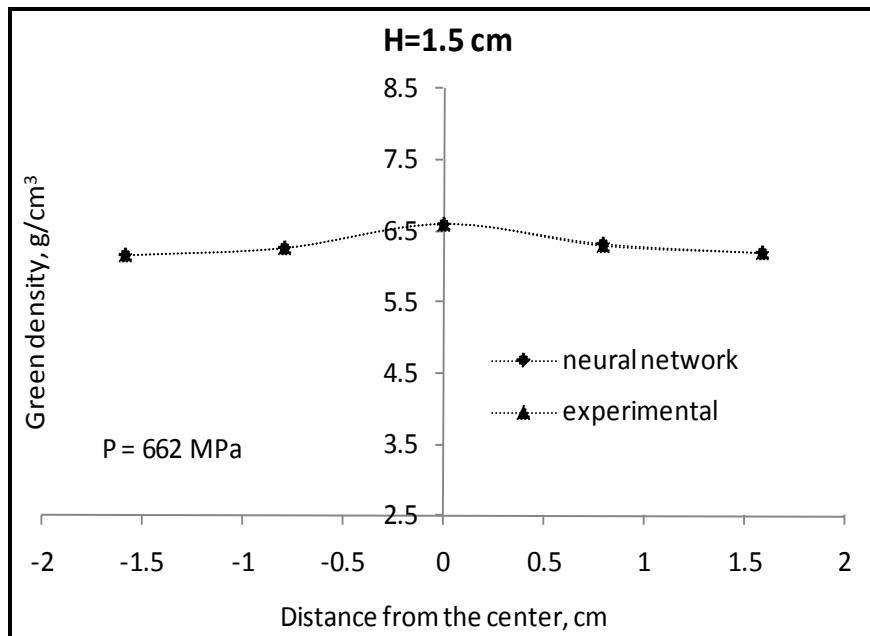
experimental

(b)

Figure 5 - 6: Variation of experimentally determined and neural network predicted local green density at compaction pressure of P=662 MPa on the center of the specimen for middle layers, a) H=1 cm, b) H=1.5 cm and c) H=2 cm
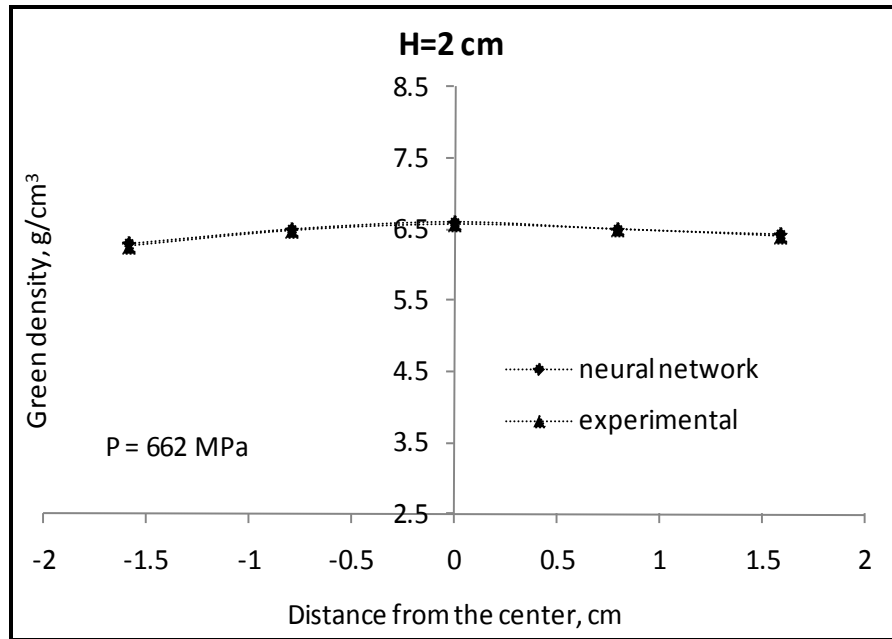
(c)

Figure 5 - 6 (continues): (c) H = 2 cm
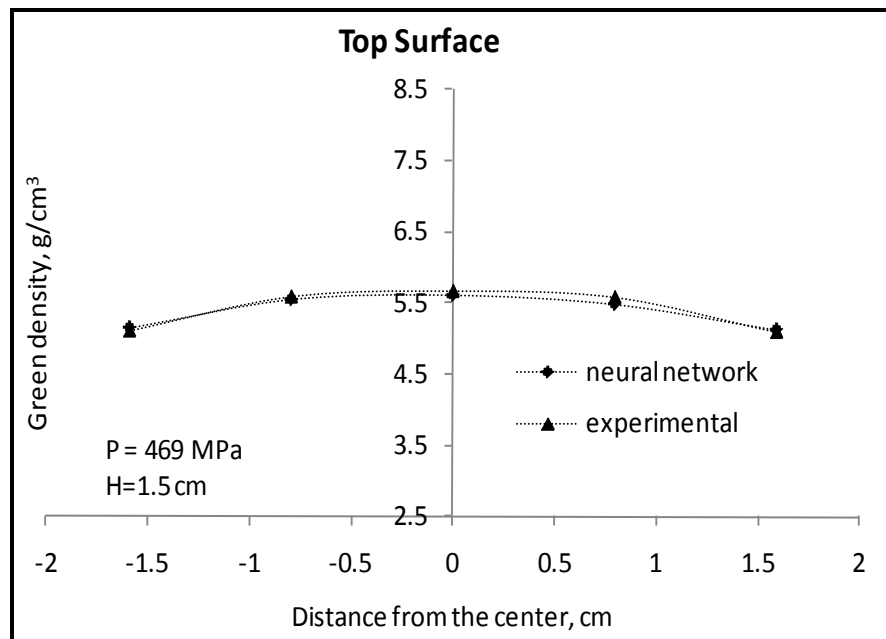
(a)

Figure 5 - 7: Variation of experimentally determined and neural network predicted local green density at compaction pressure of P=469 MPa on the center of the specimen for H=1.5 cm a) Top surface, b) Second Surface, c) Middle Surface, and d) Forth surface
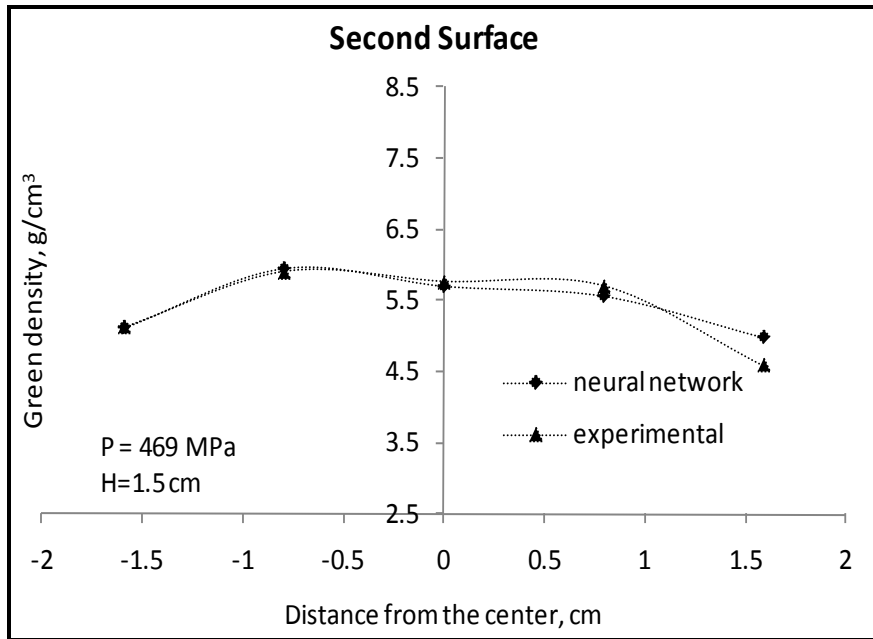
(b)
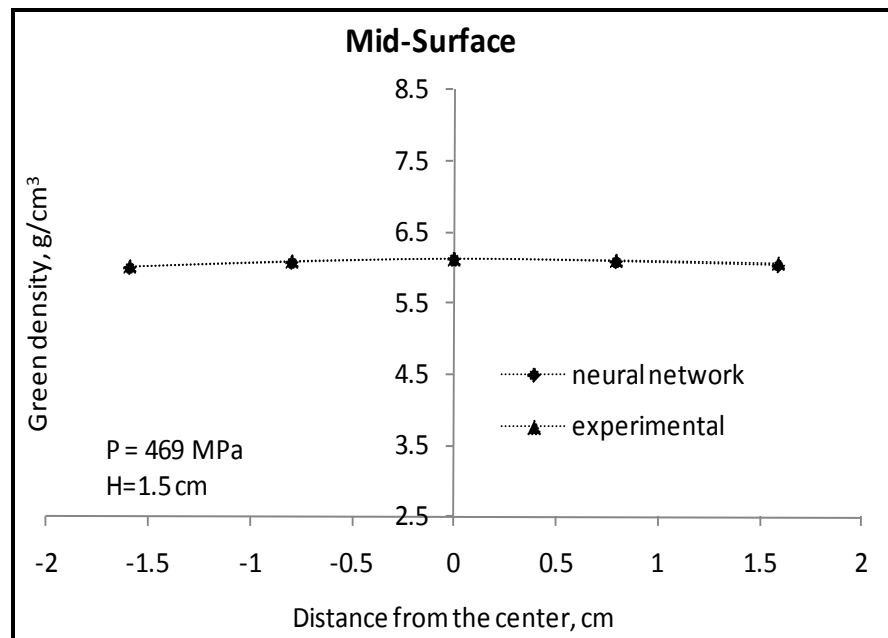
(c)

Figure 5 - 7 (continues): (b) second surface and (c) middle layer surface
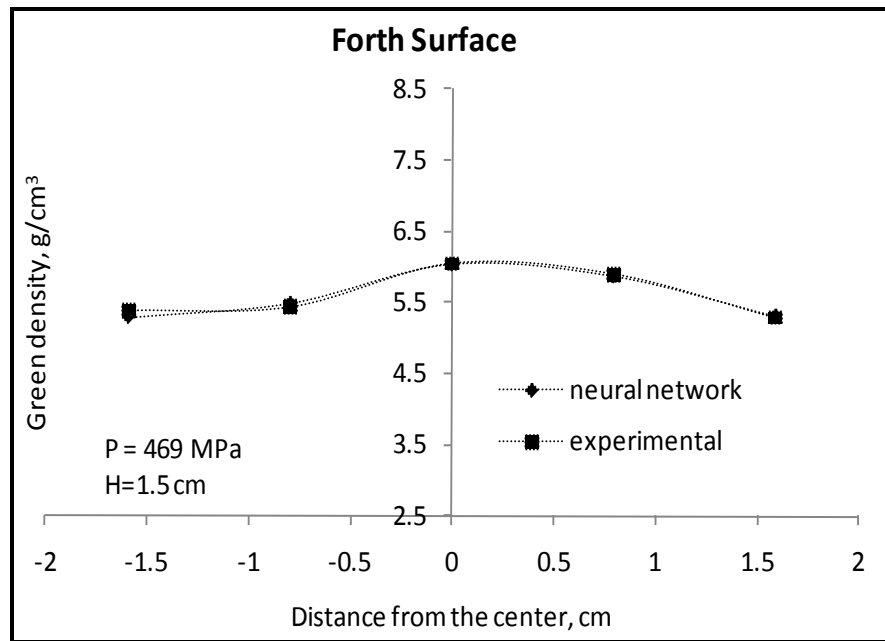
(d)
Figure 5 - 7 (continues): (d) fourth layer surface

Table 5 - 2: Comparison of experimental and neural network result at pressures 662 MPa at various thicknesses in middle surface

	Experimental density			Neural network density		
	Sample thickness			Sample thickness		
Distance	10 mm	15 mm	20 mm	10 mm	15 mm	20 mm
1.5875	6.19	6.2	6.4	6.12	6.21	6.43
0.79375	6.34	6.3	6.5	6.3	6.33	6.5
0	6.55	6.6	6.57	6.6	6.7	6.6
-0.79375	6.2	6.27	6.48	6.3	6.29	6.5
-1.5875	6.15	6.17	6.26	6.15	6.18	6.3

Table 5 - 3: Comparison of experimental and neural network result at pressure 469 MPa for various layers

Location on longitudinal axis		first layer	Second layer	mid surface	fourth layer
1.5875	Exp	5.09	4.59	6.06	5.29
	Neural	5.12	4.98	6.03	5.32
0.79375	Exp	5.59	5.7	6.1	5.9
	Neural	5.48	5.56	6.09	5.88
0	Exp	5.68	5.76	6.12	6.05
	Neural	5.61	5.7	6.13	6.05
-0.79375	Exp	5.6	5.9	6.09	5.44
	Neural	5.55	5.95	6.08	5.5
-1.5875	Exp	5.11	5.13	6.02	5.39
	Neural	5.15	5.12	6.006	5.3

5.4 Conclusions

The goal in this chapter was to evaluate neural network modeling as a method to reproduce density variations during compaction process in powder metallurgy. Neural network was used to predict the green density as the function of compaction pressure and determination of density distribution in any desired location.

The main quality indicator of a neural network is its generalization ability, i.e., its ability to predict accurately the output of un-tested data. It has been demonstrated that MLP architecture with the back-propagation learning algorithm can be successfully used as a tool for predicting the green density. In some instance the output of the neural network models shows an averaging affect that brings out a more continuous pattern of change in the density distribution. This could be a result of averaging of measured values and benefits the overall application of density distribution model obtained.

Chapter 6

Finite Element Modeling

6.1 Introduction

This chapter outlines the development of a Finite Element (FE) model to simulate the powder compaction process. The FE results are compared with the experimental measurements to evaluate the validity of the FE technique for the determination of the density distribution of compacted specimens. This chapter also describes the material model, mesh generation, mesh sensitivity analysis and the application of the boundary and loading conditions. Finally, the validity and accuracy of FE results are discussed.

6.2 Computer Modeling

To model the compaction process a geometric model of die, punch and powder compact was required. A surface model of the die and punch was first developed. This matched the size of the test specimens used in this study. The surface model was used to generate a three dimensional solid model of the components, as shown in Figure 6-1. The surface model of the powder compact was also used to develop a three dimensional model which was subsequently discretized by meshing (Figure 6-2). The two sets of models were then merged into one assembly model containing the die, punch and the powder. The punch and die were not discretized since they are much more rigid than powder and will be considered as rigid bodies. Process of discretization and meshing is one of the most important parts of FE simulation as the mesh size

65

has direct affect on the final simulation results. The mesh sensitivity analysis is the process by which the discrete element size is chosen such that the dependency of the results on mesh size is eliminated. In this study, at first a coarse mesh was used to simulate the powder compaction. The result of the analysis was compared with the experimental measurement. Subsequently, the mesh was refined and analysis was repeated until the effect of mesh refinement on the final results reduced to a negligible improvement. The sensitivity analysis was performed on 10mm thickness size at 276 MPa of pressure. Table 6-1 summarizes the mesh sensitivity analysis. Please note that the mesh sensitivity analysis was only carried out on one of the simulation. Once the optimum size was determined, the mesh size was consistently used in all other FE analyses.

Table 6 - 1: Mesh size and FE

Element axis	Mesh Size [mm]			Relative Density
	X axis	Y axis	Z axis	
Analysis 1	4.4	4	1.6	5.01
Analysis 2	2.2	4	1.6	5.16
Analysis 3	2.2	2	1.6	5.31
Analysis 4	1.1	1	0.8	5.42
*Analysis 5	0.9	0.9	0.8	5.469
Analysis 6	0.55	0.5	0.8	5.462

As mentioned previously, the base cross sectional area of the samples are identical. To obtain 10, 15 or 20 mm sample size after compaction requires different starting volume of tapped powder. With identical cross sectional area, the height of the tapped powder must increase as the compacted sample thickness increases, Table 6-2.

Table 6 - 2: Sample thickness

Final Sample size	Compaction Pressure				
	276 MPa	372 MPa	462 MPa	565 MPa	662 MPa
10 mm thick	16	17	17.6	18.3	19
15 mm thick	24	25.4	26.5	27.4	28.2
20 mm thick	32	34	35.1	36.6	37.8

Because of the rectangular cross sectional area of the specimen, the effect of friction varies along each in-plane axis. Moreover, the sharp corners of the rectangular cross section cause friction effect to vary along each in-plane axis. Therefore, a three dimensional model has to be constructed to fully capture the realistic compaction process [57]. To simplify the simulation without compromising the accuracy of the result, only quarter of the specimen was modeled using two plane of symmetry at the center of specimen.
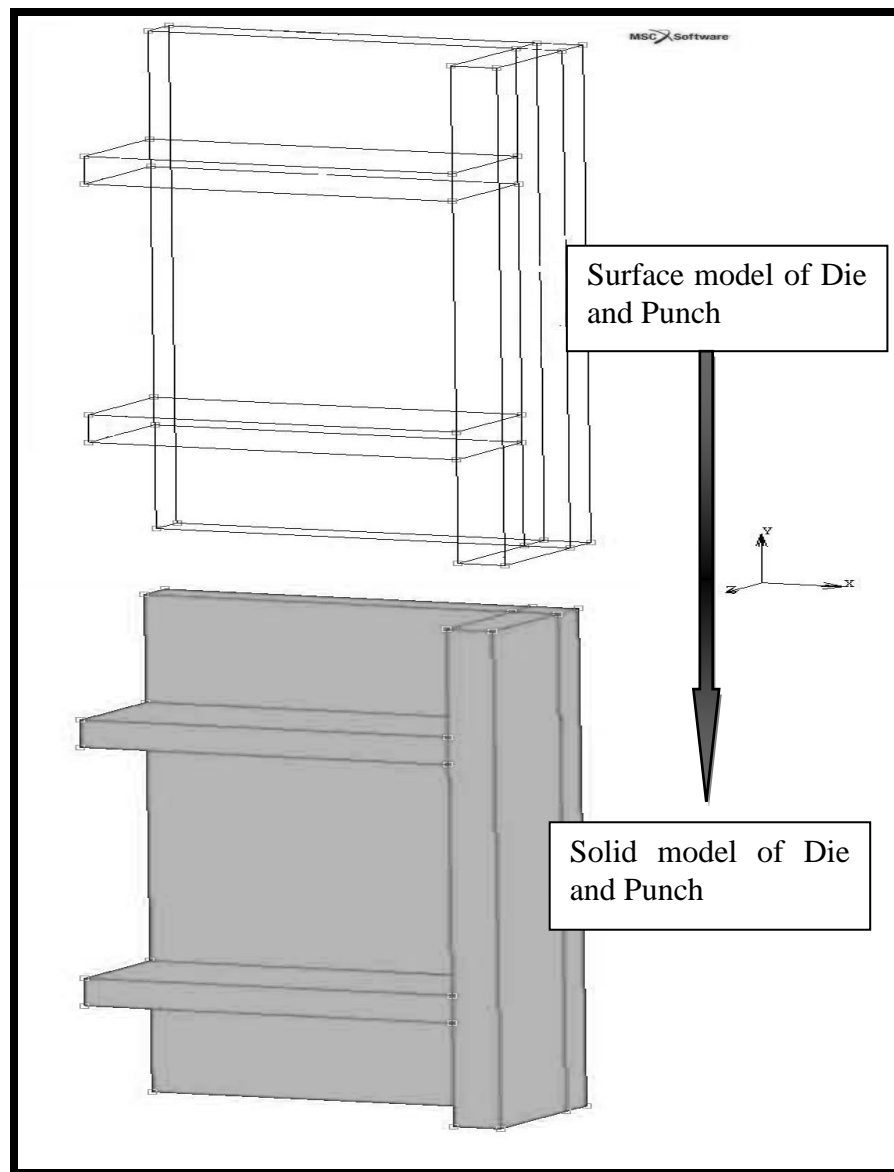
Figure 6 - 1: Finite Element model of Die from surface to solid model
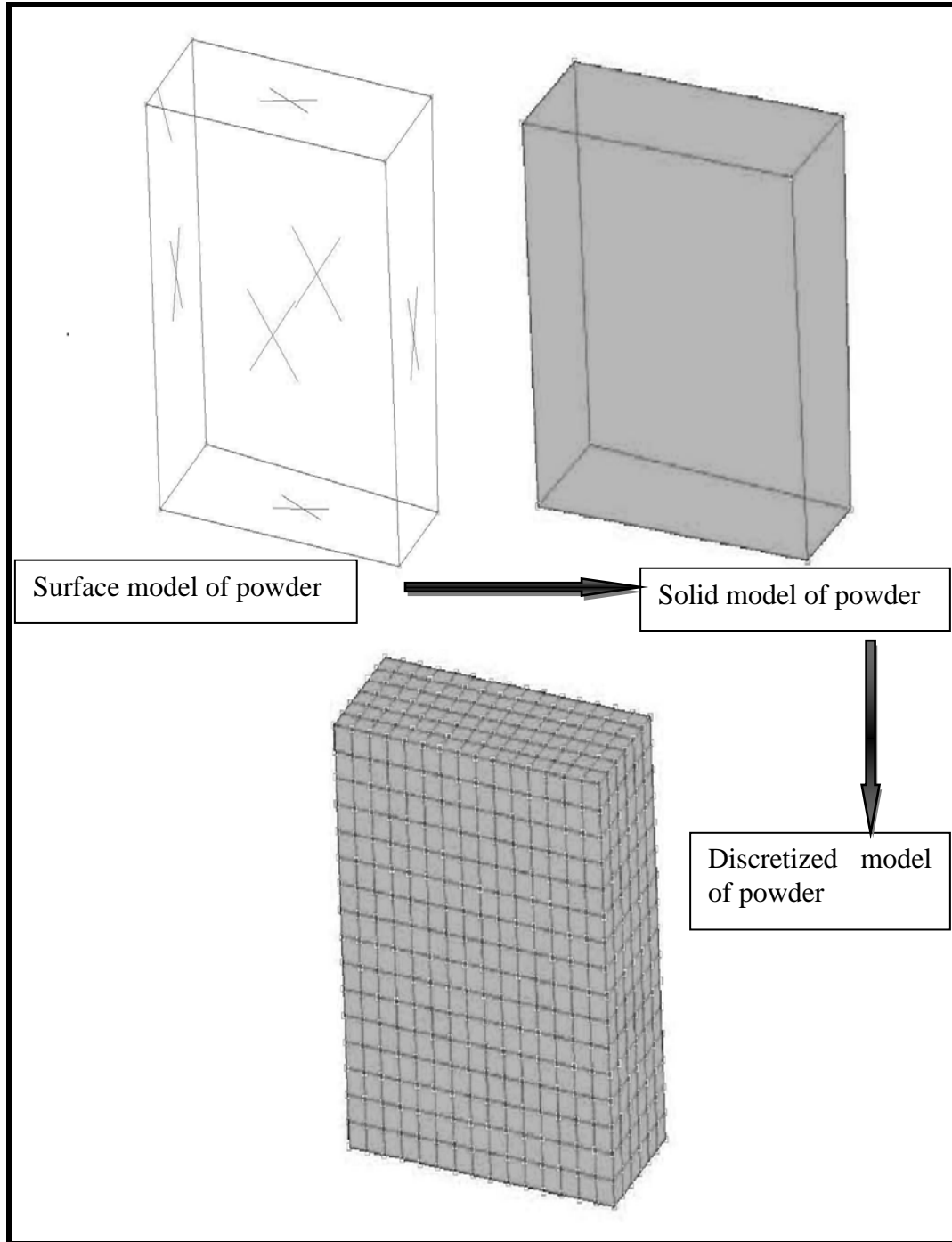
Figure 6 - 2: Finite Element model of powder from surface to discretized model
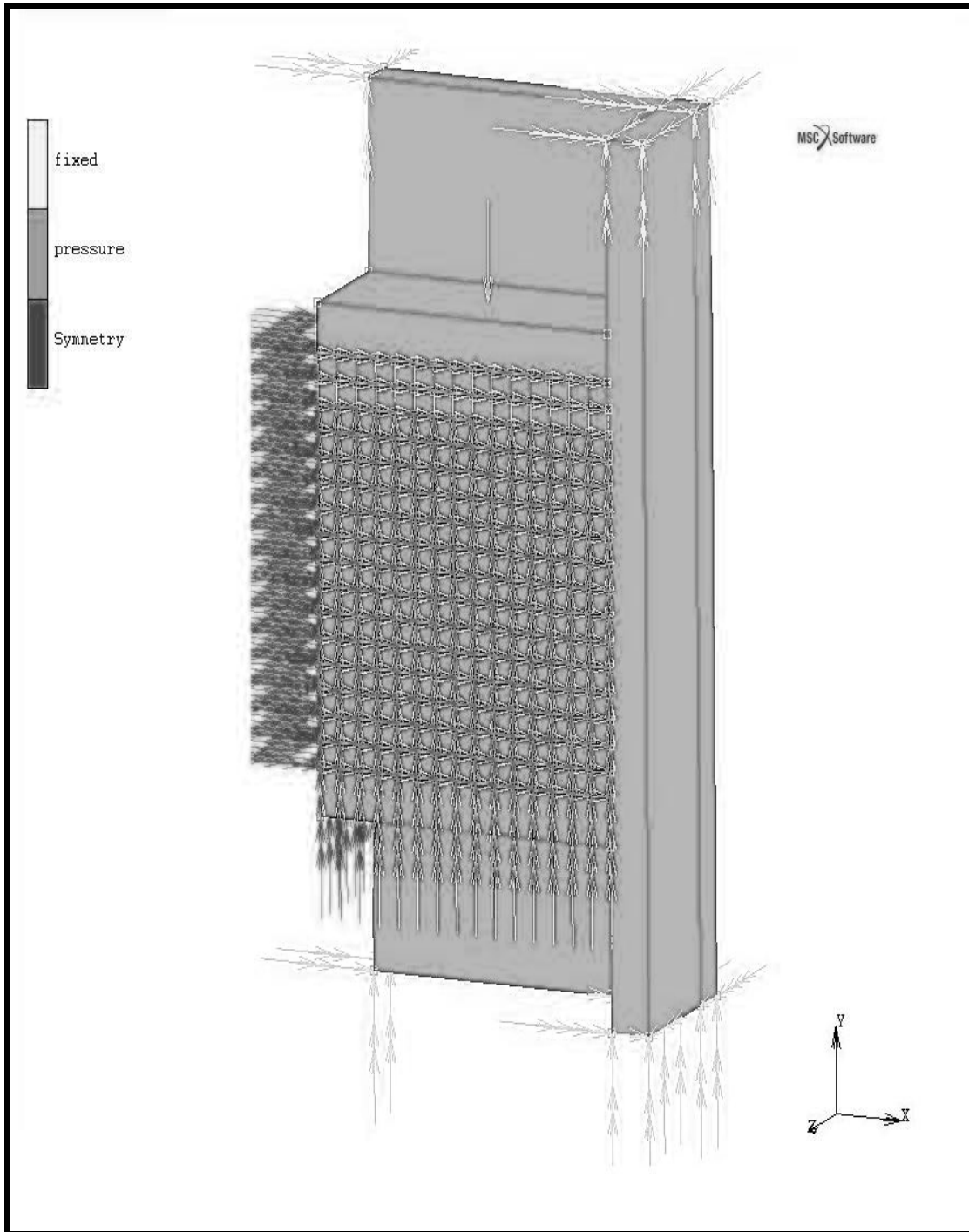
Figure 6 - 3: Finite Element models of Die and powder with applied boundary conditions.
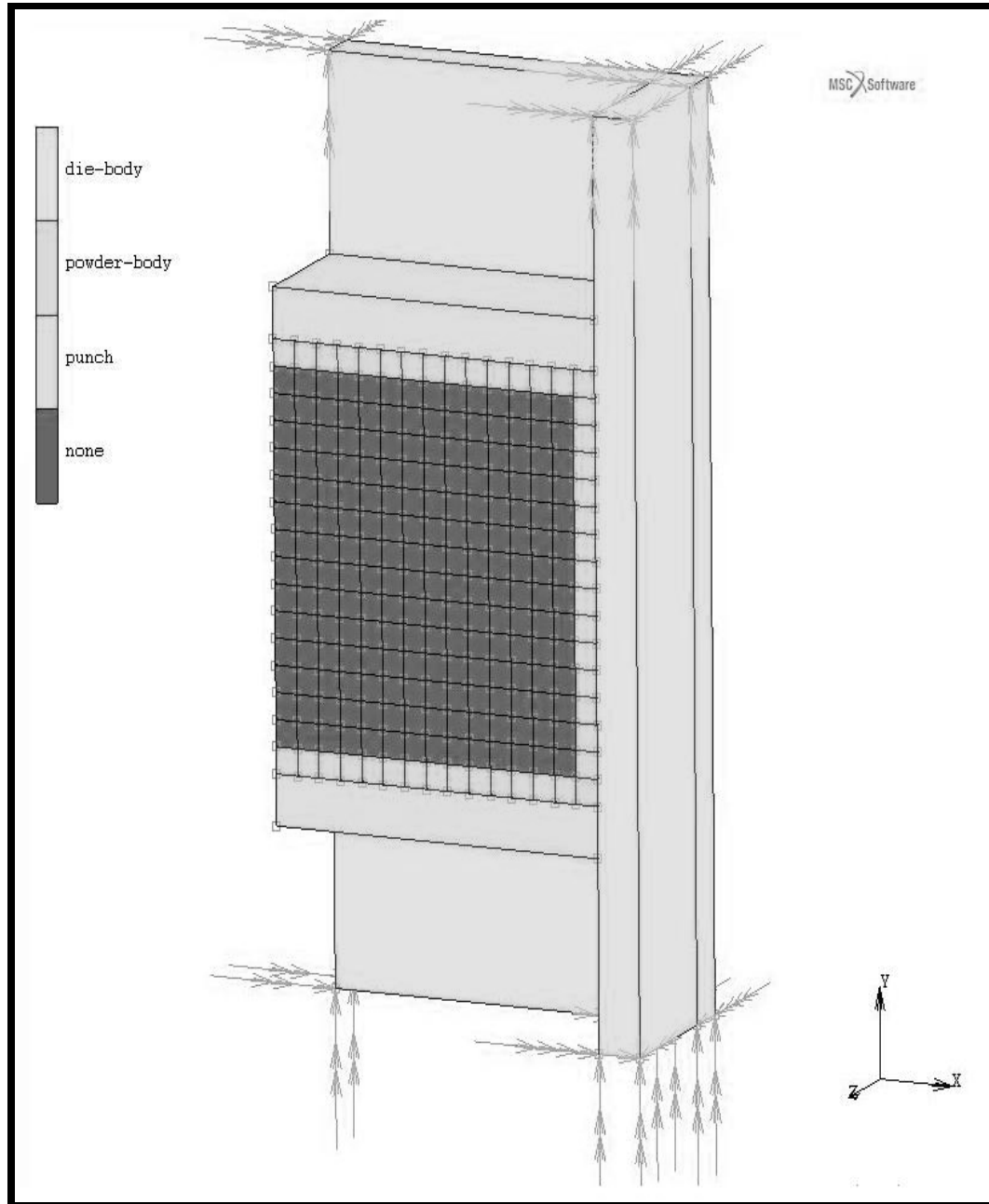
Figure 6 - 4: Contact area of Finite Element model of Die and powder.

6.3. Boundary Conditions

Appropriate boundary conditions are necessary for accurate modeling of the compaction process. In practice, pressure is applied on the powder while the die is stationary. The boundary condition must simulate the same conditions in the FE model. A pressure equal to the one used

during sample preparation was applied to the top and bottom surfaces of the powder model. Since the die is stationary, all nodal movements of the die were constrained in all direction. Additionally, since only one quarter of the specimen was modeled, a symmetric boundary condition was applied to the free surfaces of the powder model. This was achieved by constraining the motion of the nodes on the surface of the symmetric plane. The symmetry assumption is based on the fact that the center plane (the center of the specimen) remains central after the application of the load. Figure 6-3 shows the complete model with boundary conditions.

As it can be seen from Figure 6-3, the die movement is fixed in all directions. Furthermore, the pressure is applied directly to the punch and the symmetric boundary condition is applied to the two free faces. The symmetric boundary condition has constrained the x-direction and z-direction movement of the powder and allows the y-direction movement to reflect the deformation under the applied pressure. In this case, the symmetric plane will not experience any out-off-plane deformation and only in place compressive deformation will result under the pressure loading. The die constrains and symmetric plane boundary conditions were common amongst all the models simulated. However, the applied pressure load was changed to reflect the various compaction pressure used in the fabrication of the experimental samples.

It is known that a frictional force will be generated on the specimen during the fabrication phase. In order to perform an accurate simulation, in addition to boundary condition, an appropriate modeling of friction was necessary. To consider the frictional forces between the die and powder, both bodies were defined as deformable. Under the deformable condition, a Coulomb friction contact was chosen with the condition of slip to stick [58]. The slip to stick condition can be viewed as the tolerance on the relative displacement between the nodes of

contacting bodies. There are three parts to this contact; first elements that make up the bodies, the nodes on the contacting surface and finally the faces that describe the outer surface of contacting elements. The Coulomb friction model with slip to stick transition can be described as relation between tangential friction stresses (force) to normal friction stress (force). Mathematically, the following relation defines the slip to stick condition:

$$\|\sigma_t\| \angle \mu\sigma_n \qquad\qquad \text{Stick} \qquad\qquad\qquad (1)$$

$$\|\sigma_t\| = -\mu\sigma_n.t \qquad\qquad \text{Slip} \qquad\qquad\qquad (2)$$

where, σ_t is tangential stress

σ_n is normal stress

μ is coefficient of friction

t is the tangential vector in the direction of the relative velocity

There are several parameters such as friction multiplier, friction force tolerance, single or double sided contact and coefficient of friction that need consideration. These were all kept at program default values except for the coefficient of friction. A detailed explanation of each parameter can be found in the theory manual of MAS Marc software [57]. The coefficient of friction was considered constant throughout the simulation and its value was considered to be 0.15 [59 and 60]. In reality, the coefficient of friction changes as densification takes place under compacting pressure. However, MSC MARC does not allow the friction coefficient as the function of the relative density [57]. Figure 6-4 depicts the model with contact surfaces.

6.3.1 Material Constitutive Model

A number of approaches have been developed for modeling the behaviour of powder compacts. Generally most of these models have described the behaviour of powder material

based on a single state variable, the relative density. Early empirical models assumed a yield surface of the Green/Shima type (Shiam and Oyane 1979) [43]. Shima model is a quadratic function of the von Mises effective and mean stress that was derived originally from copper powder [43]. In this case, the material state is described in terms of the porosity, or relative density. The functional dependence of the yield condition on the material state is generally determined by conducting experiments on sintered components compacted to different densities. Such models predict the same yield stress in the uniaxial tension and compression. Powder material model in MSC MARC is a function of temperature and densification [58]. The yielding function used is the Shima-Oyane model for powder materials. The MSC MARC uses a unified viscoplastic approach with the following yield function [58]:

$$F = \frac{1}{\gamma}\left(\frac{3}{2}\sigma^d\sigma^d + \frac{P^2}{\beta^2}\right)^{\!\!1/2} - \sigma_y \tag{3}$$

where σ_y : uniaxial yield stress

σ_d : deviatoric stress

P : hydrostatic pressure

γ and β : material parameter

ρ: the relative density

Typically γ and β are function of the relative density. The following formulation is the typical scheme used to calculated γ and β.

$$\gamma = \left(q_1 + q_2\rho^{q_3}\right)^{q_4} \tag{4}$$

$$\beta = \left(b_1 + b_2\rho^{b_3}\right)^{b_4} \tag{5}$$

The parameters used to determine γ and β are as follows [59 and 60]:

$b_1 = 5.8995087$	$b_2 = -5.8995087$	$b_3 = 1$	$b_4 = -0.514$	(6)
$q_1 = 0$	$q_2 = 1$	$q_3 = 1$	$q_4 = 2.5$	(7)

Note as the powder becomes denser, the relative density approaches unity (fully dense) and the Shima yielding model approaches the classical von Mises yielding criterion. MARC allows the material properties to be a function of the relative density, as well. In particular, at fully dense condition, the Poisson's ratio approaches 0.5. In this analysis, the Young's modulus was also defined as a function of relative density. The material model used here was defined by Pavier and Doremus (1999) [60 and 61].

$$E = \left(-2800 + (10020 \times 7.99)\rho\right)e^{\left(\frac{7.99}{6.8}\right)^6} \tag{8}$$

$$\nu = 0.5 - \left[\left(-2800 + (10020 \times 7.99)\rho\right)e^{\left(\frac{7.99}{6.8}\right)^6} \Big/ \left(6 \times (-10500 + 3750\rho 7.99)\right)e^{\left(\frac{7.99}{6.55}\right)^6}\right] \tag{9}$$

Yield stress was $\sigma_y = 370$ MPa and the shear viscosity was 2 MPa.

The Material Properties presented in Equations 2 to 5 were used in the FE model of compaction process. The initial relative density used in this analysis was 0.435 which was provided by the manufacturer of the specimen. This value is calculated as the ratio between the tap density and the full density of stainless steel.

6.4 Finite Element Results

Fifteen FE models were developed that represented the tapped (uncompressed) powder model for all samples. These models were constructed based on the sample dimensions with common cross sectional area. In other words, the cross sectional areas were identical and the thickness of the model differs from sample to sample. Table 3-1 in Chapter 3 identified the cross sectional area, uncompressed powder weight, mass density and overall thickness of each sample after compaction. This information coupled with the tapped density was used in determining each sample's dimensions. Figures 6-5 to 6-7 depict the contour plot of relative density

distribution of 10 mm thick sample fabricated under 276 MPa of compaction pressure. Figure 6-5 shows that the average relative density came out to be 0.69, which translates to 5.469 g/cm^2 average density considering 7.99 g/cm^2 full density of 316L stainless steel.

Figures 6-6 and 6-7 indicate the density distribution on the surface that is in contact with die body and punch of the same specimen. Figure 6-6 and 6-7 show an incompatible density distribution to that of free surface. This is due to the frictional forces that are generated between the powder and the die-punch body during compaction phase. The contour plot in Figure 6-5 shows that the density distribution is a maximum on the free edge on the top and bottom surfaces (similar compaction pressure act on both surfaces). In reality, the center of specimen at the free surface should have the highest density as compared to any other location on the specimen. This trend was observed in experimental phase of this study.

Figures 6-8 and 6-9 depict the simulation results for fabrication of 10 mm thick samples at 469 MPa and 662 MPa compaction pressure, respectively. These results are presented to indicate the validity and accuracy of the FE simulation. These contour plots show that the FE modeling can predict the average relative density of the specimens to within 3.0% deviation from the experimental measurements.
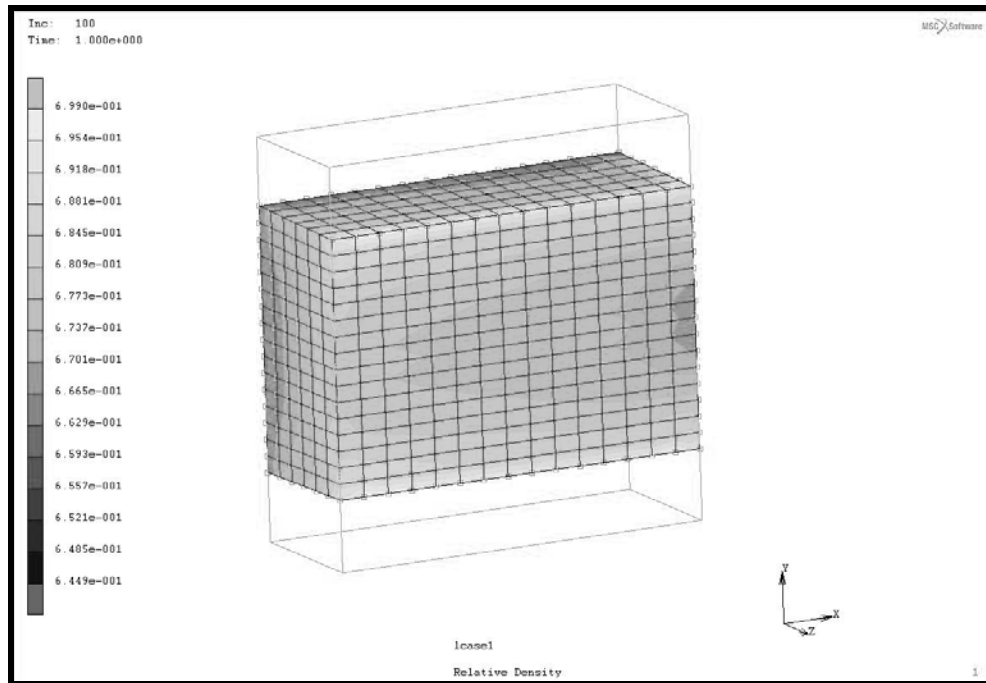
Figure 6 - 5: Density distribution of specimen compacted under 276 MPa pressure. This contour plot shows the center surface (face that is not in contact with die body).
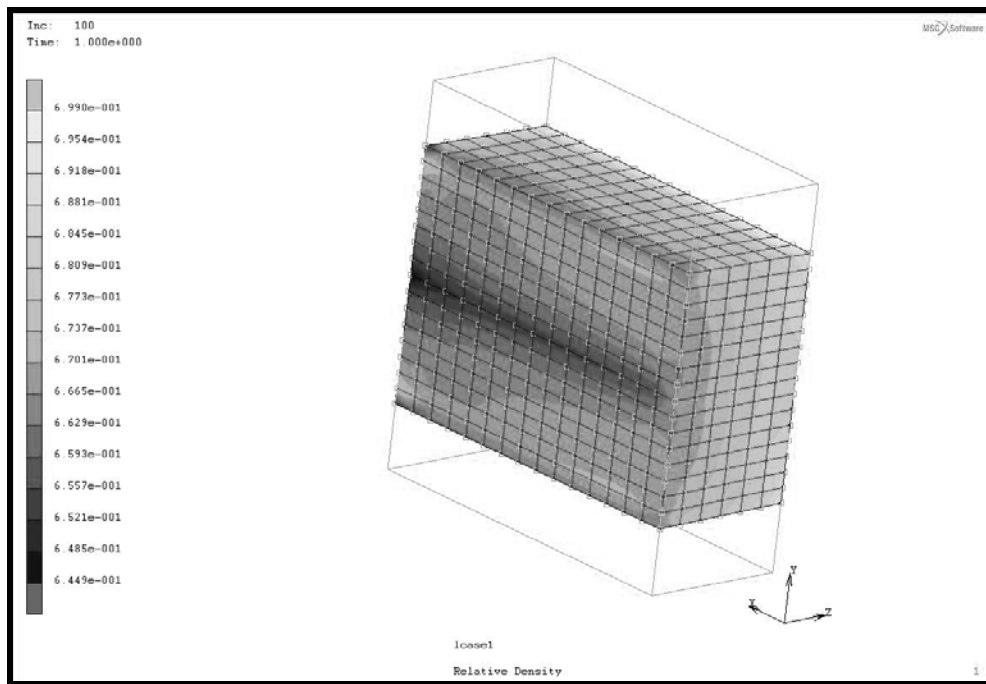

Figure 6 - 6: Density distribution of specimen compacted under 276 MPa pressure. This contour plot shows back surface (face that is in contact with die body).
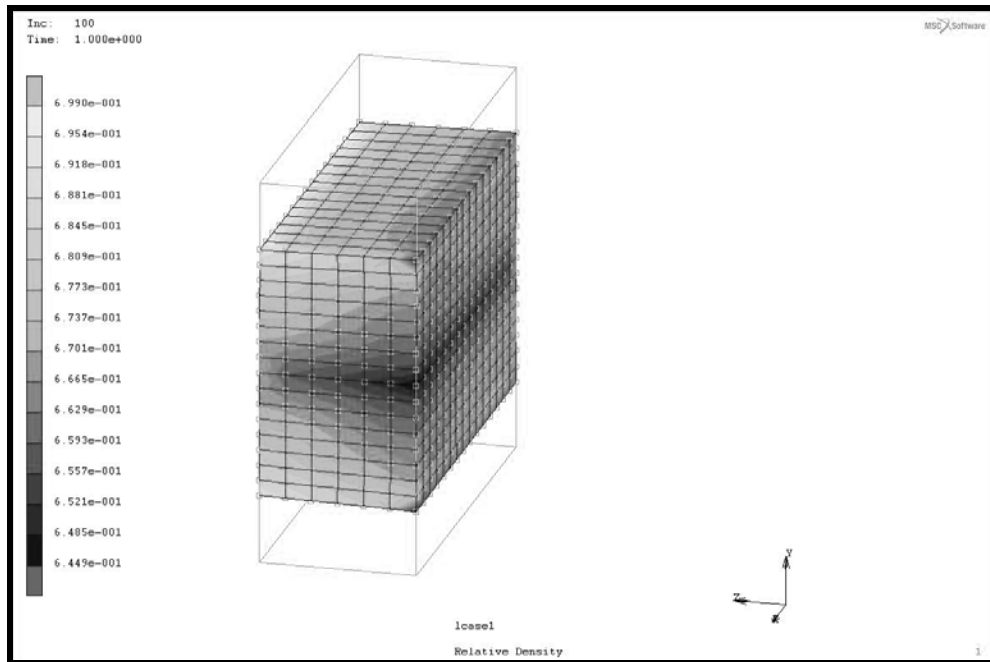
Figure 6 - 7: Density distribution of specimen compacted under 276 MPa pressure. This contour plot shows the center (face that is not in contact with die body).
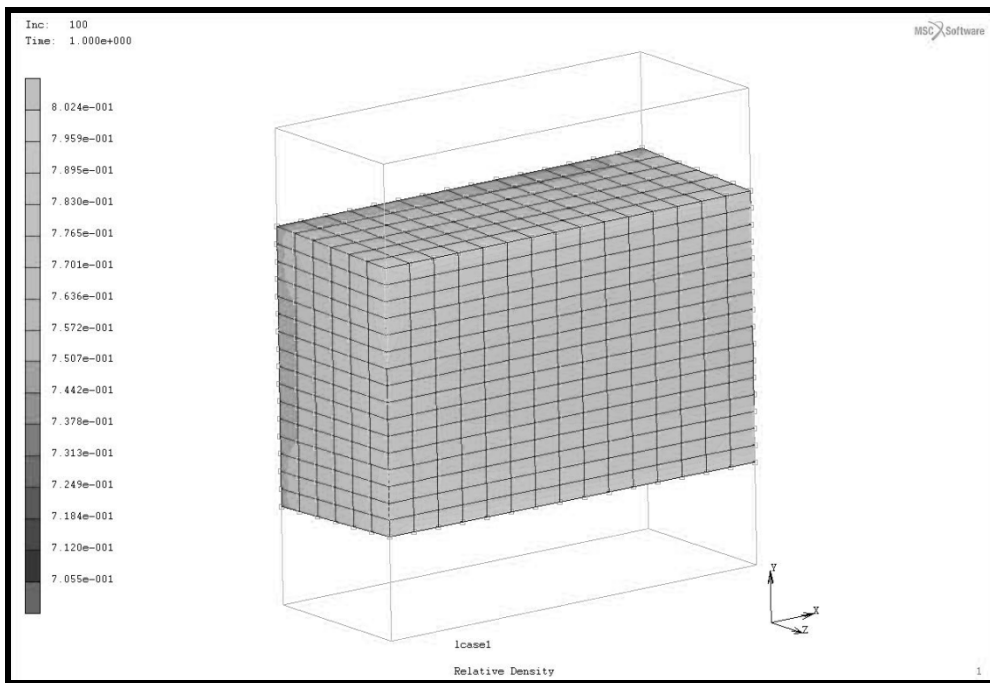

Figure 6 - 8: Density distribution of specimen compacted under 469 MPa pressure. This contour plot shows the center surface (face that is not in contact with die body).
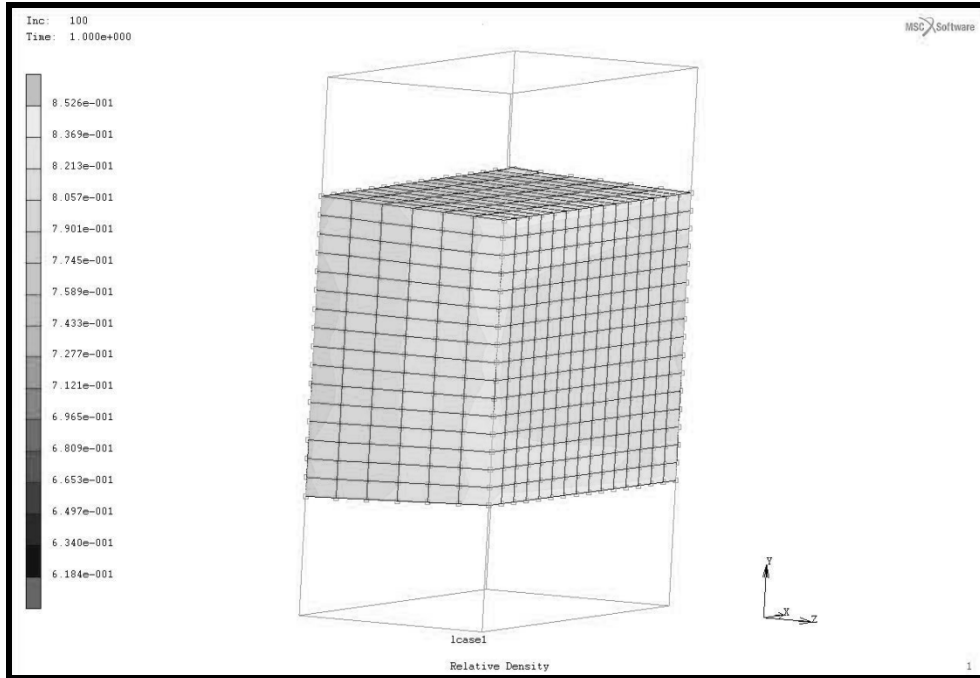
Figure 6 - 9: Density distribution of specimen compacted under 662 MPa pressure. This contour plot shows the center surface (face that is not in contact with die body).

In powder compaction, after the die filling stage, a vibratory or tapping stage follows. The main purpose of this action is to obtain a uniform tapped density throughout the un-compacted specimen. During tapping stage, few larger particles may come in contact with each other and form a bridge. A bridge, by definition, is the formation of void as the result of stacking of larger powder particles. As mentioned before, the experimental specimens used in this study were fabricated from irregular grain shapes of 100 mesh size (less than 150 micrometer grain size). In other words, the powder used here contains grain size of 150 micrometer and smaller.

Due to aforementioned tapping process and grain size, the tapped density may be non-uniformly distributed throughout the sample. The inhomogeneous distribution of void throughout the specimen causes an inhomogeneous density distribution in an un-sintered compacted specimen. The inhomogeneous density distribution was observed experimentally. On the other hand, the finite element method works based on the continuous distribution of relative density in

the element. This means that each discrete element in the model has the same tapped density at the start of the solution. In the absence of an external influence, the resulting density distribution of the FE simulation would be constant throughout the sample. In fact, a sample simulation was carried out on powder alone and the resulting density distribution was determined to be constant. Figure 6.10 shows that density is constant throughout the model signifying the continuous distribution of starting relative density.
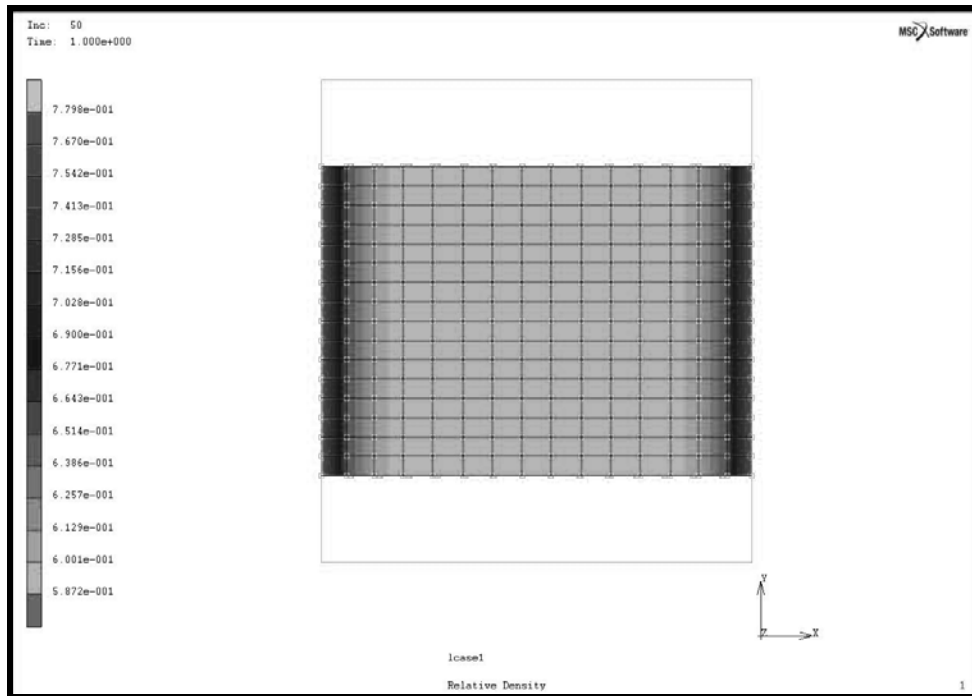

Figure 6 - 10: Constant density distribution of specimen compacted at 276 MPa pressure. Without the punch and die body effect

In the cases studied here, because of the punch and die body frictional influence, the density distribution is inhomogeneous near and around the contacting area of the powder and vanishes everywhere else. The resulting homogeneous density distribution becomes more dominant as the compaction pressure increases. As can be seen from Figures 6-5, 6-8 and 6-9, the higher the pressure, the larger the area of constant relative density.

Due to the nature of the FE formulation, the model here does not estimate the local density. Thus, the FE results will not be appropriate for evaluating the local density distribution. Nonetheless, the FE results are excellent indicator of the average overall density. Table 6.3 lists the results of the FE simulation and the experimental results. Moreover, Figures 6-11 to 6-13 depict the comparison of overall density between experimental and finite element results for samples 10, 15 and 20 [mm] respectively.

Table 6 - 3: Summary of FE and experimental result

| Pressure	10 mm			15 mm			20 mm		
	FE	EXP	% error	FE	EXP	% error	FE	EXP	% error
276	5.469	5.58	1.9	5.462	5.57	1.9	5.480	5.56	1.4
372	5.895	5.93	0.5	5.840	5.9	1.0	5.860	5.9	0.7
469	6.134	6.12	0.2	6.137	6.09	0.8	6.170	6.1	1.2
565	6.438	6.35	1.4	6.441	6.35	1.4	6.168	6.36	3.0
662	6.488	6.54	0.8	6.572	6.55	0.3	6.480	6.57	1.4
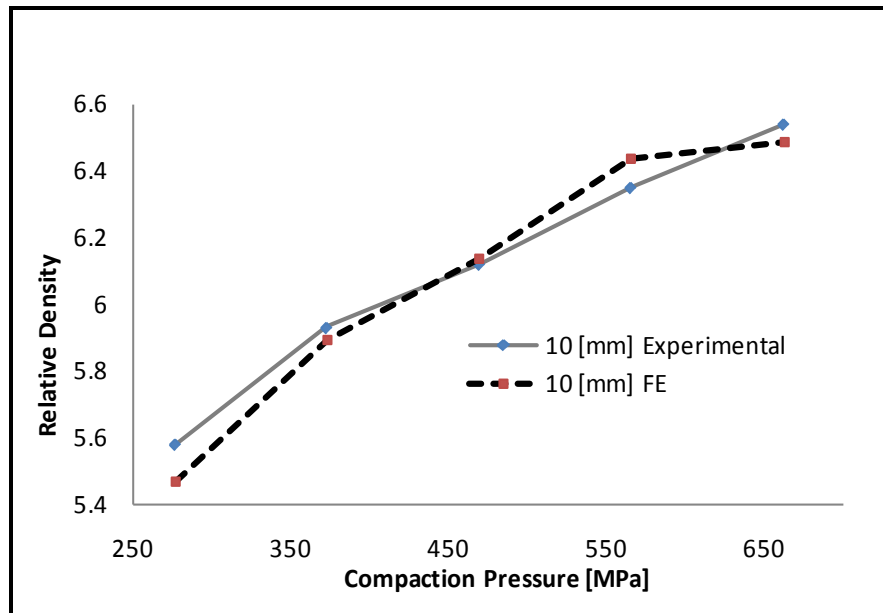
Figure 6 - 11: Comparison between experimental and finite element results for 10 mm specimen
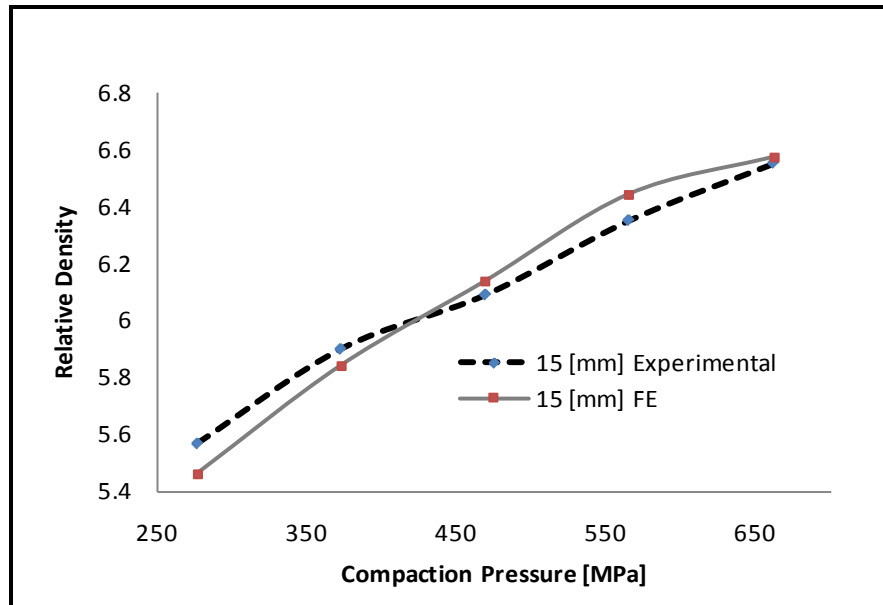
Figure 6 - 12: Comparison between experimental and finite element results for 15 mm specimen
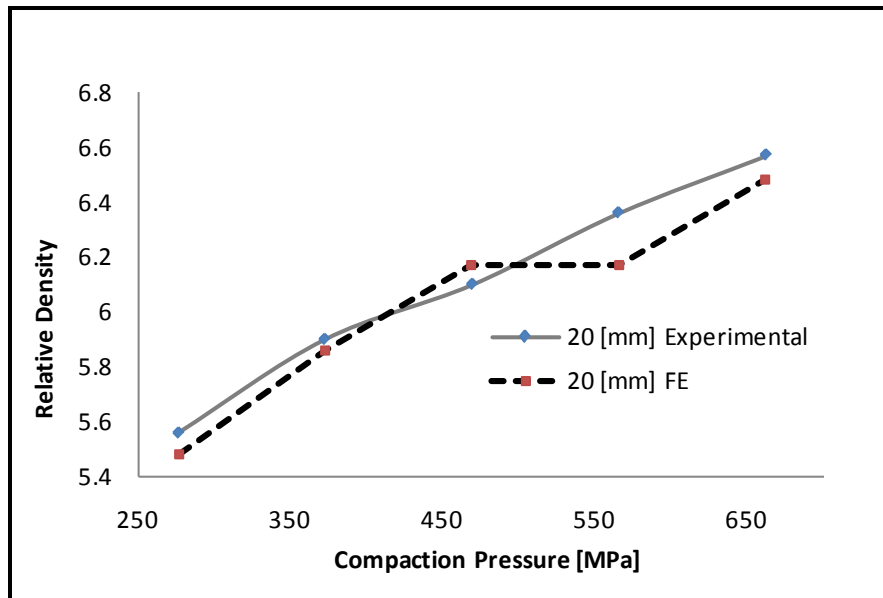

Figure 6 - 13: Comparison between experimental and finite element results for 20 mm specimen

6.5 Conclusions

Fifteen FE models of experimental specimens were constructed. FE simulation of powder compaction of the specimens was performed and the results compared with experimental data. It was determined that since the FE formulation is based on a uniform distribution of the relative

81

density, the determination of the local density is not achievable. One possible way of determining the local density is to assign various state parameters to each element of the model, such as Young's modulus, Poisson ratio and starting relative density. This can be achieved by creating an input program. More importantly, the accuracy of such simulation directly relies on the accurate knowledge of the starting local density or void ratio of the experimental samples.

Nonetheless, the FE results show an excellent agreement with the average relative density obtained from the experimental work. The FE results indicate that the FE method is a reliable and accurate method for overall density calculation.

Chapter 7

Conclusion

7.1 Conclusion

The focus of this research was to study and determine the green density of powder material at various compaction pressures. Green shape (density) is defined as the state of the powder in which the powder is compacted under high pressure. In green state, powders are bonded together either by grain interlocking or by cold welding. In general, cold welding occurs at high compaction pressure and powder interlocking happens at low compaction pressure. To measure the relative green density of specimens, scanning electron microscope (SEM) with 300 X magnification was utilized. Specimens fabricated at low compaction pressure showed that interlocking at the grain interlocking was visible. On the other hand, at high compaction pressure, the boundary of powder grains was not visible indicating cold welding phenomenon.

The behaviour of the cold compaction process of iron powders depends on material response such as friction between powders, tool kinematic, lubrication, compaction process, the particles experience frictional forces between each other and die and punch boundary. The experimental results showed that the center of specimen achieved higher density than other areas on the sample during compaction. This phenomenon could partly be attributed to the fact that smaller particles migrate at the center of specimen during vibratory or tapping process. This makes the tapped density at the center of specimen to appear denser. Another reason for denser central region is the fact that frictional forces vanish at the center of specimen. These two factors

combined are the main reason for denser central region. This fact was observed in all samples tested here regardless of compaction pressure.

Upon experimental evaluation of green density, neural network method was used to estimate the green density. The neural network modeling was used as a technique to reproduce green density variations during compaction process. In other words, a neural network was used to predict the green density distribution in any desired location. Intuitively, one can see the direct relationship between pressure and green density, as pressure increases so is the green density. The direct relation between pressure and green density accurately was predicted with ANN.

It was determined that the ANN results were closer to experimental at sub layers than top layers in all sample. Upon close inspection of input data, it was determined that the experimental data for top surface had wider range than the experimental data on sub surface layers. For instance, the data at the die body on top surface of specimen was measured 4.23 g/cm^3 and at the center of specimen were measured 5.38 g/cm^3. On the other hand, the middle layer reading at the die body was 5.71 g/cm^3 and 5.95 g/cm^3 at the center of the specimen for the same compaction pressure. This indicates that ANN training data were sparser on top surface than the middle layer. As mentioned earlier, equal amount of data from all surfaces were used in training ANN. Therefore, the results of ANN modeling would be closer to the experimental on sub surface layers than the top surface layer. Nonetheless, ANN demonstrated that it can predict the green density of powder component with excellent accuracy.

In addition to neural network, the application of finite element method was also studied. Finite element has application in variety of field such as automotive, aerospace, biomechanics as well as machining and manufacturing. One of the goals of this study was to determine the validity and application of FE in powder metallurgy. Here, fifteen finite element models

corresponding to the experimental specimens were constructed and compaction simulations were carried out. Finite element formulation is based on a continuous distribution of the relative density. As such, each discrete element in FE model had the same mechanical properties such as Young's modulus, Poisson ratio and starting relative density. As such, in the absence of external influences such as die friction, the FE results showed a uniform distribution of relative density. Thus, the determination of the local density was not achievable with model used in this study.

In order to accurately determine the local density at any desired location (density distribution), state parameters such as relative density could be applied individually to each discrete element. This can be achieved by creating an input program as a user subroutine. However, it is extremely important to note that the accuracy of such simulation directly relies on the accurate knowledge of the starting local density or void ratio distribution of the experimental samples, which is extremely difficult to measure if not impossible. Nevertheless, the FE results predicted the overall relative density with excellent agreement to the experimental measurement. The FE results indicate that the FE method predicted the average relative density to within 2% deviation from experimental average relative density. The FE results clearly demonstrate the reliability and accuracy of FE method in powder metallurgy.

7.2 Contribution

In this study, the density distribution as a function of compaction pressure was investigated. A comprehensive study was carried out experimentally to measure the green density distribution at various locations and various depths of specimens. Many valuable researches has been performed in this area. However, to the best of author's knowledge, the density distribution at green state under various compaction pressures has not been addressed.

Thus, the main contribution of this work is the determination of density distribution of powder compacted specimens in green state. Additionally, the role of tapping in general is also highlighted though out the work presented here.

7.3 Future work

This work can be expanded to cover few areas. The most important expansion is to performed study on the green state - compaction pressure relationship for more geometrically intricate specimens. Another important area is the fracture toughness of un-sintered compacted components. More geometrically intricate parts have tendency to fracture either when parts is ejected from the die or during handling prior to heat treatment. Further work could be performed on quantify the relation between green density and sintered density.

Appendix

Experimental Results
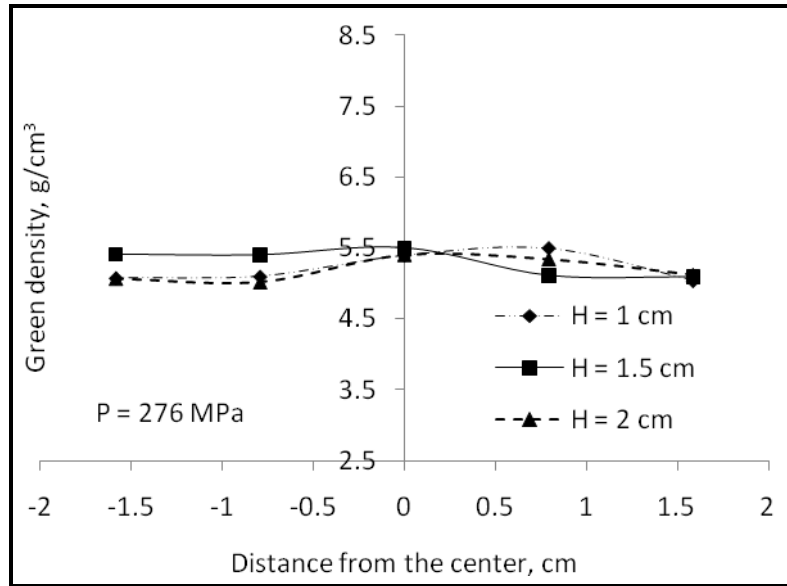
Figure A - 1: Density distribution of first layer at 276 MPa for all samples
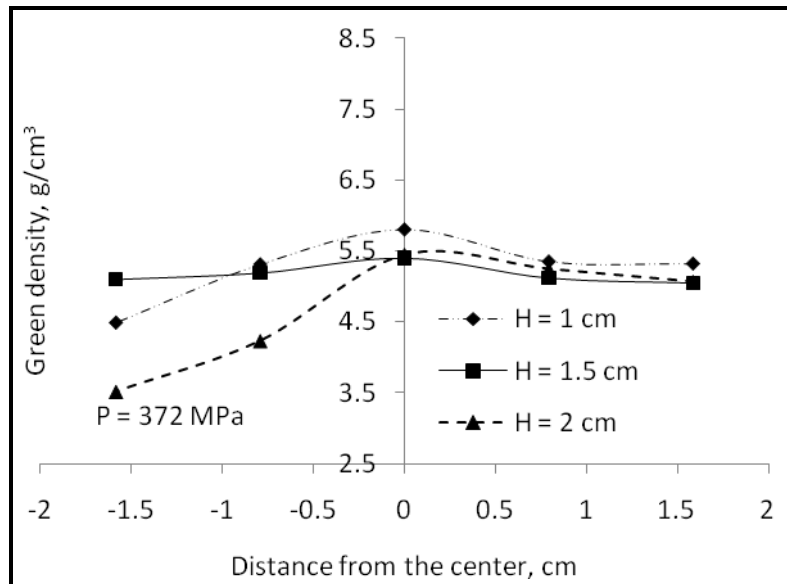
Figure A - 2: Density distribution of first layer at 372 MPa for all samples

87
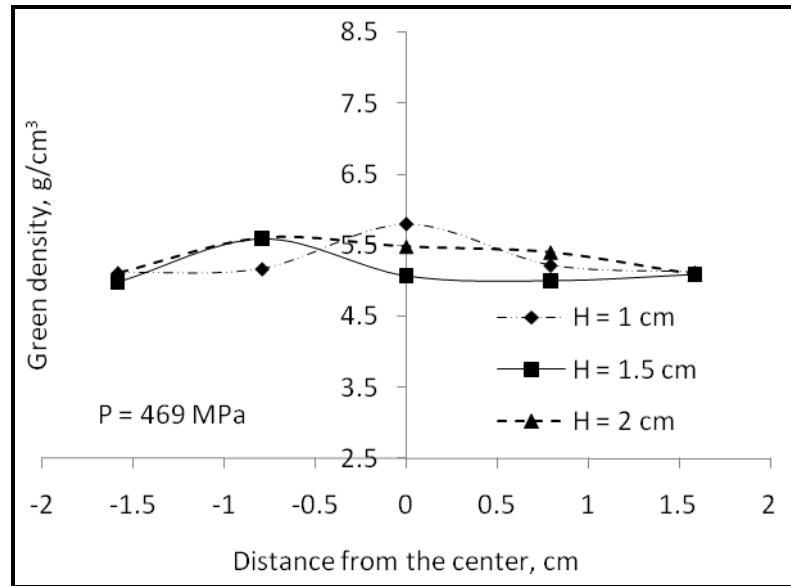
Figure A - 3: Density distribution of first layer at 469 MPa for all samples
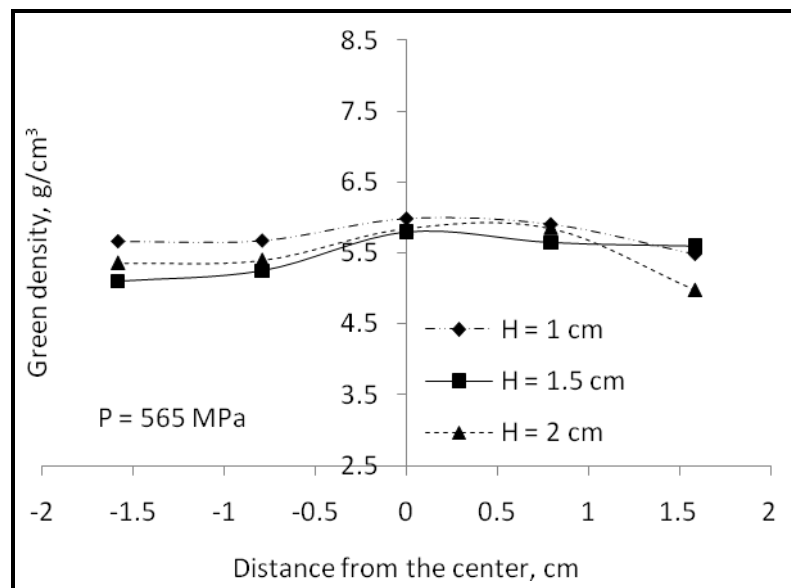
Figure A - 4: Density distribution of first layer at 565 MPa for all samples
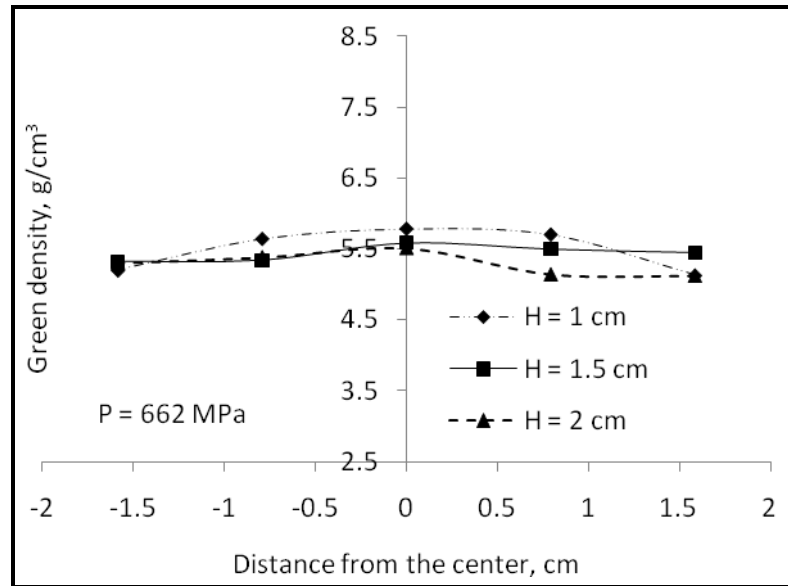
Figure A - 5: Density distribution of first layer at 662 MPa for all samples
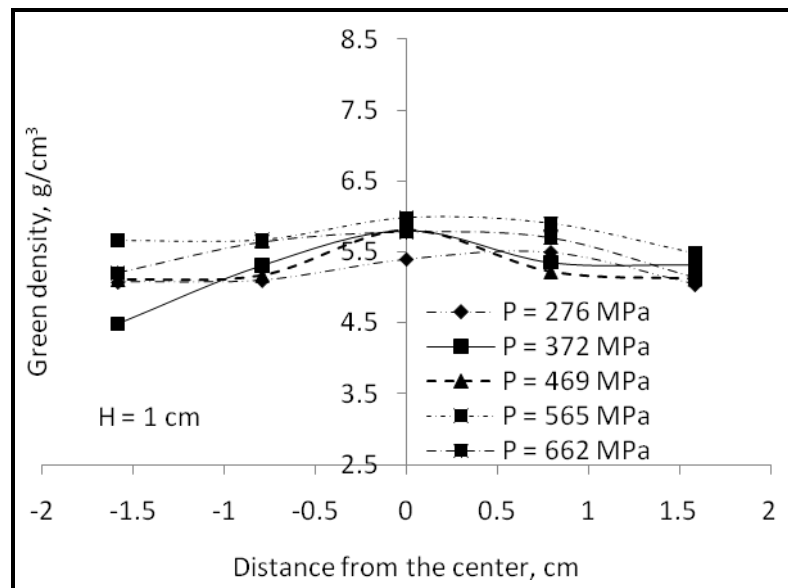
Figure A - 6: Density distribution of first layer for 1.0 cm thick sample
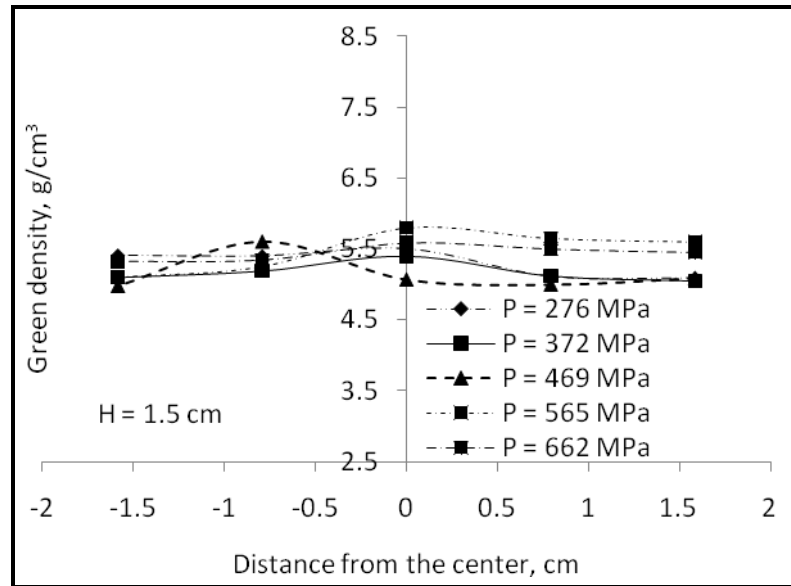
Figure A - 7: Density distribution of first layer for 1.5 cm thick sample
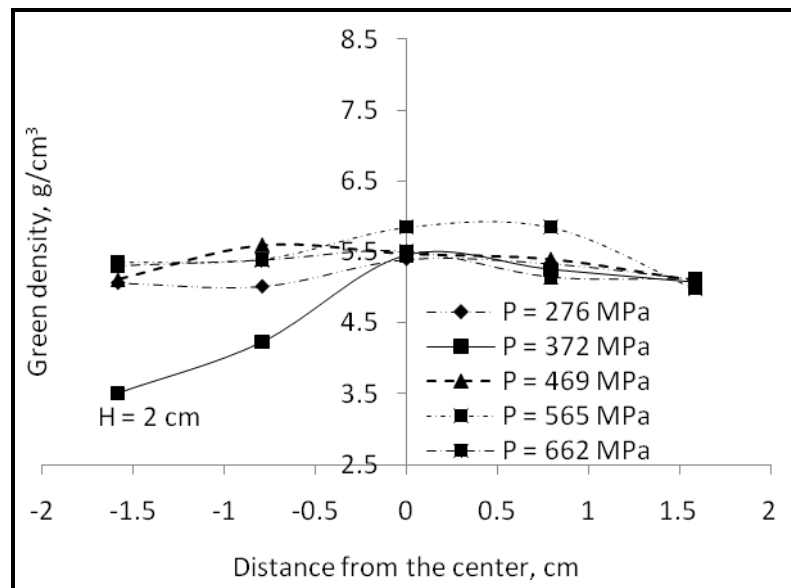
Figure A - 8: Density distribution of first layer for 2.0 cm thick sample
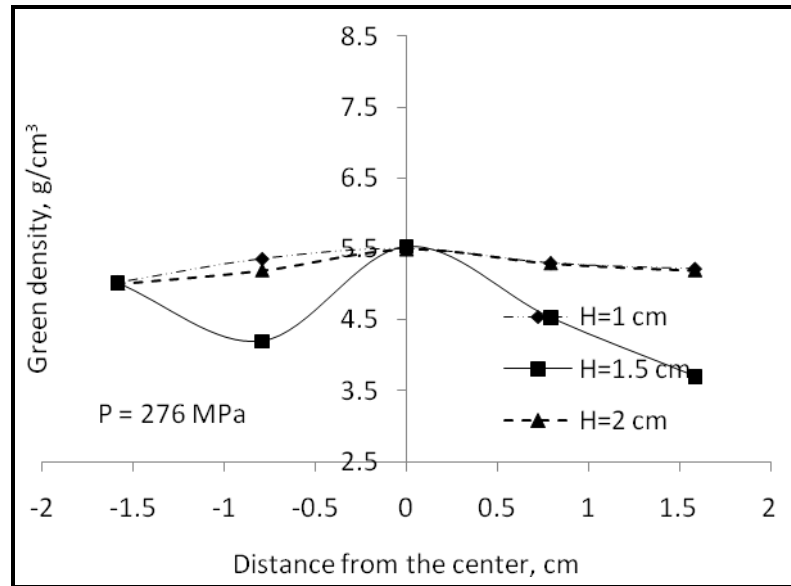
Figure A - 9: Density distribution of second layer at 276 MPa for all samples
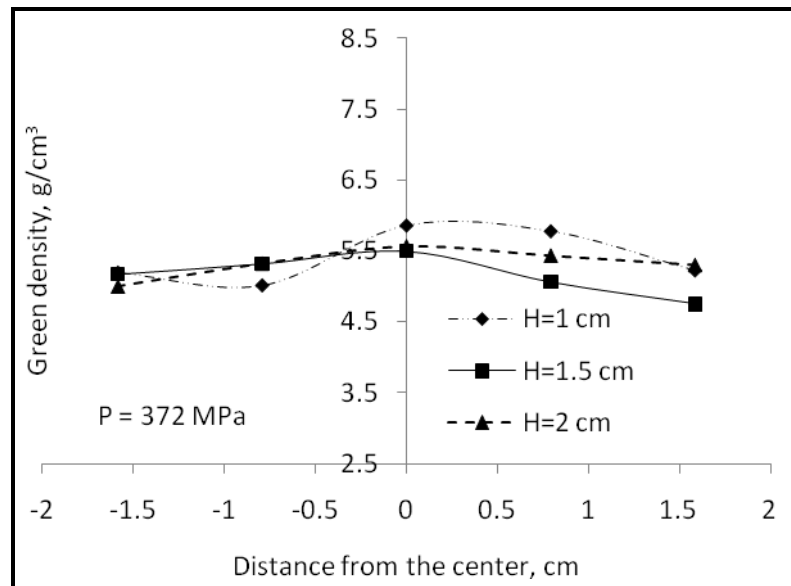
Figure A - 10: Density distribution of second layer at 372 MPa for all samples
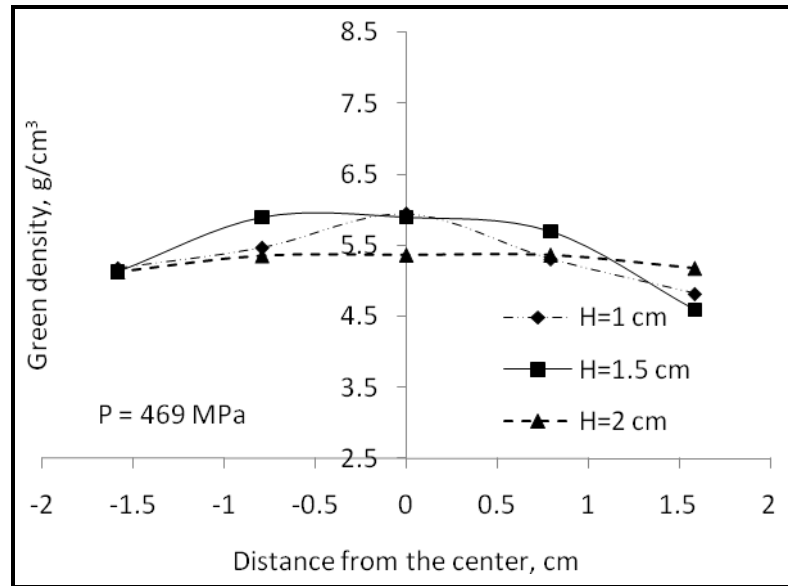
Figure A - 11: Density distribution of second layer at 469 MPa for all samples
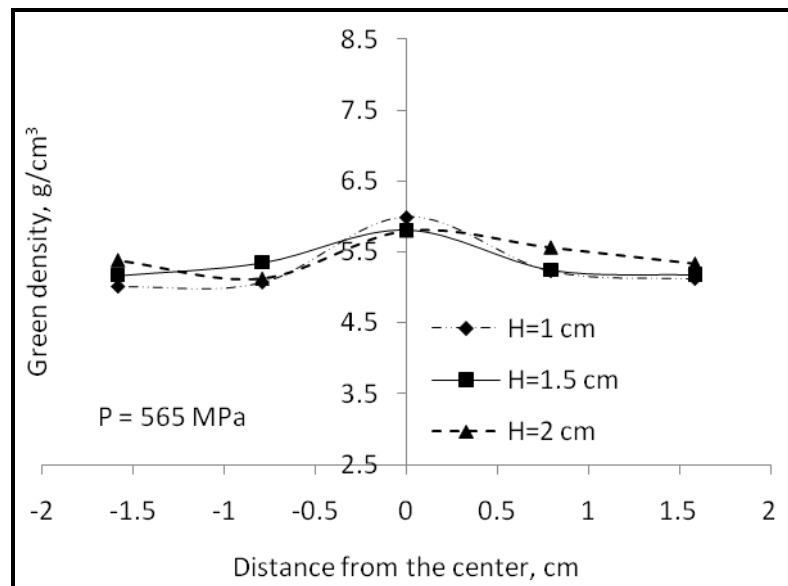

Figure A - 12: Density distribution of second layer at 565 MPa for all samples
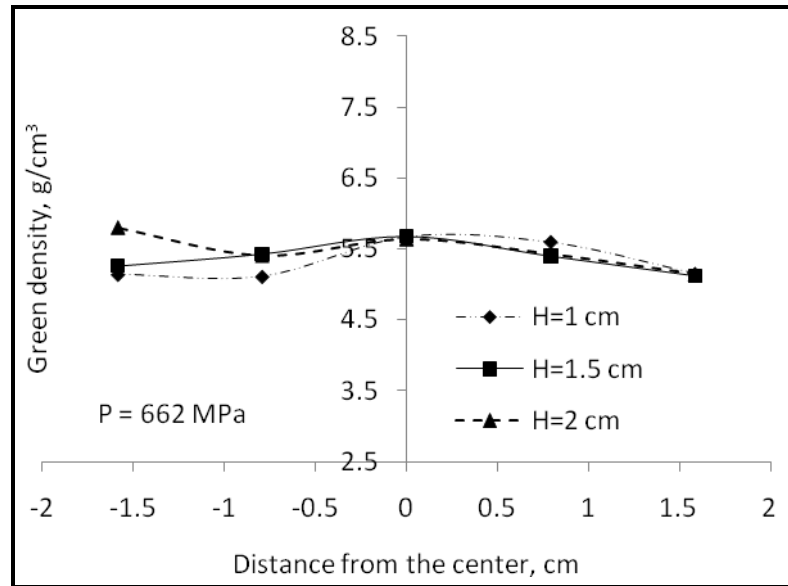
Figure A - 13: Density distribution of second layer at 662 MPa for all samples
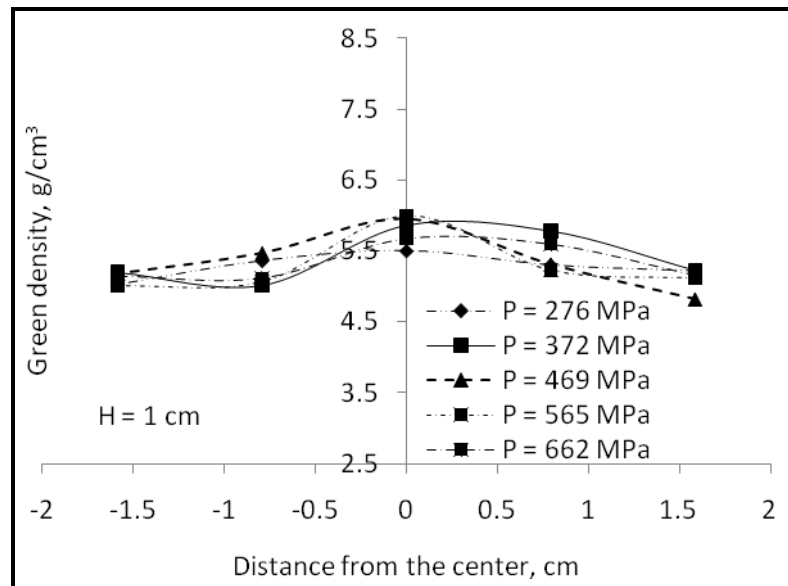

Figure A- 14: Density distribution of second layer for 1.0 cm thick sample
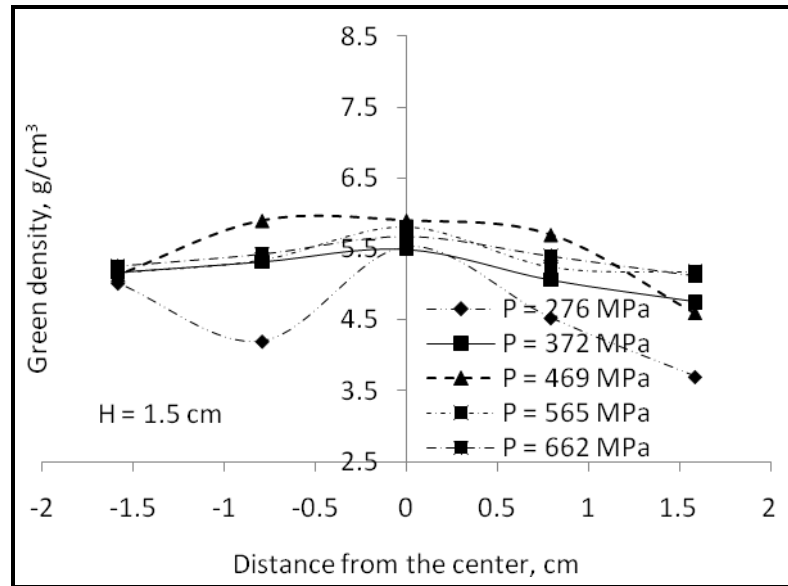
Figure A - 15: Density distribution of second layer for 1.5 cm thick sample
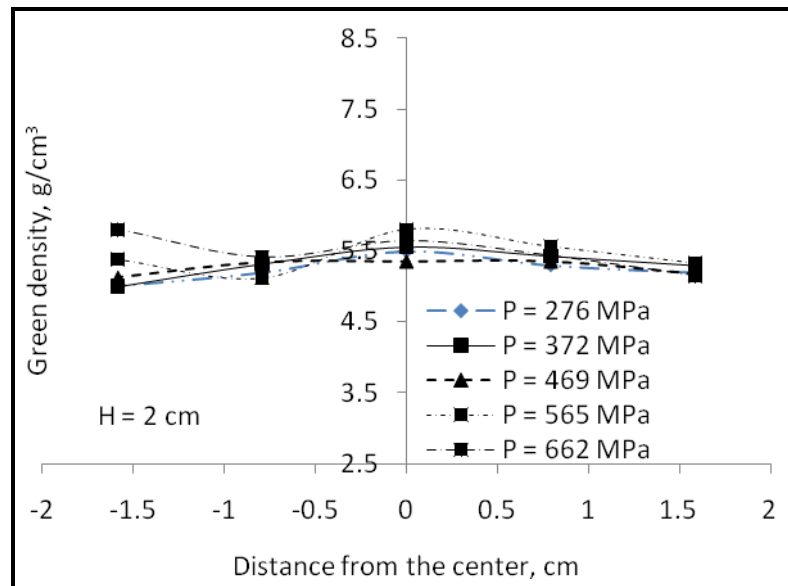
Figure A - 16: Density distribution of second layer for 2.0 cm thick sample
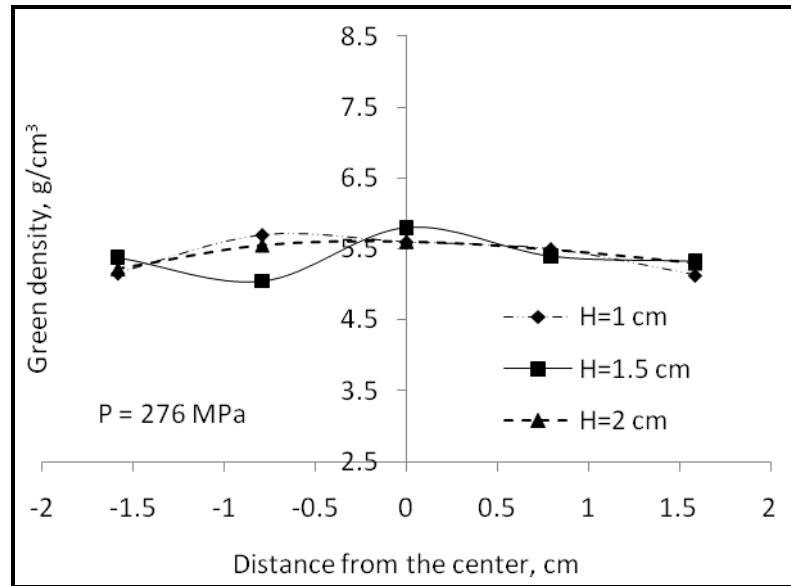
Figure A - 17: Density distribution of mid surface layer at 276 MPa for all samples
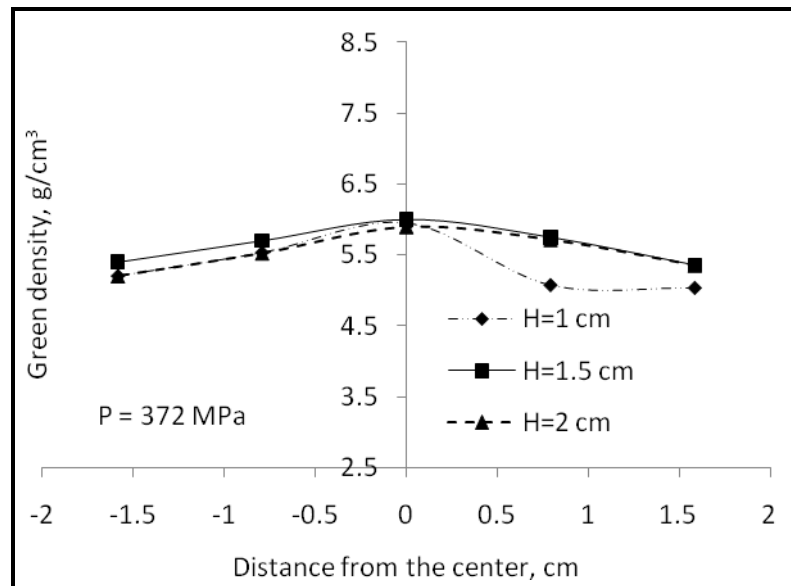
Figure A - 18: Density distribution of mid surface layer at 372 MPa for all samples
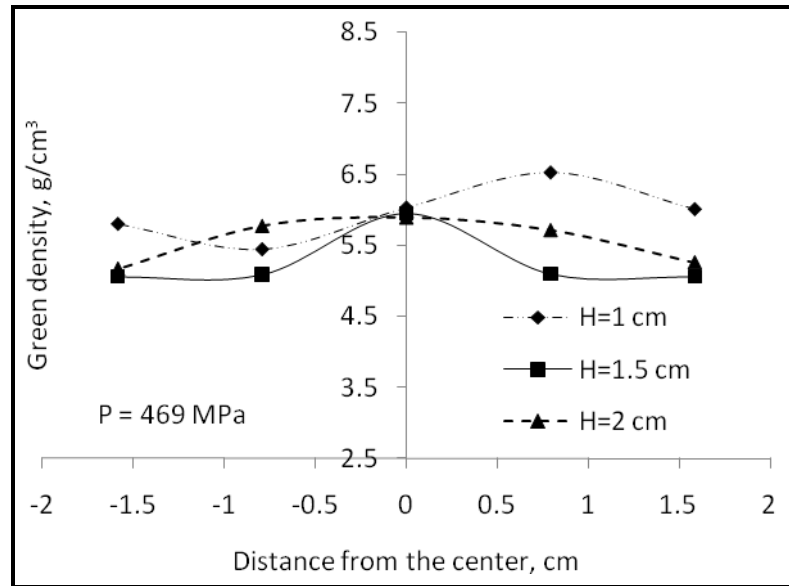
Figure A - 19: Density distribution of mid surface layer at 469 MPa for all samples
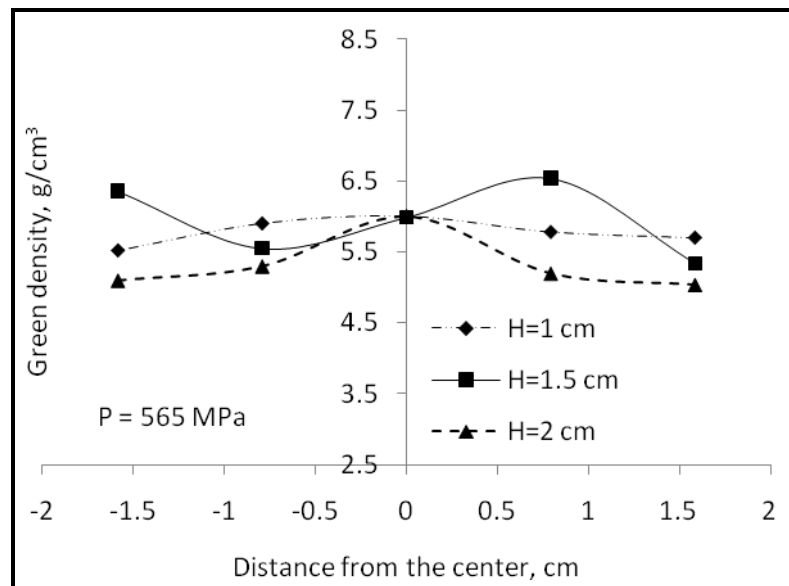
Figure A - 20: Density distribution of mid surface layer at 565 MPa for all samples
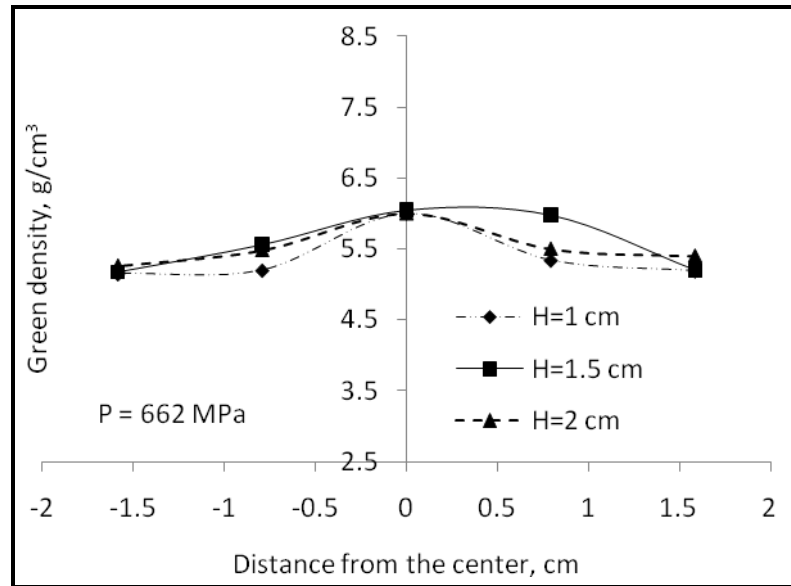
Figure A - 21: Density distribution of mid surface layer at 662 MPa for all samples
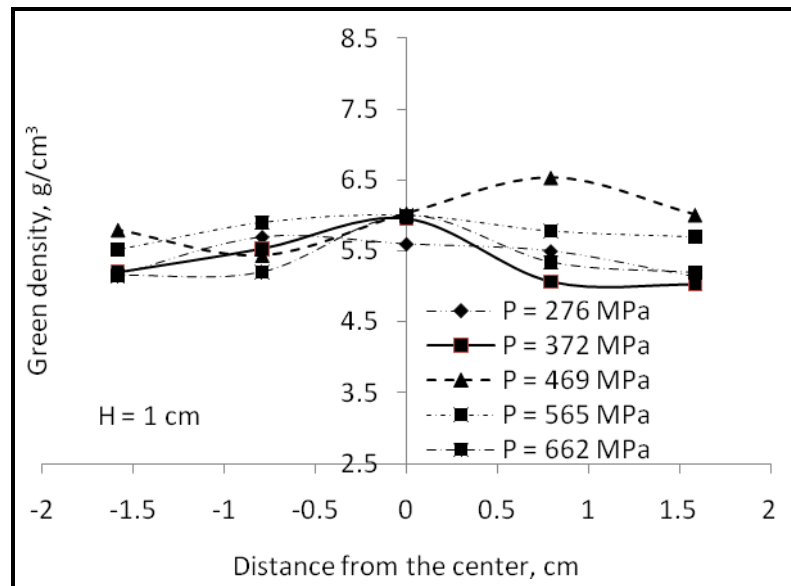

Figure A - 22: Density distribution of mid surface layer for 1.0 cm thick sample
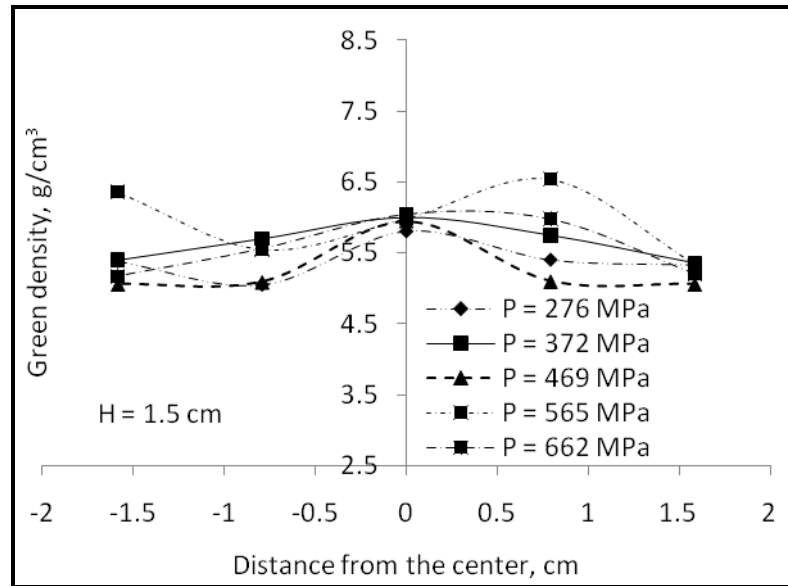
Figure A - 23: Density distribution of mid surface layer for 1.5 cm thick sample
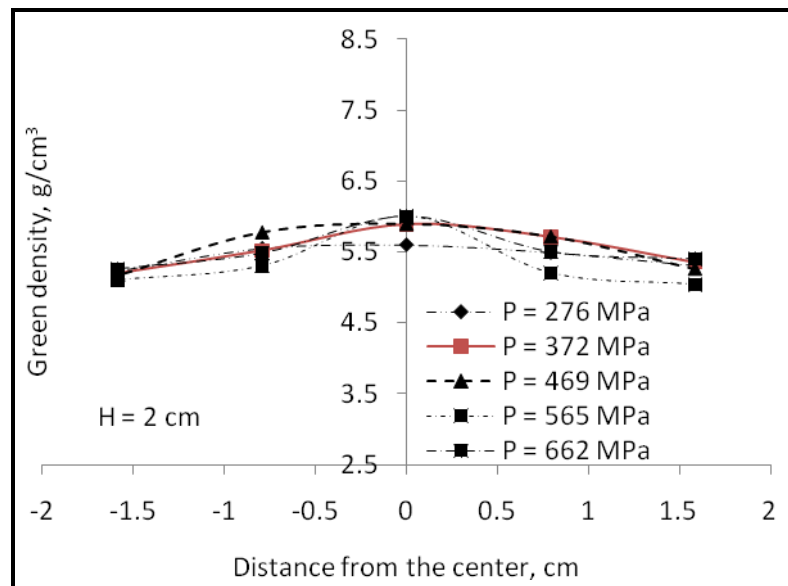
Figure A - 24: Density distribution of mid surface layer for 2.0 cm thick sample
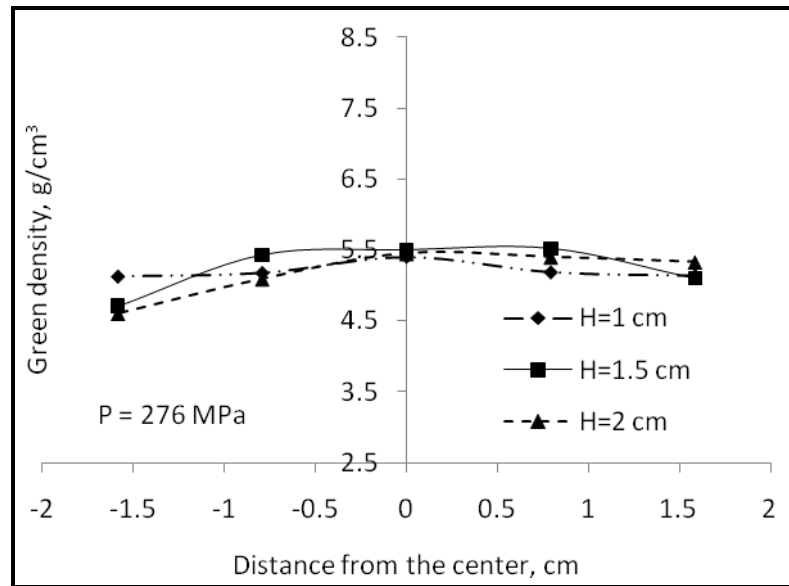
Figure A - 25: Density distribution of forth layer at 276 MPa for all samples
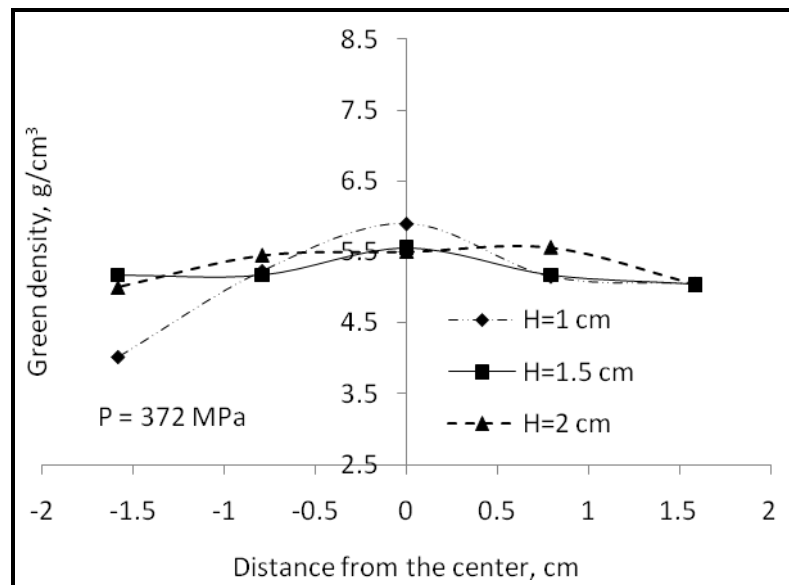
Figure A - 26: Density distribution of forth layer at 372 MPa for all samples
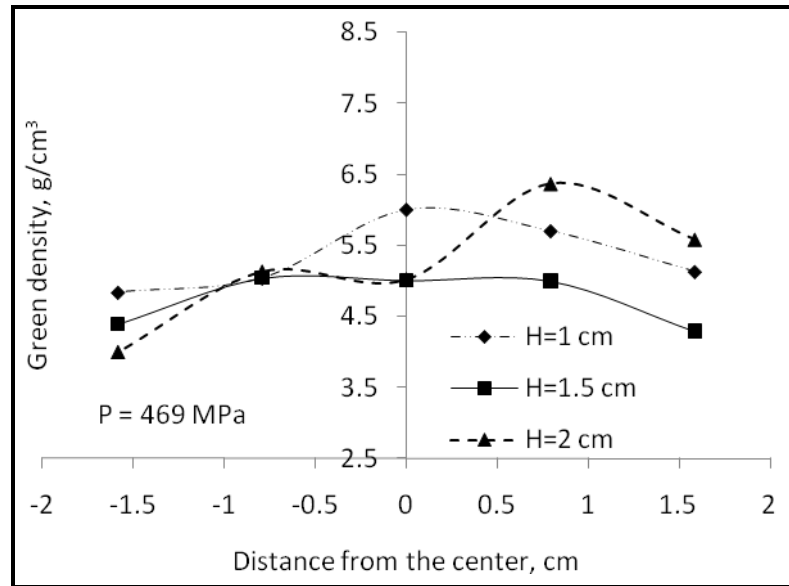
Figure A - 27: Density distribution of forth layer at 469 MPa for all samples
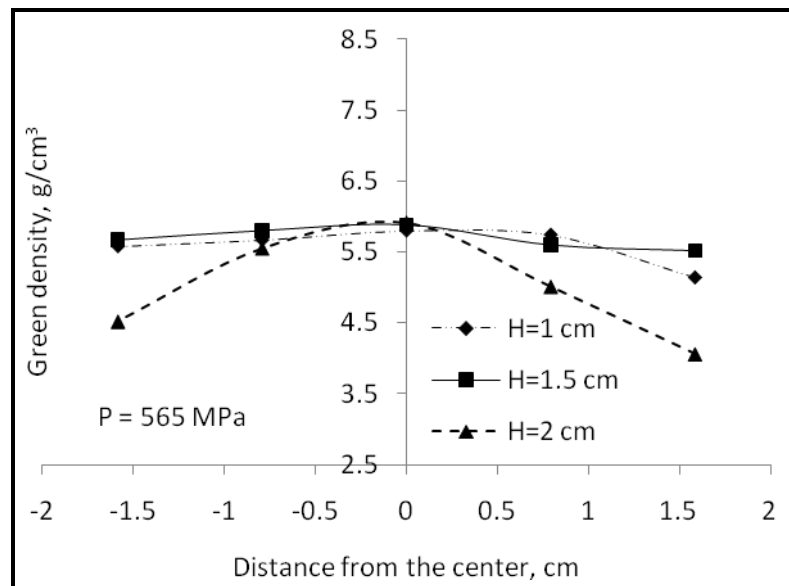
Figure A - 28: Density distribution of forth layer at 565 MPa for all samples
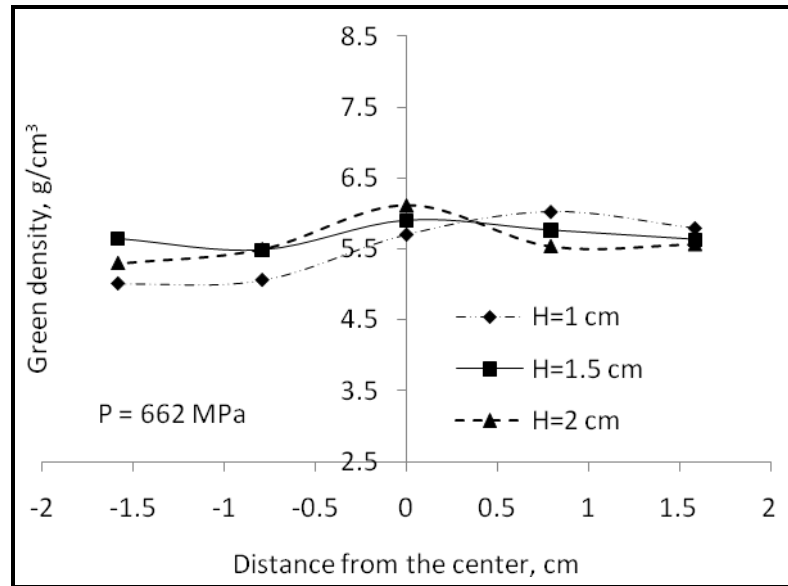
Figure A - 29: Density distribution of forth layer at 662 MPa for all samples
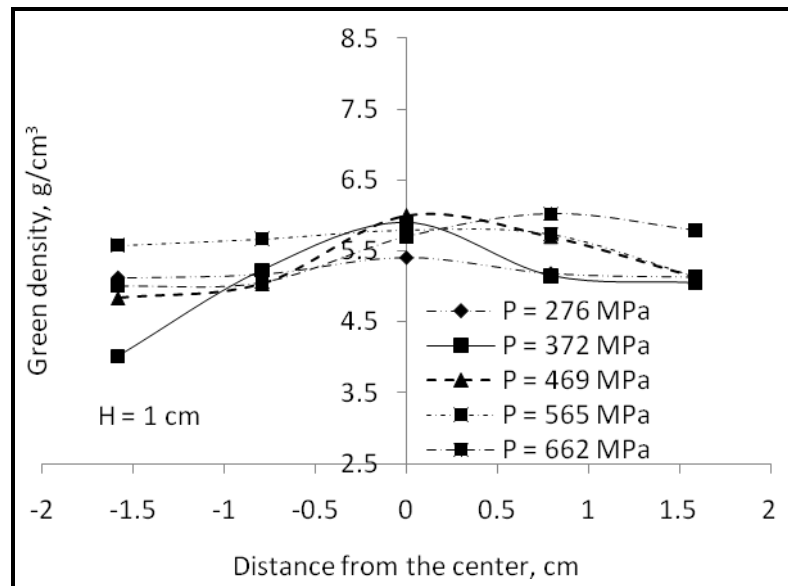
Figure A - 30: Density distribution of forth layer for 1.0 cm thick sample
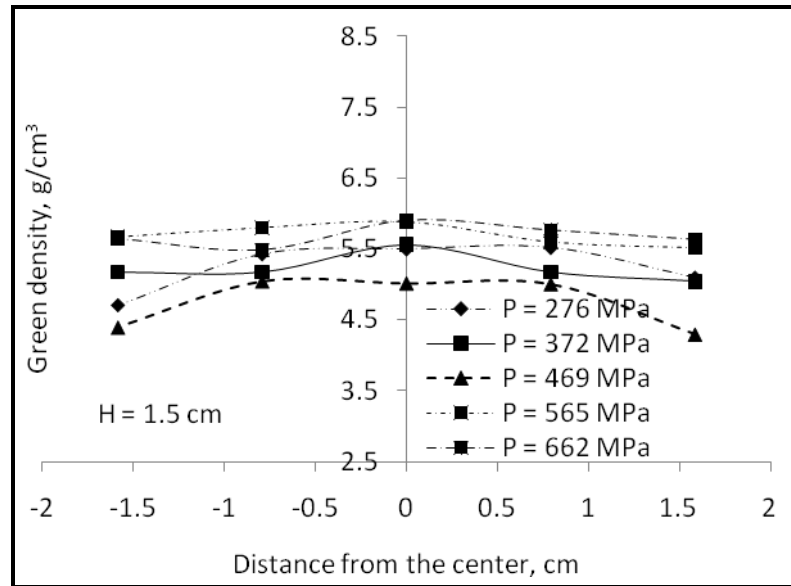
Figure A - 31: Density distribution of forth layer for 1.5 cm thick sample
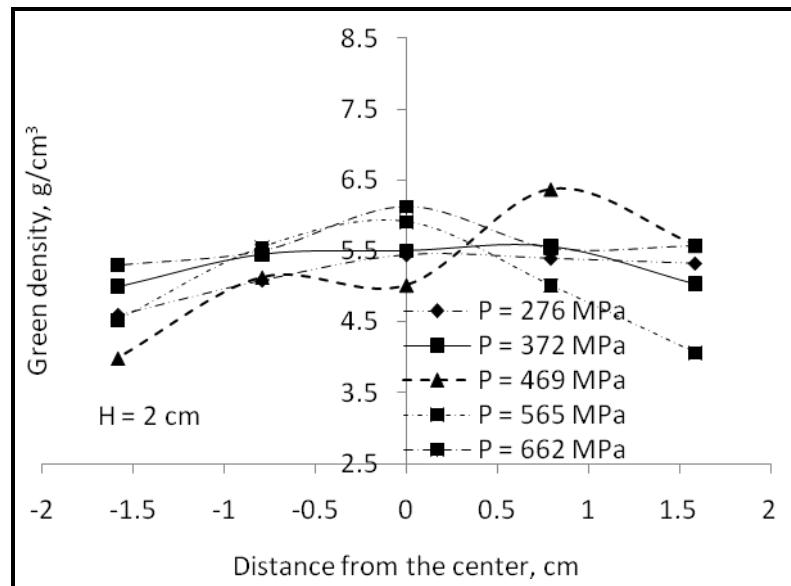
Figure A - 32: Density distribution of forth layer for 2.0 cm thick sample

References

[1]   C.-Y. Wu, L. Dihoru and A. C. F. Cocks, "The flow of powder into simple and stepped dies", Powder Technology, Vol. 134, pp. 24–39, 2003.

[2]   C.-Y. Wu, A. C. F. cocks and O. T. Gillia, "Die filling and powder transfer", Advances in powder metallurgy and particulate materials, Vol. 4, pp. 258–272, Princeton, NJ, MPIF, 2002.

[3]   C.-Y. Wu, A. C. F. Cocks, O. T. Gillia and D. A. Thompson, "Experimental and numerical investigations of powder transfer", Powder Technology, Vol. 138, pp.216–228, 2003.

[4]   A. Benner and P. Beiss, "Machinability of green powder metallurgy components ",Powder Metallurgy, Vol. 44, pp.299–303, 2001.

[5]   T. Mamedov and V. A. Mamedov, "New technological approach to fabrication of high density PM parts by cold pressing sintering", Powder Metallurgy, Vol. 47, No. 3, 2004.

[6]   D. Korachkin, D. T. Gethin, R. W. Lewis and J. H. Tweed, "Friction measurement and lubrication in unloading and ejection stages in powder pressing cycle", Powder Metall., Vol. 51, No.1, pp.14-30, 2008.

[7]   B.J. Briscoe and S.L. Rough, "The effects of wall friction in powder compaction", Physicochemical and Engineering Aspects, No. 137, pp. 103-116, 1998.

[8]   R.M. Nedderman, "The flow of granular materials-II: velocity distribution in silo flow", Trans. Inst. Chem. Eng, Vol.60, pp. 259, 1982.

[9]   H. Khorsand , M. Arjomandi , H. Abdoos and S.H. Sadati, "Application of Artificial Neural Network for Prediction of Heat Treated Sintered Steels Properties", Defect and Diffusion Forum, Vol. 276, pp. 323-328, 2008.

[10] K. V. Sudhakar and Mohammed E. Haque, "Mechanical Behaviour of Powder Metallurgy Steel—Experimental Investigation and Artificial Neural Network-Based Prediction Model", Journal of Materials Engineering and Performance, Vol. 10, No.1, February 2001.

[11] D. Korachkin, D. T. Gethin, R. W. Lewis, J. H. Tweed and D. M. M. Guyoncourt, "Measurement of Young's modulus and tensile failure properties of green powder compacts", Powder Metallurgy, Vol. 51, NO. 2, 2008.

[12] P. M. Modnet, "Measurement of friction for powder compaction modelling", Powder Metallurgy, Vol.2, No.4, pp. 301–311, 2000.

[13]   I.C. Sinka, J.C. Cunnigham and A. Zavaliangos, "Analysis of tablet compaction. 1. Characterization of mechanical behaviour of powder and powder and tooling friction", Powder Technology, Vol. 133, pp. 33-43, 2003.

[14]   A. Michrafy, J. A. Dodds and M. S. Kadiri, "Wall friction in the compaction of pharmaceutical powders: Measurement and effect on the density distribution", Powder Technology, Vol. 148, pp.53–55, 2004.

[15]   P. Doremus, F. Toussaint and E. Pavier, "Investigation of iron powder friction on tungsten carbide tool wall", Powder Metallurgy, Vol. 44, No.3, pp.243–247, 2001.

[16]   L. Sanchez, E. Ouedraogo, C. Dellis and L. Federzoni, "Influence of container on numerical simulation of hot isostatic pressing: final shape profile Comparison", Powder Metallurgy, Vol. 47, No. 3, pp. 253-262, 2004.

[17]   C. C. Degnan, A. R. Kennedy and P. H. Shipway, "Relationship between physical structure and machinability of green compacts", Powder Metallurgy, Vol. 50, No. 1, 2007.

[18]   S.H Luk, A.B. Davala and F.Y.Chan, "Processing experience of green strength enhanced materials system advances in powder metallurgy and particulate materials", Metal powder industries federation, Vol.3, part 16, pp.33-53, 1997.

[19]   E. Ernst, F. Thummler, P. Beiss, R. Wahling and V. Arnold, "Friction Measurements during powder compaction", powder metallurgy, Vol.23, No.2, pp.77-84, 1991.

[20]   B.N.J. Persson, " Sliding Friction: Physical, principles and application" second Edition, Springer, 2000.

[21]   V. Bonnefoy, P. Doremus, and G. Puente, "Investigation on friction behaviour of treated and coated tools with poorly lubraicated powder mixed", Powder metallurgy, Vol. 46, pp. 224-229, 2003.

[22]   N. Solimanjad, "Friction in metal powder processing". Thesis, Lulea University of Technology. 2001.

[23]   N. Solimanjad, "New method of measuring and characterisation of friction at wide range of density in metal powder compaction". Powder metallurgy, Vol. 46, pp. 48-55, 2003.

[24]   L.N. Smith, R.M. German, R. Cherian, P.S. Midha and T. Pelletiers, "A neural network for selection of powders and process settings for Cu powder metallurgy materials" Proceedings of the International Conference on Powder Metallurgy and Particulate Materials, Vancouver, Canada, 1999.

[25]   HIPIH. Ho¨gana¨s, "Iron Powder Information Hub, Database and Information Package from Ho¨gana¨s AB Sweden, 1999.

[26]   MPR, the MPR Structural Materials Selector, European Powder Metallurgy Association, Shrewsbury, UK, 1989.

[27]   L.N. Smith and P.S. Midha, "Simulation of metal powder compaction, for development of a knowledge-based powder metallurgy process advisor", Journal of Material Processing and Technology, Vol. 79, pp.94–100, 1998.

[28]   S. Ozan, M. Taskin, S. Kolukisa and M.S. Ozerdem "Application of ANN in the prediction of the pore concentration of aluminum metal foams manufactured by powder metallurgy methods" International Journal of Advanced Manufacturing, Vol. 39, pp. 251-256, 2008.

[29]   N. Altinkok and R. Koker, "Modeling of the prediction of tensile and density properties in particle reinforced metal matrix composites by using neural network", Materials and Design, Vol. 27, pp. 6245-631, 2006.

[30]   B. Wikman, G. Bergman, M. Oldenburg and H. Å. Häggblad, "Estimation of constitutive parameters for powder pressing by inverse modelling", Structure Multidisc Optimum, Vol.31, pp. 400–409, 2006.

[31]   R.P. Cherian, L.N. Smith and P.S. Midha, "A neural network approach for selection of powder metallurgy materials and process parameters", Artificial Intelligence in Engineering, Vol. 14, pp. 39–44, 2000.

[32]   Fırat Kafkas , Cetin Karatas , Adnan Sozen , Erol Arcakliog˘lub and Su¨leyman Saritas, "Determination of residual stresses based on heat treatment conditions and densities on a hybrid (FLN2-4405) powder metallurgy steel using artificial neural network", Materials and Design, Vol. 28, pp. 2431–2442, 2007.

[33]   L.N. Smith, R.M. German and M.L. Smith, "A neural network approach for solution of the inverse problem for selection of powder metallurgy materials", Journal of Materials Processing Technology, Vol.120, pp.419–425, 2002.

[34]   L.H. Han, J.A. Elliot, A.C. Bentham, A. Mills, G.E. Amidon and B.C. Hancock, " A modified Drucker-Prager cap model for die compaction simulation of pharmaceutical powders, Solid and Structure", Vol. 45, pp. 3088-3106, 2008.

[35]   Cunningham, J.C., Sinka, I.C., Zavaliangos, A., "Analysis of tablet compaction characterization of mechanical behavior of powder and powder/tooling friction". Journal of Pharmaceutical Sciences, Vol. 93, pp. 2022–2039, 2004.

[36]   L. Ma, t. Zahara and R. Fields, "Numerical three dimensional simulation of cold compaction and spring back for prealloyed powder composites", Powder Metallurgy, Vol. 47, pp. 31-37, 2004.

[37]   B. Storakers, N.A. Fleck and R.M. McMeeking. "The viscoplastic compaction of composite powders", Journal of Mechanics and Physics of Solids, Vol. 47 pp. 785-815, 1999.

[38]   P. Redanz, " Numerical modeling of the powder compaction of a cup" European Journal of Mechanics Nonlinear Solids, Vol. 18, pp. 399-413, 1999.

[39]   A. Kuhn and C.L. Downey. "Deformation characteristics and plasticity theory of sintered powder materials", International Journal of powder Metallurgy, Vol. 7, pp. 15-25, 1971.

[40]   C.M. Huang, P.Q. Chen, M. Shao and Y. Y. Li, "Numerical simulation powder compaction of metallurgy component", Transaction of Nonferrous Metals Society of China, Vol. 16, pp. 1353-1357, 2006.

[41]   N.A. Fleck, L.T. Khun and R.M. McMeeking, "Yielding of metal powder bounded by isolated contacts", Journal of Mechanics, physics and solids, Vol. 40, pp.1139-1162, 1992.

[42]   Y.S. Kwon, H.T. Lee and K.T. Kim, "Analysis for Cold Die Compaction of Stainless Steel Powder", Transaction of ASME, Vol. 119, pp.366-373, 1997.

[43]   S. Shima and M.Oyane, "Plasticity Theory for porous metals" International Journal of Mechanical Science, Vol. 018, pp.285-291, 1976.

[44]   O. Coube, A. C. F. Cocks and C.-Y. Wu, "Experimental and numerical study of die filling, powder transfer and die compaction", Powder Metallurgy, Vol. 48, No. 1, 2005.

[45]   D. C. Drucker and W. Prager, "Soil mechanics and plastic analysis or limit design", Appl. Math, Vol. 10, pp.157–175, 1952.

[46]   I.S. Sandler, F. L. Dimaggio and G.Y. Baladi, "Elastoplastic stress strain theory for cohesionless soil" Journal of Geo-technology Engineering Division, transaction of ASCE, Vol. 102, pp. 683-699, 1976.

[47]   S.-J. Park, H. N. Han, K. H. Oh, K. W. Kang and K. W. Song, "Finite element simulation of duplex compaction processes", Powder Metallurgy, Vol. 48, No. 193, 2005.

[48]   R. Zhang, R. S. Engel, N. J. Salamon, and R. M. German, "Finite element analysis on the sintering of stainless steel 316L powder compacts", Advances in powder metallurgy and particulate materials, pp.60-68, Princeton, NJ, 2002.

[49]   www.tiniusolsen.com accessed at February 2010.

[50]   www.speciation.net accessed at February 2010.

[51]   G.J. Udo, "Neural network applications in manufacturing processes", Computer Industry Eng, Vol. 23, pp. 97–100, 1992.

[52] H. Zhand and S.H. Huang, "Applications of neural networks in manufacturing", International Journal Production Research, Vol. 33, pp. 705–728, 1995.

[53] M. Smith, "Neural Networks for Statistical Modelling", Van Nostrand Reinhold, New York, ISBN 0-442-01310-8, 1993.

[54] www.mathworks.com/access/helpdesk/help/toolbox/nnet/ accessed at March 2010.

[55] S. Haykin, "Neural networks, a comprehensive foundation", McMillian College, New York, pp. 198–203, 1994.

[56] V. Tandon and H. El-Mounayri, "A novel artificial neural networks force model for end milling", IJAMT, Vol. 18, pp.693–700, 2001.

[57] J. Cedergren, N.J. Sorensen and A.P. Bergmark, "Three dimensional analysis of compaction of metal powder" Mechanics of Materials, Vol. 34, pp.43-59 and 27-40, 2002

[58] "MSC MARC Theory Manual", Volume C, 2008 Revision

[59] E. Pavier and P. Doremus, "Triaxial Characterisation of Iron Powder Behaviour", Powder Metallurgy, Vol. 42, No. 4, pp.345-352, 1999.

[60] E. Pavier and P. Doremus Pavier, "Comparison between Constitutive Equations. Modeling the Compaction of Iron Powder and Experimental Data obtained with Triaxial Tests" International Workshop on Modeling of Metal Powder Forming Processes, pp.1-8, 1997.

[61] E. Pavier and P. Doremus Pavier, "Mechanical Behaviour of a Lubricated Iron Powder", Advances in Powder Metallurgy and Particulate Materials, Vol.2 (PART 6), pp.27-40, 1996